Maker-Fringe Analysis and Electric-Field Poling of Lithium Niobate

J. Andrew Aust
B.S., University of Vermont, 1987
M.S., University of Colorado, 1990

A thesis submitted to the
Faculty of the Graduate School of the
University of Colorado in partial fulfillment
of the requirement for the degree of
Doctor of Philosophy
Department of Electrical and Computer Engineering
1999

This thesis entitled:
Maker-Fringe Analysis and Electric-Field Poling of Lithium Niobate
Written by J. Andrew Aust
Has been approved for the Department of Electrical and Computer Engineering

_____
Norman A. Sanford

_____
Alan R. Mickelson

_____
Date

The final copy of this thesis has been examined by the signatories, and we find that both the content and the form meet the acceptable presentation standards of scholarly work in the above discipline.

Abstract

Aust, J. Andrew (Ph.D., Electrical Engineering)

Maker-Fringe Analysis and Electric-Field Poling of Lithium Niobate

Thesis directed by Professor Adjunct Norman A. Sanford

This dissertation focuses on Maker-fringe analysis and electric-field poling of *z*-cut lithium niobate ($LiNbO_3$). The Maker-fringe analysis involved examining second-harmonic generation (SHG) as a function of pump beam angle of incidence, where four separate pump-SHG polarization orientations were examined. The theoretical model developed here to describe the Maker fringes includes the full birefringent of this uniaxial material. The theory also considers Fabry-Perot resonances of both the pump and second-harmonic waves in the sample. Simultaneously fitting all four pump-SHG orientations to sample thickness, ordinary index of refraction at the pump and second-harmonic wavelengths, and extraordinary index of refraction at the pump and second-harmonic wavelengths has led to the most comprehensive Maker-fringe analysis attempted to date. From this analysis, index of refraction variations lead to a description of the compositional variation within a wafer and between wafers. Other properties that may also be determined are the nonlinear coefficients $d_{ij}^{(2)}$, electrooptic coefficients r_{ij}, surface charges, internal fields, stresses, and strains. Any effect that perturbs the indices of refraction by 1×10^{-5} or more can be examined.

The Maker-fringe analysis revealed that the extraordinary index of refraction of $LiNbO_3$ is smaller than that predicted by the commonly used Sellmeier equation derived by Edwards and Lawrence [Edwards '84]. The discrepancy is on the order of -9×10^{-4} at a wavelength of 532 nm and appears to be related to the compositional variation between the congruent material used in the original index studies and that, which is currently available. Maker-fringe analysis has also been used to measure the nonlinear coefficients $d_{31}^{(2)} = 5.95$ pm/V and $d_{33}^{(2)} = 25.2$ pm/V, electrooptic coefficients $r_{13}^{T} = 1.27 \times 10^{-5}$ mm/kV and $r_{33}^{T} = 3.44 \times 10^{-5}$ mm/kV at a wavelength of 1.064 μm, and $r_{13}^{T} = 1.39 \times 10^{-5}$ mm/kV and $r_{33}^{T} = 3.43 \times 10^{-5}$ mm/kV at a wavelength of 532 nm, and pyroelectrically induced electric fields up to -19.1 kV/mm after a 200 °C temperature cycle.

The electric-field poling experiments involved examination of the poling current with respect to the applied poling field and Maker-fringe analysis of domain-reversed material. I observed a similar offset in the behavior of the poling current (6.9 kV/mm) as other researchers have seen in polarization hysteresis loops (6.7 to 7.0 kV/mm). I also correlated this offset with the observation of fringe shifts in the Maker-fringe scans of domain reversed material.

For Dad

The hardest working man I know

Acknowledgements

I am indebted to Norm Sanford, my mentor and teacher. Without your support this dissertation would never have reached completion. You have shown incredible patience throughout this ordeal, allowing me to take a winding scenic route on occasion but nudging me back to the highway when necessary. Your unwavering passion over photonics research is inspiring.

I'd like to thank NIST in general for providing the top-notch facilities where all of this research was performed and for funding much of the tuition.

I'd also like to thank Alexana Roshko for her help with material science issues involved with $LiNBO_3$, Sara Metz for scanning photographs and being the best office automation assistant our group has ever had, and the Lab Gang for many fruitful discussions over burritos at Z-Teca, mostly about the Avalanche and Broncos.

To Mom and Dad, I want to thank you for providing everything necessary for a developing scientist to flourish, not to mention displaying the wisdom not to always ask, "how's the Ph.D. going." I am who I am today because of the two of you.

And finally I'd like to thank my family, Sue, Tucker, and Bailey, for providing a safe haven where I could forget about the rigors of my Ph.D. and just be a husband and dad. Sue, you kept everything together during this very trying period, I can not begin to express how much I appreciated that. I love you with all my heart. To the boys, thank you for every smile, laugh, and hug, they truly warm the heart. I apologize for not always being there for you when you wanted me and I promise tonight "dada no go to work."

Contents

List of Tables

List of Figures

Chapter 1

Introduction

1.0 Dissertation Overview

In this work, I use Maker-fringe analysis to examine several properties of lithium niobate ($LiNbO_3$). Historically, Maker-fringe analysis has been used for the measurement of nonlinear coefficients; in most cases this has involved fitting the envelope function of the fringes only. In my analysis, this one measurement technique is used to examine the indices of refraction and the electrooptic coefficients of $LiNbO_3$ as well as the effects to the material due to pyroelectricity and domain reversal [Aust ‘97a, ‘97b].

My theoretical contribution is the full Fabry-Perot resonance development of the second-harmonic generation (SHG) for uniaxial media. I also introduce a heuristic correction factor to compensate for the lack of infinite plane waves. My treatment includes all four possible pump-to-SHG polarization orientations obtained from rotation of a *z*-cut wafer about its *y*-axis.

Finally, I examine the poling current, which is involved with domain reversal, as a function of electric field. A correlation between the Maker-fringe analysis of domain reversed $LiNbO_3$ and the poling current studies is made.

1.1 Background

Lithium niobate is used for a host of accoustooptic, electrooptic, and nonlinear optical applications. As the sophistication of the devices employing $LiNbO_3$ increases the need for better characterization of this material has arisen. Wafer uniformity is a key issue for improving device performance and yields. One method of analysis, suggested as a tool to examine the uniformity of $LiNbO_3$ wafers and boules, is Maker-fringe analysis [Lunt '85]. Maker fringes, or the oscillations of the SHG as a function of pump angle of incidence, were first demonstrated by Maker *et. al* in 1962 while examining quartz and potassium dihydrogen phosphate (KDP) [Maker '62]. Maker fringes are produced by rotating a nonlinear material, typically around one of its crystallographic axes, while illuminating it by a polarized pump beam. The fringes are the result of interference between the bound and free harmonic waves that propagate in a nonlinear material as a result of the pump wave. The attributes of the fringes, their frequency and amplitude, depend upon several criteria including the indices of refraction at the fundamental and second-harmonic wavelengths, nonlinear coefficients, sample thickness, pump and SHG polarizations, and location of rotation axis with respect to crystal axes.

Bloembergen reported a theoretical description of nonlinear frequency generation by a nonlinear material in 1962 [Bloembergen '62]. His treatment considered the sum frequency produced from a plane-parallel plate of

isotropic material being pumped by two infinite plane waves at frequencies ω_1 and ω_2. The resulting expression for the electric field at $\omega_3 = \omega_1 + \omega_2$ was obtained by considering Fresnel's laws for all three frequencies involved.

In 1969 Jerphagnon stated that Bloembergen's "formulas, besides the fact that they hardly can be used by the experimentalist, do not describe the multiple refection phenomenon as it usually occurs" [Jerphagnon '69]. Jerphagnon then modified the multiple reflection result in such a way as to eliminate the coherent addition of the E_m and E_{m+1} transmitted electric fields, where $m \geq 1$. The reasoning given for his modification was that the crystal faces were not flat and parallel enough to get a constant phase difference between E_m and E_{m+1}. His result includes the incoherent addition of the multiple pass fields but ignores the coherent addition. Another reason this assumption worked for Jerphagnon is that the indices of refraction of the materials he was examining, quartz, ADP, and KDP, are relatively low, ~1.5. This reduces the reflectance of each pass and, therefore, reduces the interference. Jerphagnon's assumption may have been accurate for his studies, but it is far from accurate for the work presented here, where the nominal index of refraction of $LiNbO_3$ is ~2.2 and the wafers are polished to a scratch/dig of 10/5 and have a wavefront distortion at 633 nm of $<\lambda/4$.

My recent interest in $LiNbO_3$ involves its use as a nonlinear material, in particular, its use in implementing quasi-phase-matched (QPM) nonlinear optical interactions [Yamada '93]. QPM is an extremely versatile method of achieving phase matching for optical frequency conversions.

Conventional birefringent phase-matching relies on the chance material characteristics that the index of refraction at the fundamental frequency is the same as it is for the harmonic frequency. This criterion is very limiting, inasmuch as there are only a finite number of frequency conversions that can be birefringently phase-matched with currently known materials. As examples, $LiNbO_3$ birefringently phase-matches SHG at room temperature for fundamental wavelengths of ~1.08 and ~3.74 μm, while another material suitable for QPM, $LiTaO_3$, is not birefringently phase matchable.

QPM uses a periodic modification of the nonlinear susceptibility to compensate for the phase walkoff between the fundamental and harmonic waves. In the simplest case this modification is a periodic sign reversal of the nonlinear susceptibility. The period of this modulation is two times the coherence length l_c of the particular interaction. For SHG the phase mismatch between the fundamental and harmonic waves reaches a value of π at a distance of l_c in the media, at which point the sign of the nonlinear coefficient is reversed and the fundamental field continues to feed power into the harmonic field. Instead of relying upon the birefringence and/or the dn/dT for the nonlinear media, phase-matching is achieved by tailoring the period of the QPM grating to the particular desired interaction. This allows for efficient phase-matching of any frequency conversion within the transparency window of the material. $LiNbO_3$ is particularly suited for implementing QPM because it is a ferroelectric material. From Lines and Glass [Lines '77]:

> A material is defined as ferroelectric when it has two or more orientational states in the absence of an electric field and can be

> shifted from one to the another of these states by an electric field. Any two of the orientation states are identical in crystal structure and differ only in electric polarization vector at null electric field.

Using the ferroelectric property of $LiNbO_3$, the direction of the spontaneous polarization, and therefore the sign of the nonlinear coefficients, can be reversed by the application of a sufficiently strong poling field. A spontaneous polarization domain grating can be formed in the material for implementing QPM by patterning the poling electrodes into a grating structure with individual segments the size of the coherence length of the desired interaction.

Domain reversal, the process of changing the direction of the spontaneous polarization, can briefly be explained as the movement of the Li^{+1} and Nb^{+5} ions with respect to the oxygen planes in the material. At temperatures below the Curie temperature, $LiNbO_3$'s structure consists of oxygen planes that are packed into octahedra. The interstices of these orctahedra are one-third filled by lithium, one-third filled with niobium, and one-third vacant. The order in which the cations occur in the $+z$ direction is Li Nb □ Li Nb □ Li Nb □, where □ denotes a vacancy [Weis '85]. During domain reversal, the Li^{+1} ions must pass through an oxygen plane from one oxygen octahedron to the next while the Nb^{+5} ions merely shift their position within an oxygen octahedron. Figure 1.1 schematically represents the positions of the Li^{+1} and Nb^{+5} ions before and after domain reversal. The motion of the cations in the crystal gives rise to a displacement current,

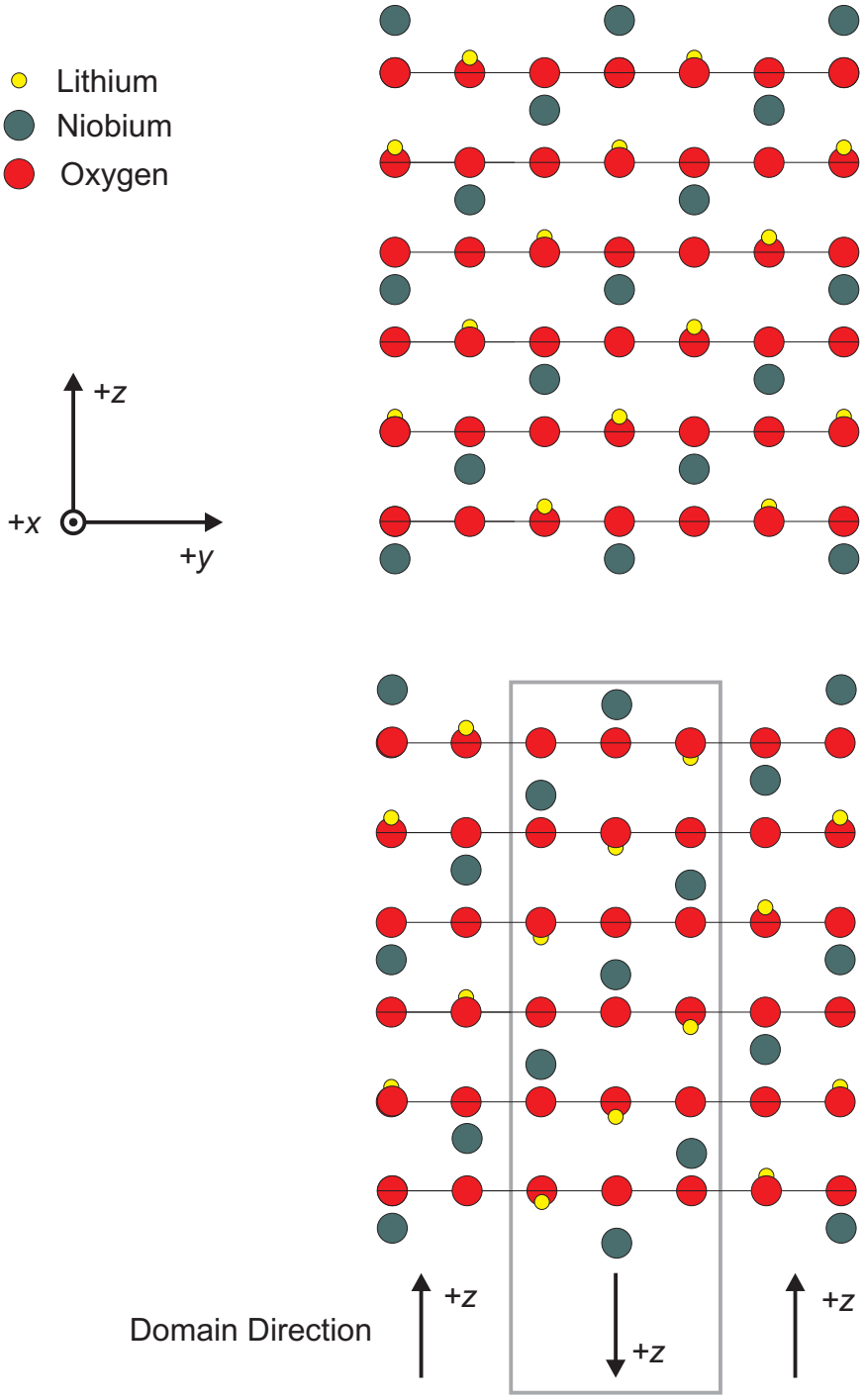

Figure 1.1 Position of ions in the $LiNbO_3$ structure. Top figure is for a single domain. Lower figure shows domain reversed region.

referred to here as a poling current, that can be measured and is a direct indication of the completeness of the domain reversal.

In the six years since the first demonstration of electrically induced periodically poled $LiNbO_3$ (PPLN), several groups around the world have attempted to perfect the poling process [Webjörn ’94, Goldberg ’95, Pruneri ’95, Meyn ’97, Rosenman ’98] while others have concentrated on trying to better understand the poling process itself [chao ’95, Gopalan ’97, ’98, Wang ’97, Miller ‘98]. Today PPLN substrates are commercially available from approximately two suppliers here in the United States and a number of other companies have in-house capabilities to produce such material. However, these substrates are still fairly expensive and available only in a limited number of domain periods. One of the reasons for this is the difficulty involved in producing the QPM gratings. Device yields are still too low due to the frequent occurrence of electrical breakdown suffered by the material during electric field poling at room temperature.

Chapter 2

Theoretical Development of Maker Fringe Analysis

2.0 Introduction

This treatment of Maker fringe analysis will deal with four specific pump-to-SHG relationships: extraordinary or *e*-polarized pump producing *e*-polarized SHG, *e*-polarized pump producing ordinary or *o*-polarized SHG, *o*-polarized pump producing *o*-polarized SHG, and *o*-polarized pump producing *e*-polarized SHG. Each of these nonlinear frequency conversions will be treated in two distinctly different developments. The first is a single-pass ray approach which will also include a second-pass correction. The second method is a fully resonant approach where the Fabry-Perot resonance of the pump and SHG will be considered. In presenting this formalism, the *e*-polarized pump producing *e*-polarized SHG case will be given in detail, because of its added complexity, while just the results will be stated for the remaining cases.

The substrate being considered here is *z*-cut $LiNbO_3$. For a *z*-cut wafer the *z*-axis of the crystal is normal to the wafer's polished surfaces. Figure 2.1 illustrates the orientation of the wafer in the experimental setup. For this exercise, the wafer rotation is about the *y*-axis while the pump propagation is in the *xz*-plane. The two different pump conditions are *e*- and *o*-polarized.

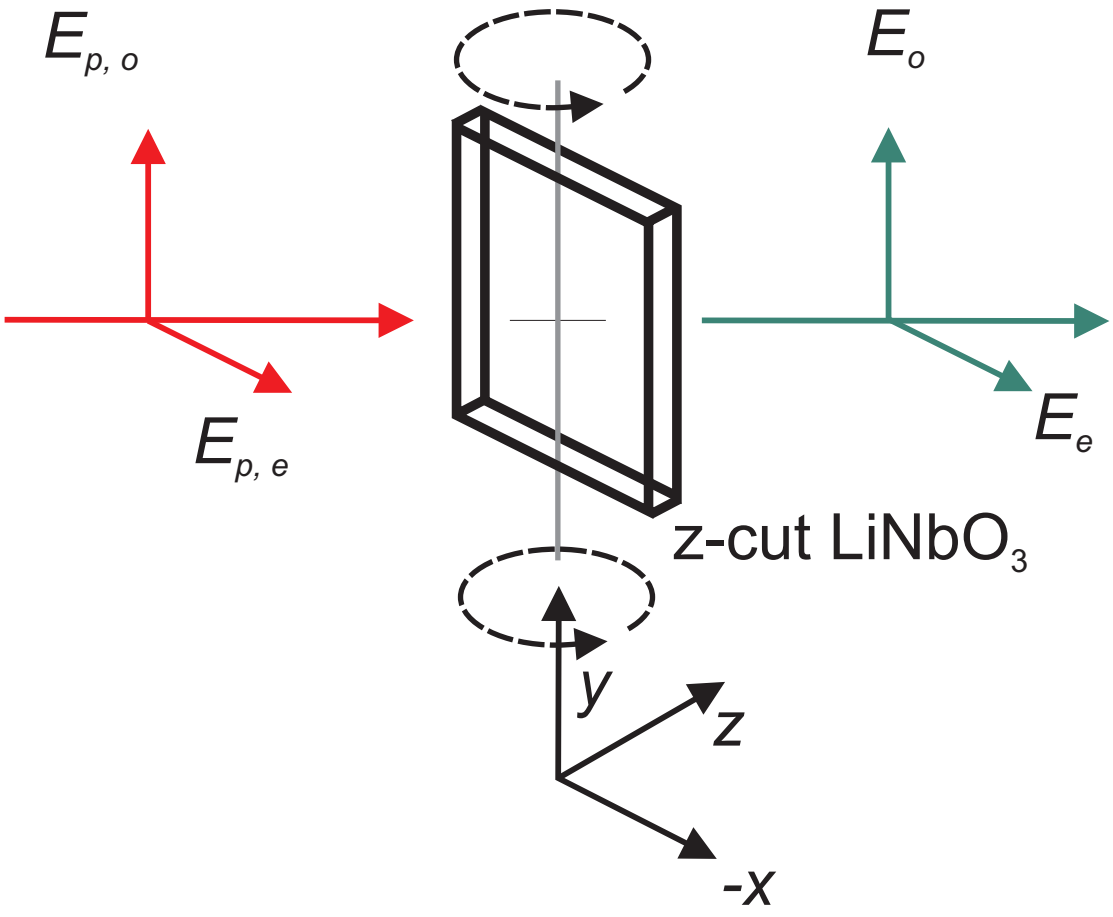

Figure 2.1 Schematic of sample orientation.

When the pump polarization is parallel to the plane of incidence it is referred to as *p*-, π-, or *e*-polarized. When the pump polarization is perpendicular to the plane of incidence it is referred to as *s*-, σ-, or *o*-polarized.

2.1 Wave Equations

The wave equations describing the propagation of light through a uniaxial crystal such as $LiNbO_3$ must first be developed. The result of this development will be used to express the propagation of the pump and the second-harmonic fields through the substrate. This is accomplished by starting with Maxwell's curl relations

$$\vec{\nabla} \times \vec{H} = \vec{J} + \frac{\partial \vec{D}}{\partial t} = \vec{J} + \varepsilon_o \vec{\vec{\varepsilon}} \frac{\partial \vec{E}}{\partial t} + \frac{\partial \vec{P}}{\partial t}, \tag{1a}$$

$$\vec{\nabla} \times \vec{E} = -\mu_o \frac{\partial \vec{H}}{\partial t}. \tag{1b}$$

The reference coordinate system is taken to coincide with the substrate's crystallographic axes. This results in the dielectric tensor $\vec{\vec{\varepsilon}}$ being diagonal with $\varepsilon_{11} = \varepsilon_{22} = n_o^2$ and $\varepsilon_{33} = n_e^2$, where n_o and n_e are the ordinary and extraordinary indices of refraction. For the sample-pump orientation chosen here all derivatives with respect to *y* are zero. Writing out the curl relations with the current $\vec{J}$ assumed to be zero gives

$$-\partial_z H_y = -i\omega\varepsilon_o n_o^2 E_x - i\omega P_x, \tag{2a}$$

$$-\partial_x H_z + \partial_z H_x = -i\omega\varepsilon_o n_o^2 E_y - i\omega P_y\,, \tag{2b}$$

$$\partial_x H_y = -i\omega\varepsilon_o n_e^2 E_z - i\omega P_z\,, \tag{2c}$$

$$-\partial_z E_y = i\omega\mu_o H_x\,, \tag{2d}$$

$$-\partial_x E_z + \partial_z E_x = i\omega\mu_o H_y\,, \tag{2e}$$

$$\partial_x E_y = i\omega\mu_o H_z\,. \tag{2f}$$

Solving Equations (2d-f) for H_x, H_y, and H_z, respectively, and then substituting appropriately into Equations (2a-c) gives

$$\partial_{xz}^2 E_z - \partial_z^2 E_x - \omega^2\varepsilon_o\mu_o n_o^2 E_x = \omega^2\mu_o P_x\,, \tag{3a}$$

$$-\partial_x^2 E_y - \partial_z^2 E_y - \omega^2\varepsilon_o\mu_o n_o^2 E_y = \omega^2\mu_o P_y\,, \tag{3b}$$

$$-\partial_x^2 E_z + \partial_{xz}^2 E_x - \omega^2\varepsilon_o\mu_o n_o^2 E_z = \omega^2\mu_o P_z\,. \tag{3c}$$

The mixed partial derivatives $\partial_{xz}^2 E_z$ and $\partial_{xz}^2 E_x$ must be eliminated. This is accomplished by using the fact that the media is charge-free, so that $\vec{\nabla}\bullet\vec{D} = 0$. Writing this equation out fully with $\vec{D} = \varepsilon_o\vec{\vec{\varepsilon}}\vec{E} + \vec{P}$ and again taking all derivatives with respect to y as zero gives

$$\vec{\nabla}\bullet\vec{D} = \varepsilon_o n_o^2\partial_x E_x + \partial_x P_x + \varepsilon_o n_e^2\partial_z E_z + \partial_z P_z = 0\,. \tag{4}$$

Rewriting Equation (4) to solve for $\partial_z E_z$ and again to solve for $\partial_x E_x$ gives

$$\partial_z E_z = \frac{-1}{\varepsilon_o n_e^2}\left(\varepsilon_o n_o^2\partial_x E_x + \partial_x P_x + \partial_z P_z\right), \tag{5a}$$

$$\partial_x E_x = \frac{-1}{\varepsilon_o n_o^2}\left(\varepsilon_o n_e^2\partial_z E_z + \partial_x P_x + \partial_z P_z\right). \tag{5b}$$

Taking ∂_x of Equation (5a) and ∂_z of Equation (5b) results in suitable expressions for eliminating the mixed partial derivatives found in Equations (3a,c):

$$\partial_{xz}^2 E_z = \frac{-1}{\varepsilon_o n_e^2}(\varepsilon_o n_o^2 \partial_x^2 E_x + \partial_x^2 P_x + \partial_{xz}^2 P_z), \tag{6a}$$

$$\partial_{xz}^2 E_x = \frac{-1}{\varepsilon_o n_o^2}(\varepsilon_o n_e^2 \partial_z^2 E_z + \partial_{xz}^2 P_x + \partial_z^2 P_z). \tag{6b}$$

Substituting Equation (6a) into Equation (3a), Equation (6b) into Equation (3c), and making the substitution $k^2 = \omega^2 \mu_o \varepsilon_o$ results in the general wave equations

$$\frac{n_o^2}{n_e^2}\partial_x^2 E_x + \partial_z^2 E_x + k^2 n_o^2 E_x = \frac{-\partial_x^2 P_x}{\varepsilon_o n_e^2} - \frac{\partial_{xz}^2 P_z}{\varepsilon_o n_e^2} - \frac{k^2}{\varepsilon_o} P_x, \tag{7a}$$

$$\partial_x^2 E_y + \partial_z^2 E_y + k^2 n_o^2 E_y = \frac{-k^2}{\varepsilon_o} P_y, \tag{7b}$$

$$\partial_x^2 E_z + \frac{n_e^2}{n_o^2}\partial_z^2 E_z + k^2 n_e^2 E_z = \frac{-\partial_{xz}^2 P_x}{\varepsilon_o n_o^2} - \frac{\partial_z^2 P_z}{\varepsilon_o n_o^2} - \frac{k^2}{\varepsilon_o} P_z. \tag{7c}$$

These general wave equations will be used to describe both the pump and the second-harmonic propagation within the $LiNbO_3$. When used to describe the pump propagation, the nonlinear driving terms or source polarizations P_i on the right side of Equations (7a-c) are set to zero; n_o and n_e are taken at the pump wavelength λ_p; and the wave vector k becomes $k_p = \omega_p^2 \mu_o \varepsilon_o = 2\pi/\lambda_p$.

For second-harmonic wave propagation the nonlinear driving terms are retained, n_o and n_e are taken at the second harmonic wavelength λ_s, and the

wave vector k becomes $k_s = \omega_s^2 \mu_o \varepsilon_o = 2\pi/\lambda_s$. Note that the homogeneous portions of Equations (7a-c) are completely uncoupled. Also, the partial derivatives of P_x and P_z will correspond to the "effective" nonlinear coefficients described by many authors.

2.2 Single-Pass Analysis

This first approach to describing the second-harmonic signal uses simple ray propagation. The input pump and generated second-harmonic waves are treated in a stepwise fashion as they propagate through the media. Figure 2.2 illustrates all the *e*-polarized pump and second-harmonic fields associated with the single-pass approach.

2.2.1 Single-Pass Pump

In order to express the SHG output field in terms of the input field, a full treatment of the pump propagation through the system must be undertaken. Here, I calculate the Fresnel reflection and transmission coefficients for the uniaxial media. Figure 2.3 depicts the pump waves incident, transmitted, and reflected from the first surface of the sample as well as the wave vectors associated with each of these fields. The pump wave incident on the sample

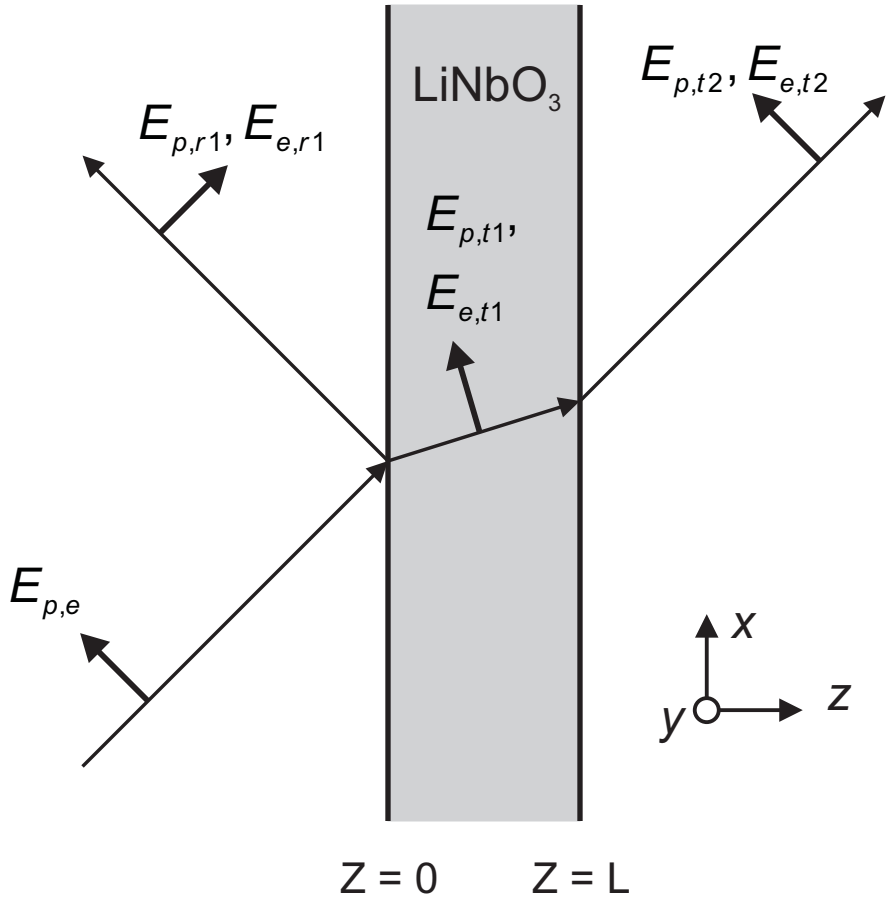

Figure 2.2 *e*-polarized pump and SHG fields propagating through the sample.

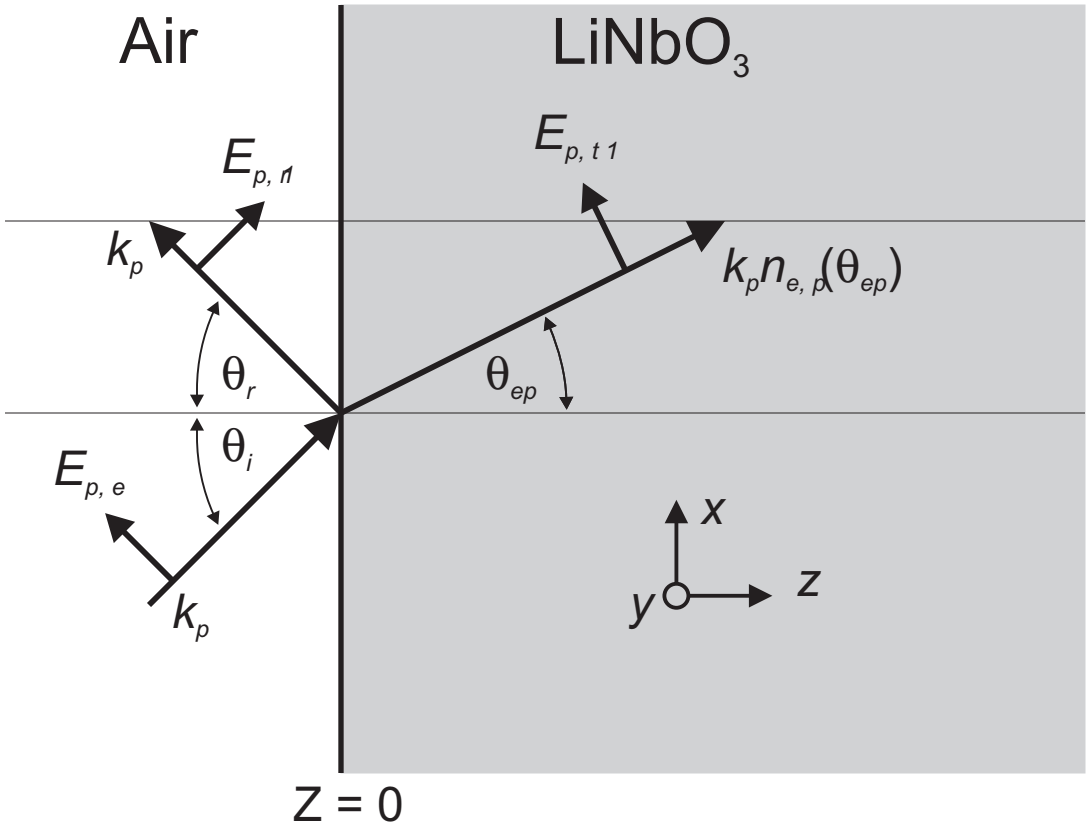

Figure 2.3 Pump fields and wave vectors associated with the first surface of the sample.

for the *e*-polarized pump may be written as

$$\vec{E}_{p,e} = \hat{x}E_{p,x} + \hat{z}E_{p,z} = \hat{x}E^{o}_{p,x}e^{i(K_{xp}x+K_{zp}z-\omega_p t)} + \hat{z}E^{o}_{p,z}e^{i(K_{xp}x+K_{zp}z-\omega_p t)}, \qquad (8)$$

where $K_{xp} = k_p \sin\theta_i$, $K_{zp} = k_p \cos\theta_i$, ω_p is the angular frequency of the pump, and θ_i is the incident angle of the pump. The waves reflected from the first surface may be represented as

$$E_{p,r1,x} = E^{o}_{p,r1,x}e^{i(K_{xr1p}x-K_{zr1p}z-\omega_p t)}, \qquad (9a)$$

$$E_{p,r1,z} = E^{o}_{p,r1,z}e^{i(K_{xr1p}x-K_{zr1p}z-\omega_p t)}, \qquad (9b)$$

where $K_{xr1p} = k_p \sin\theta_{r1}$, $K_{zr1p} = k_p \cos\theta_{r1}$, and θ_{r1} is the angle of reflection for the pump beam. The pump field transmitted through the first surface of the sample must be a solution to the homogeneous portion of the wave equations, that is, Equations (7a,c) with the right side set equal to zero. These solutions may be written in the form

$$E_{p,t1,x} = E^{o}_{p,t1,x}e^{i(K_{pex}x+K_{pez}z-\omega_p t)}, \qquad (10a)$$

$$E_{p,t1,z} = E^{o}_{p,t1,z}e^{i(K_{pex}x+K_{pez}z-\omega_p t)}, \qquad (10b)$$

where $K_{pex} = k_p n_{ep}(\theta_{ep}) \sin\theta_{ep}$, $K_{pez} = k_p n_{ep}(\theta_{ep}) \cos\theta_{ep}$, and θ_{ep} is the angle of propagation through the sample of the *e*-polarized pump field. An expression for the extraordinary index of refraction as a function of angle $n_{e,p}(\theta_{ep})$ is obtained by applying the solution of Equation (10a) to the homogeneous portion of Equation (7a). This leads to the well known expression [see for example Hecht ‘87]

$$n_{e,p}^2(\theta_{ep}) = \frac{n_{o,p}^2 n_{e,p}^2}{n_{o,p}^2 \sin^2\theta_{ep} + n_{e,p}^2 \cos^2\theta_{ep}}, \tag{11}$$

in terms of our definition of θ_{ep}.

In order to solve for the field amplitudes in Equations (9a,b) and (10a,b) the boundary conditions at the first surface of the lithium niobate substrate, z = 0, must be examined. The boundary conditions require the tangential field components be equal across a surface. This leads to

$$\left(E_{p,x} + E_{p,r1,x}\right)\Big|_{z=0} = E_{p,t1,x}\Big|_{z=0}, \tag{12a}$$

$$\left(H_{p,y} + H_{p,r1,y}\right)\Big|_{z=0} = H_{p,t1,y}\Big|_{z=0}. \tag{12b}$$

Substituting the appropriate fields into Equations (12a,b) yields

$$E_{p,x}^o e^{iK_{xp}x} + E_{p,r1,x}^o e^{iK_{xr1p}x} = E_{p,t1,x}^o e^{iK_{pex}x}, \tag{13a}$$

$$\begin{aligned}\left(-K_{xp}E_{p,z}^o + K_{zp}E_{p,x}^o\right)e^{iK_{xp}x} - \left(K_{xr1p}E_{p,r1,z}^o + K_{zr1p}E_{p,r1,x}^o\right)e^{iK_{xr1p}x} \\ = \left(-K_{pex}E_{p,t1,z}^o + K_{pez}E_{p,t1,x}^o\right)e^{iK_{pex}x}.\end{aligned} \tag{13b}$$

To satisfy these equations, the amplitudes on the left must equal the amplitudes on the right and the transverse phases must be equal everywhere on the boundary. These requirements lead to

$$E_{p,x}^o + E_{p,r1,x}^o = E_{p,t1,x}^o, \tag{14a}$$

$$\begin{aligned}-K_{xp}E_{p,z}^o + K_{zp}E_{p,x}^o - K_{xr1p}E_{p,r1,z}^o - K_{zr1p}E_{p,r1,x}^o = \\ -K_{pex}E_{p,t1,z}^o + K_{pez}E_{p,t1,x}^o,\end{aligned} \tag{14b}$$

$$K_{xp} = K_{xr1p} = K_{pex}. \tag{14c}$$

Equation (14c) leads directly to the law of reflection

$$\sin\theta_i = \sin\theta_{r1}. \tag{15a}$$

and Snell's law generalized to the air-uniaxial interface

$$\sin\theta_i = n_{e,p}(\theta_{ep})\sin\theta_{ep}. \tag{15b}$$

The field amplitudes $E^o_{p,z}$, $E^o_{p,r1,z}$, and $E^o_{p,t1,z}$ found in Equation (14b) may be written in terms of $E^o_{p,x}$, $E^o_{p,r1,x}$, and $E^o_{p,t1,x}$ by using $\vec{\nabla}\bullet\vec{D}=0$. This leads to the expressions

$$E^o_{p,z} = -\frac{K_{xp}}{K_{zp}}E^o_{p,x} = -\tan\theta_i \cdot E^o_{p,x}, \tag{16a}$$

$$E^o_{p,r1,z} = \frac{K_{xp}}{K_{zp}}E^o_{p,r1,x} = \tan\theta_i \cdot E^o_{p,r1,x}, \tag{16b}$$

$$E^o_{p,t1,z} = -\frac{n^2_{o,p}}{n^2_{e,p}}\frac{K_{pex}}{K_{pez}}E^o_{p,t1,x} = -\frac{n^2_{o,p}}{n^2_{e,p}}\tan\theta_{ep} \cdot E^o_{p,t1,x}. \tag{16c}$$

The *x*-component of the transmitted pump field $E^o_{p,t1,x}$ may be found by combining Equations (14a,b), (16a-c), and making the substitutions $K_{xr1p} = K_{xp}$ and $K_{zr1p} = K_{zp}$. The result is

$$E^o_{p,t1,x} = \frac{2\cos\theta_{ep}}{n_{e,p}(\theta_{ep})\cos\theta_i\left(\frac{n^2_{o,p}}{n^2_{e,p}}\sin^2\theta_{ep}+\cos^2\theta_{ep}\right)+\cos\theta_{ep}}E^o_{p,x}. \tag{17}$$

In order to represent this relationship in terms of the total incident pump field the following expression is used

$$\left|E_{p,e}\right|^2 = \left|E_{p,x}\right|^2 + \left|E_{p,z}\right|^2 = \frac{1}{\cos^2\theta_i}\left|E_{p,x}\right|^2. \tag{18}$$

Equation (17) can now be written as

$$E^{o}_{p,t1,x} = t1_e \cos\theta_{ep} E^{o}_{p,e}, \tag{19}$$

where the transmission coefficient is

$$t1_e = \frac{2\cos\theta_i}{n_{e,p}(\theta_{ep})\cos\theta_i\left(\frac{n^2_{o,p}}{n^2_{e,p}}\sin^2\theta_{ep} + \cos^2\theta_{ep}\right) + \cos\theta_{ep}}. \tag{20}$$

Following a similar procedure as above, the reflected field amplitude is

$$E^{o}_{p,r1,x} = r1_e \cdot \cos\theta_i \cdot E^{o}_{p,e}, \tag{21}$$

where the reflection coefficient is

$$r1_e = \frac{\cos\theta_{ep} - n_{e,p}(\theta_{ep})\cos\theta_i\left(\frac{n^2_{o,p}}{n^2_{e,p}}\sin^2\theta_{ep} + \cos^2\theta_{ep}\right)}{n_{e,p}(\theta_{ep})\cos\theta_i\left(\frac{n^2_{o,p}}{n^2_{e,p}}\sin^2\theta_{ep} + \cos^2\theta_{ep}\right) + \cos\theta_{ep}}. \tag{22}$$

Examining these coefficients reveals the subtle differences between the transmission and reflection coefficients for uniaxial and isotropic media. If $n_{o,p}$ and $n_{e,p}$ were equal, Equations (20) and (22) would simplify to the commonly published transmission and reflection coefficients for isotropic materials; see for example [Möller ‘88] or [Hecht ‘87]. The perturbation to these coefficients due to factors of n_{op}/n_{ep} is very slight. This fact is illustrated in Figure 2.4 (a), where the transmittance, the square of Equation (20), is plotted for three separate cases. The first case is for $LiNbO_3$, the second for an isotropic medium with $n = n_{op}$, and the last for an isotropic medium with $n = n_{ep}$. Figure 2.4 (b) provides a similar comparison for the reflectance, obtained by squaring Equation (22). Figures 2.4 (a) and (b) show that the uniaxial curves for $LiNbO_3$ follow very closely the isotropic curves for $n = n_{op}$.

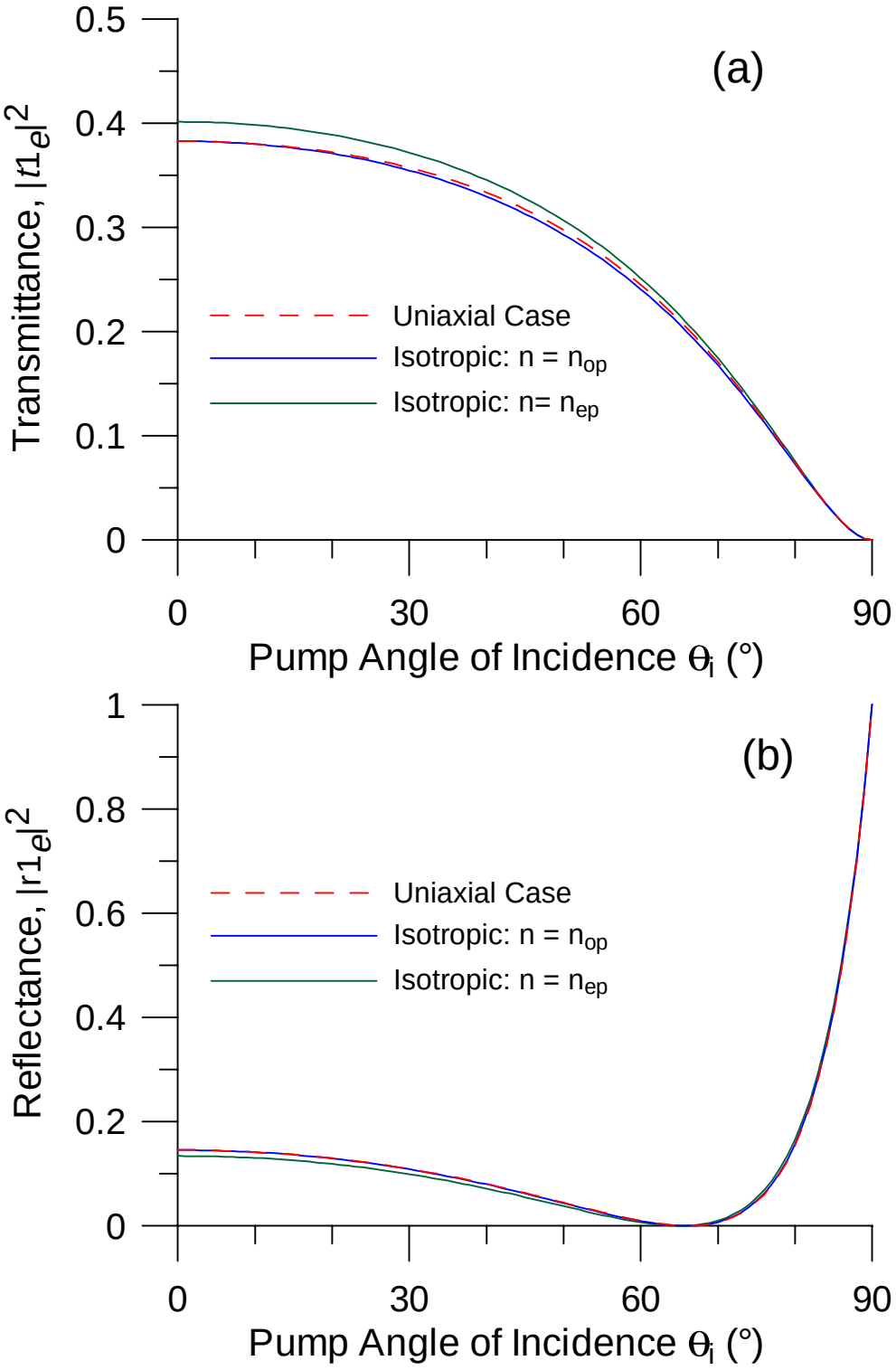

Figure 2.4 Transmittance (a) and reflectance (b) comparisons for uniaxial and isotropic media. The red lines are for uniaxial $LiNbO_3$. The blue lines are for an isotropic medium with index of refraction equal to the ordinary index of $LiNbO_3$. The green lines are for an isotropic medium with an index of refraction equal to the extraordinary index of $LiNbO_3$.

This is because at $\theta_i = 0°$ the pump wave sees only the ordinary index of refraction.

Propagating the transmitted pump field through the substrate to the second surface results in a second set of reflected and transmitted waves and a second set of boundary conditions, as illustrated in Figure 2.5. The reflected and transmitted waves from the second surface may be represented as

$$E_{p,r2,x} = E^{o}_{p,r2,x} e^{i(K_{pexr2}x - K_{pezr2}(z-L) - \omega_p t)}, \tag{23a}$$

$$E_{p,r2,z} = E^{o}_{p,r2,z} e^{i(K_{pexr2}x - K_{pezr2}(z-L) - \omega_p t)}, \tag{23b}$$

and

$$E_{p,t2,x} = E^{o}_{p,t2,x} e^{i(K_{pxt2}x + K_{pzt2}(z-L) - \omega_p t)}, \tag{24a}$$

$$E_{p,t2,z} = E^{o}_{p,t2,z} e^{i(K_{pxt2}x + K_{pzt2}(z-L) - \omega_p t)}, \tag{24b}$$

where

$$K_{pexr2} = k_p n_{ep}(\theta_{r2}) \sin\theta_{r2}, \tag{25a}$$

$$K_{pezr2} = k_p n_{ep}(\theta_{r2}) \cos\theta_{r2}, \tag{25b}$$

$$K_{pxt2} = k_p \sin\theta_{t2}, \tag{25c}$$

$$K_{pzt2} = k_p \cos\theta_{t2}, \tag{25d}$$

and L is the sample thickness.

Examining the phases associated with the boundary conditions

$$\left(E_{p,t1,x} + E_{p,r2,x}\right)\Big|_{z=L} = E_{p,t2,x}\Big|_{z=L}, \tag{26a}$$

$$\left(H_{p,t1,y} + H_{p,r2,y}\right)\Big|_{z=L} = H_{p,t2,y}\Big|_{z=L} \tag{26b}$$

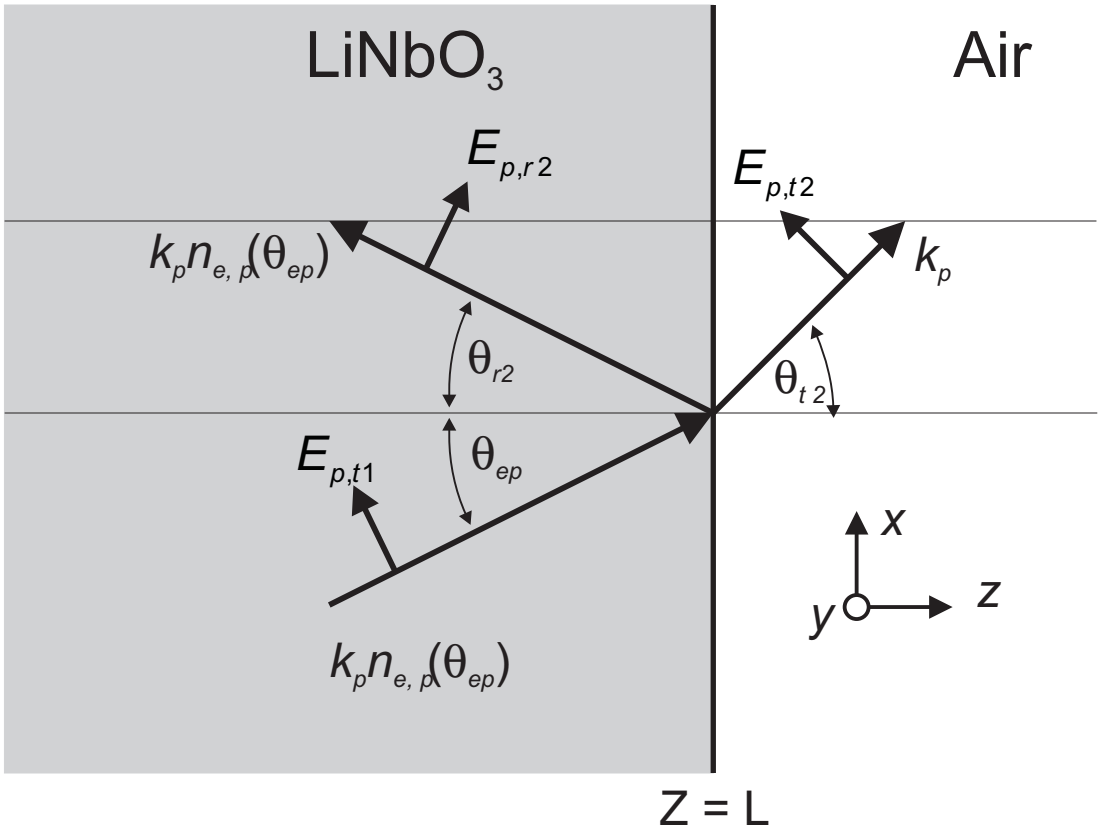

Figure 2.5 Second surface electric fields and wave vectors.

at the second surface, $z = L$, leads to the obvious redefinition of the phases in Equations (25a-d) to

$$K_{pexr2} = K_{pex}, \tag{27a}$$

$$K_{pezr2} = K_{pez}, \tag{27b}$$

$$K_{pxt2} = K_{xp}, \tag{27c}$$

$$K_{pzt2} = K_{zp}. \tag{27d}$$

Writing the amplitude equations

$$E^o_{p,t1,x} e^{iK_{pez}L} + E^o_{p,r2,x} = E^o_{p,t2,x}, \tag{28a}$$

$$\begin{aligned}\left(-K_{pex}E^o_{p,t1,z} + K_{pez}E^o_{p,t1,x}\right)e^{iK_{pez}L} - K_{pex}E^o_{p,r2,z} - K_{pez}E^o_{p,r2,x} = \\ - K_{xp}E^o_{p,t2,z} + K_{zp}E^o_{p,t2,x},\end{aligned} \tag{28b}$$

associated with the boundary conditions in Equations (26a,b) shows the accumulation of phase associated with the pump propagation through the sample. Writing $E^o_{p,r2,z}$ and $E^o_{p,t2,z}$ in terms of $E^o_{p,r2,x}$ and $E^o_{p,t2,x}$ by using $\vec{\nabla} \bullet \vec{D} = 0$ yields

$$E^o_{p,r2,z} = \frac{n^2_{o,p}}{n^2_{e,p}} \frac{K_{pex}}{K_{pez}} E^o_{p,r2,x} = \frac{n^2_{o,p}}{n^2_{e,p}} \tan\theta_{ep} E^o_{p,r2,x}, \tag{29a}$$

$$E^o_{p,t2,z} = -\frac{K_{xp}}{K_{zp}} E^o_{p,t2,x} = -\tan\theta_i E^o_{p,t2,x}. \tag{29b}$$

Combining Equations (16c), (28a,b), and (29a,b) results in expressions for the transmitted and reflected pump field amplitudes at the second surface of the substrate:

$$E^{o}_{p,t2,x} = \frac{2n_{e,p}(\theta_{ep})\cos\theta_i\left(\frac{n^2_{o,p}}{n^2_{e,p}}\sin^2\theta_{ep}+\cos^2\theta_{ep}\right)}{n_{e,p}(\theta_{ep})\cos\theta_i\left(\frac{n^2_{o,p}}{n^2_{e,p}}\sin^2\theta_{ep}+\cos^2\theta_{ep}\right)+\cos\theta_{ep}}E^{o}_{p,t1,x}e^{iK_{pez}L}, \quad (30a)$$

$$E^{o}_{p,r2,x} = \frac{n_{e,p}(\theta_{ep})\cos\theta_i\left(\frac{n^2_{o,p}}{n^2_{e,p}}\sin^2\theta_{ep}+\cos^2\theta_{ep}\right)-\cos\theta_{ep}}{n_{e,p}(\theta_{ep})\cos\theta_i\left(\frac{n^2_{o,p}}{n^2_{e,p}}\sin^2\theta_{ep}+\cos^2\theta_{ep}\right)+\cos\theta_{ep}}E^{o}_{p,t1,x}e^{iK_{pez}L}. \quad (30b)$$

Expressing Equations (30a,b) in terms of the incident pump field by using Equation (18) results in

$$E^{o}_{p,t2,x} = t1_e \cdot t2_e \cdot \cos\theta_i \cdot E^{o}_{p,e}e^{iK_{pez}L}, \quad (31a)$$

$$E^{o}_{p,r2,x} = t1_e \cdot r2_e \cdot \cos\theta_{ep} \cdot E^{o}_{p,e}e^{iK_{pez}L}, \quad (31b)$$

where the second-surface transmission and reflection coefficients are

$$t2_e = \frac{2n_{e,p}(\theta_{ep})\cos\theta_{ep}\left(\frac{n^2_{o,p}}{n^2_{e,p}}\sin^2\theta_{ep}+\cos^2\theta_{ep}\right)}{n_{e,p}(\theta_{ep})\cos\theta_i\left(\frac{n^2_{o,p}}{n^2_{e,p}}\sin^2\theta_{ep}+\cos^2\theta_{ep}\right)+\cos\theta_{ep}}, \quad (32a)$$

$$r2_e = \frac{n_{e,p}(\theta_{ep})\cos\theta_i\left(\frac{n^2_{o,p}}{n^2_{e,p}}\sin^2\theta_{ep}+\cos^2\theta_{ep}\right)-\cos\theta_{ep}}{n_{e,p}(\theta_{ep})\cos\theta_i\left(\frac{n^2_{o,p}}{n^2_{e,p}}\sin^2\theta_{ep}+\cos^2\theta_{ep}\right)+\cos\theta_{ep}} = -r1_e. \quad (32b)$$

This concludes the single-pass, *e*-polarized pump discussion. This same procedure may be applied to the case of an *o*-polarized pump field as depicted in Figure 2.6. For the *o*-polarized pump

$$\vec{E}^{o}_{p,o} = \hat{y}E_{p,y} = E^{o}_{p,y}e^{i(K_{xp}x+K_{zp}z-\omega_p t)}, \tag{33}$$

the transmitted and reflected pump fields are

$$E^{o}_{p,t1,y} = t1_o \cdot E^{o}_{p,o}, \tag{33a}$$

$$E^{o}_{p,r1,y} = r1_o \cdot E^{o}_{p,o}, \tag{33b}$$

$$E^{o}_{p,t2,y} = t1_o \cdot t2_o \cdot E^{o}_{p,o}e^{iK_{poz}L}, \tag{33c}$$

$$E^{o}_{p,r2,y} = t1_o \cdot r2_o \cdot E^{o}_{p,o}e^{iK_{poz}L}, \tag{33d}$$

where the *o*-polarized transmission and reflection coefficients are

$$t1_o = \frac{2\cos\theta_i}{n_{o,p}\cos\theta_{op} + \cos\theta_i}, \tag{34a}$$

$$r1_o = \frac{\cos\theta_i - n_{o,p}\cos\theta_{op}}{n_{o,p}\cos\theta_{op} + \cos\theta_i}, \tag{34b}$$

$$t2_o = \frac{2n_{o,p}\cos\theta_{op}}{n_{o,p}\cos\theta_{op} + \cos\theta_i}, \tag{34c}$$

$$r2_o = \frac{n_{o,p}\cos\theta_{op} - \cos\theta_i}{n_{o,p}\cos\theta_{op} + \cos\theta_i} = -r1_o, \tag{34d}$$

$K_{poz} = k_p n_{o,p}\cos\theta_{op}$, and θ_{op} is the angle of propagation through the sample of the *o*-polarized pump field.

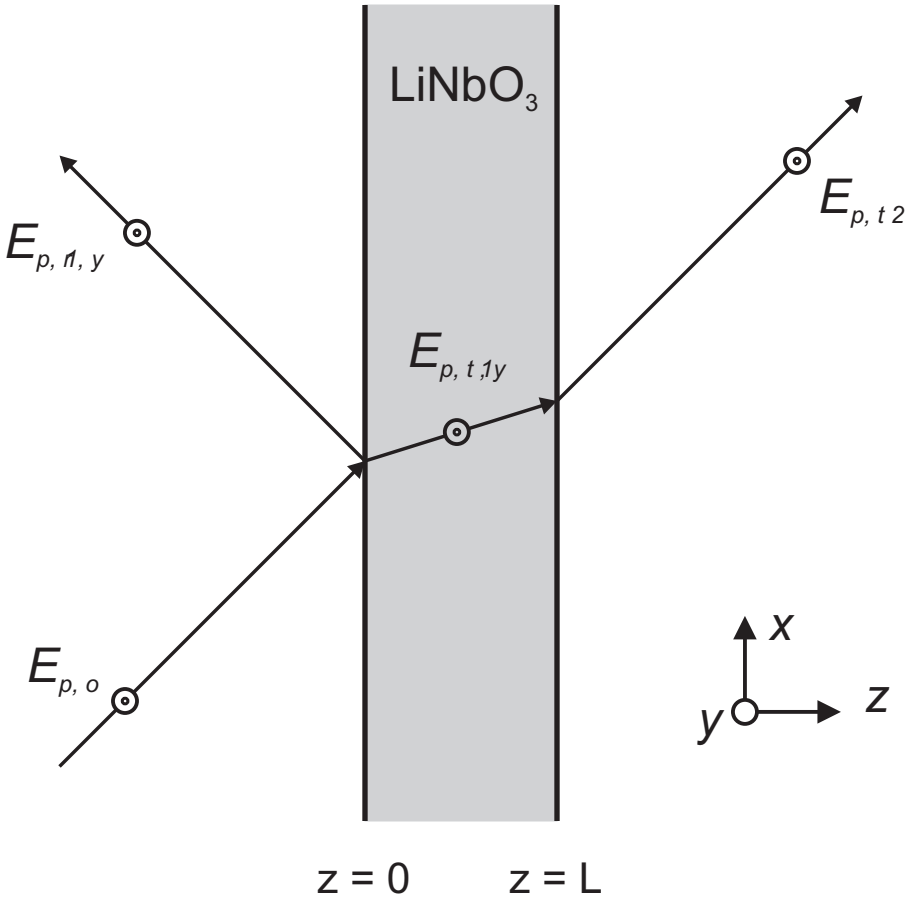

Figure 2.6 o-polarized pump fields propagating through the sample.

2.2.2 Single-Pass Second-Harmonic Generation

The development of the second-harmonic field must now be examined. The second-harmonic field is generated by the second-order nonlinear source polarizations found on the right side of Equations (7a-c). These polarizations arise from the interaction of the pump field with the nonlinear material through the action of the second-order susceptibilities. As described by [Shen '84] various definitions are found in the literature for nonlinear susceptibilities. This has led to considerable confusion in interpreting the value of the nonlinear susceptibilities within factors of 2 and ε_o. Shen represents the second-harmonic source polarization as $P = \chi^{(2)}EE$ where P and E are complex quantities. He also notes that several authors [for example, Yariv '84] represent P and E as real quantities using the nonlinear coefficient $d^{(2)}$ resulting in $P = d^{(2)}EE$. Using $d^{(2)}$ to connect the complex polarization and electric fields results in $P = 2d^{(2)}EE$. In this representation $d^{(2)}$ is in units of C/V^2. Following [Kurtz '79], I have chosen to represent the nonlinear polarization as $P = 2\varepsilon_o d^{(2)}EE$ where $d^{(2)}$ is in units of m/V, as it is in most reference books. Writing the nonlinear source polarization for $LiNbO_3$ in matrix notation results in

$$\begin{bmatrix} P_x \\ P_y \\ P_z \end{bmatrix} = 2\varepsilon_o \begin{bmatrix} 0 & 0 & 0 & 0 & d_{15}^{(2)} & -d_{22}^{(2)} \\ -d_{22}^{(2)} & d_{22}^{(2)} & 0 & d_{15}^{(2)} & 0 & 0 \\ d_{31}^{(2)} & d_{31}^{(2)} & d_{33}^{(2)} & 0 & 0 & 0 \end{bmatrix} \begin{bmatrix} E_{p,t1,x}^2 \\ E_{p,t1,y}^2 \\ E_{p,t1,z}^2 \\ 2E_{p,t1,z}E_{p,t1,y} \\ 2E_{p,t1,z}E_{p,t1,x} \\ 2E_{p,t1,x}E_{p,t1,y} \end{bmatrix}. \quad (35)$$

For an *e*-polarized pump, the pump field transmitted into the $LiNbO_3$ sample is

$$\vec{E}_{p,t1} = \hat{x}E_{p,t1,x} + \hat{z}E_{p,t1,z} = \hat{x}E_{p,t1,x}^{o}e^{i\varphi} + \hat{z}E_{p,t1,z}^{o}e^{i\varphi}, \quad (36)$$

where $\varphi = k_p n_{e,p}(\theta_{ep})\sin(\theta_{ep})x + k_p n_{e,p}(\theta_{ep})\cos(\theta_p)z - \omega_p t$. For this pump and sample arrangement, the nonlinear source polarization becomes

$$\vec{P} = 2\varepsilon_o[\hat{x}(d_{15}^{(2)}2E_{p,t1,z}E_{p,t1,x}) - \hat{y}(d_{22}^{(2)}E_{p,t1,x}^2) + \hat{z}(d_{31}^{(2)}E_{p,t1,x}^2 + d_{33}^{(2)}E_{p,t1,z}^2)]. \quad (37)$$

Examining the product of the electric fields in this expression shows that $E_{p,t1,j}E_{p,t1,k} = E_{p,t1,j}^{o}E_{p,t1,k}^{o}e^{2i\varphi}$, where *j* and *k* may be *x* or *z*. Recognizing that $k_s=2\pi/\lambda_s=2k_p$ and $\omega_s=2\omega_p$ allows for the phase of the nonlinear source polarization to be written in terms of the second-harmonic wavelength and frequency:

$$2\varphi = \varphi_s = k_s n_{e,p}(\theta_{ep})\sin(\theta_p)x + k_s n_{e,p}(\theta_{ep})\cos(\theta_p)z - \omega_s t, \quad (38)$$

instead of the fundamental wavelength and frequency.

The nonlinear source polarizations that appear on the right side of Equations (7a-c) are now defined. Solving Equations (7a-c) for the second-harmonic fields may now be accomplished. The solution to these

inhomogeneous wave equations can be found by adding a particular solution to the homogeneous solution. The homogeneous and particular solutions represent the “free” and “bound” second-harmonic waves mentioned in the introduction. The particular solution is bound to the propagation of the pump wave while the homogeneous solution is not. Figure 2.7(a) illustrates the *e*-polarized second-harmonic fields associated with the first boundary while Figure 2.7 (b) represents these fields’ wave vectors. The fields $E^{h}_{e,t1}$ and $E^{p}_{e,t1}$ represent the two portions of the total second-harmonic field propagating through the sample. The homogeneous equations, obtained by setting all driving terms to zero, have plane wave solutions of the form

$$E^{h}_{e,t1,x} = E^{o}_{e,t1,x} e^{i(K_{xes}x + K_{zes}z - \omega_s t)}, \tag{39a}$$

$$E^{h}_{e,t1,z} = E^{o}_{e,t1,z} e^{i(K_{xes}x + K_{zes}z - \omega_s t)} \tag{39b}$$

for the *e*-polarized second-harmonic field, where $K_{xes} = k_s n_{e,s}(\theta_{es}) \sin\theta_{es}$, $K_{zes} = k_s n_{e,s}(\theta_{es}) \cos\theta_{es}$, and θ_{es} is the angle of propagation of the *e*-polarized second-harmonic field inside the sample. The extraordinary index of refraction at the second-harmonic wavelength as a function of angle $n_{e,s}(\theta_{es})$ may be solved as it was for the pump wavelength

$$n^2_{e,s}(\theta_{es}) = \frac{n^2_{o,s} n^2_{e,s}}{n^2_{o,s} \sin^2 \theta_{es} + n^2_{e,s} \cos^2 \theta_{e,s}} \tag{40}$$

in terms of our definition of θ_{es}. Figure 2.8 shows how $n_{e,s}(\theta_{es})$ varies from the ordinary index at $\theta_{es} = 0°$ to the extraordinary index at $\theta_{es} = 90°$.

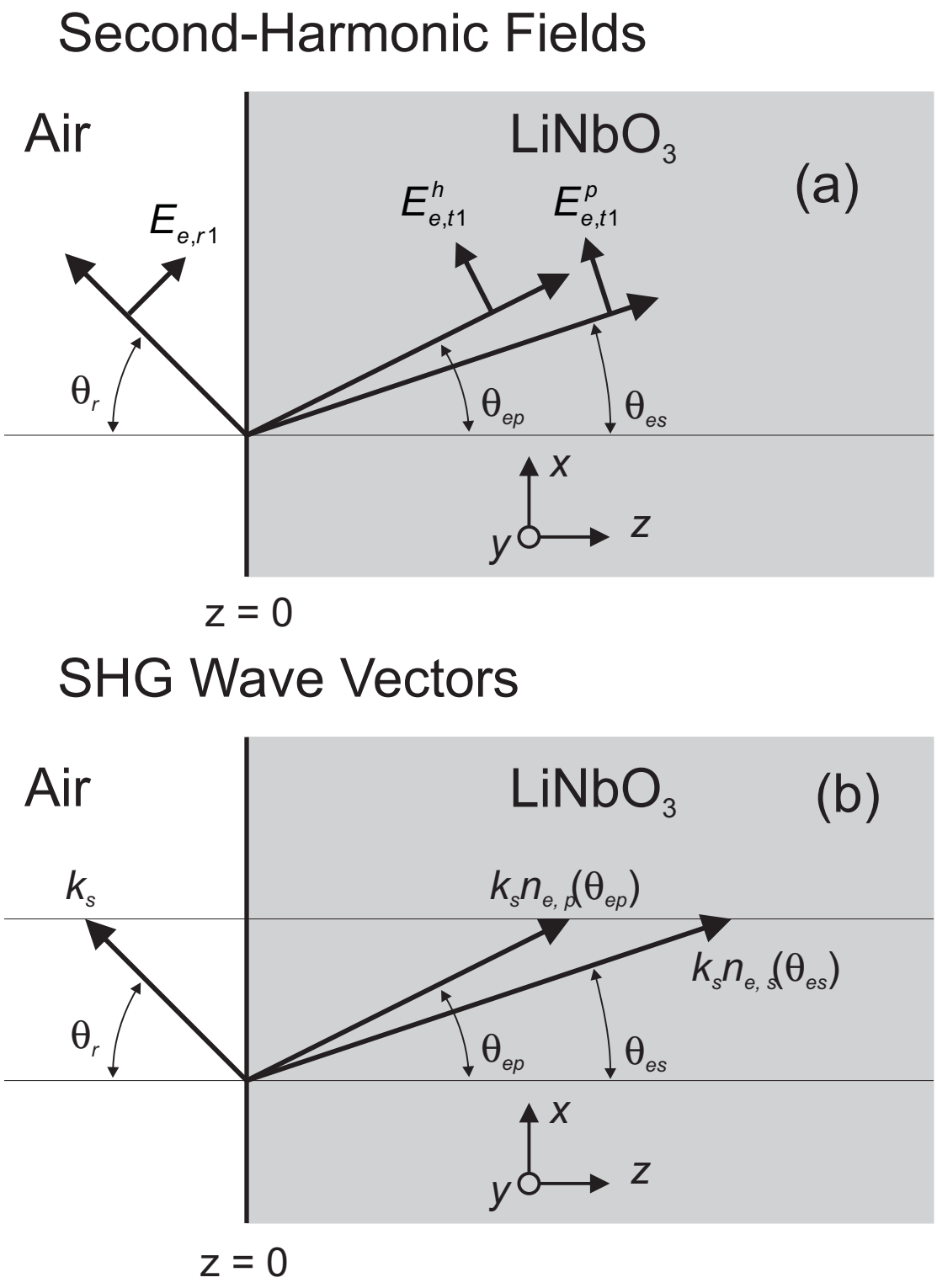

Figure 2.7 First surface electric fields (a) and wave vectors (b).

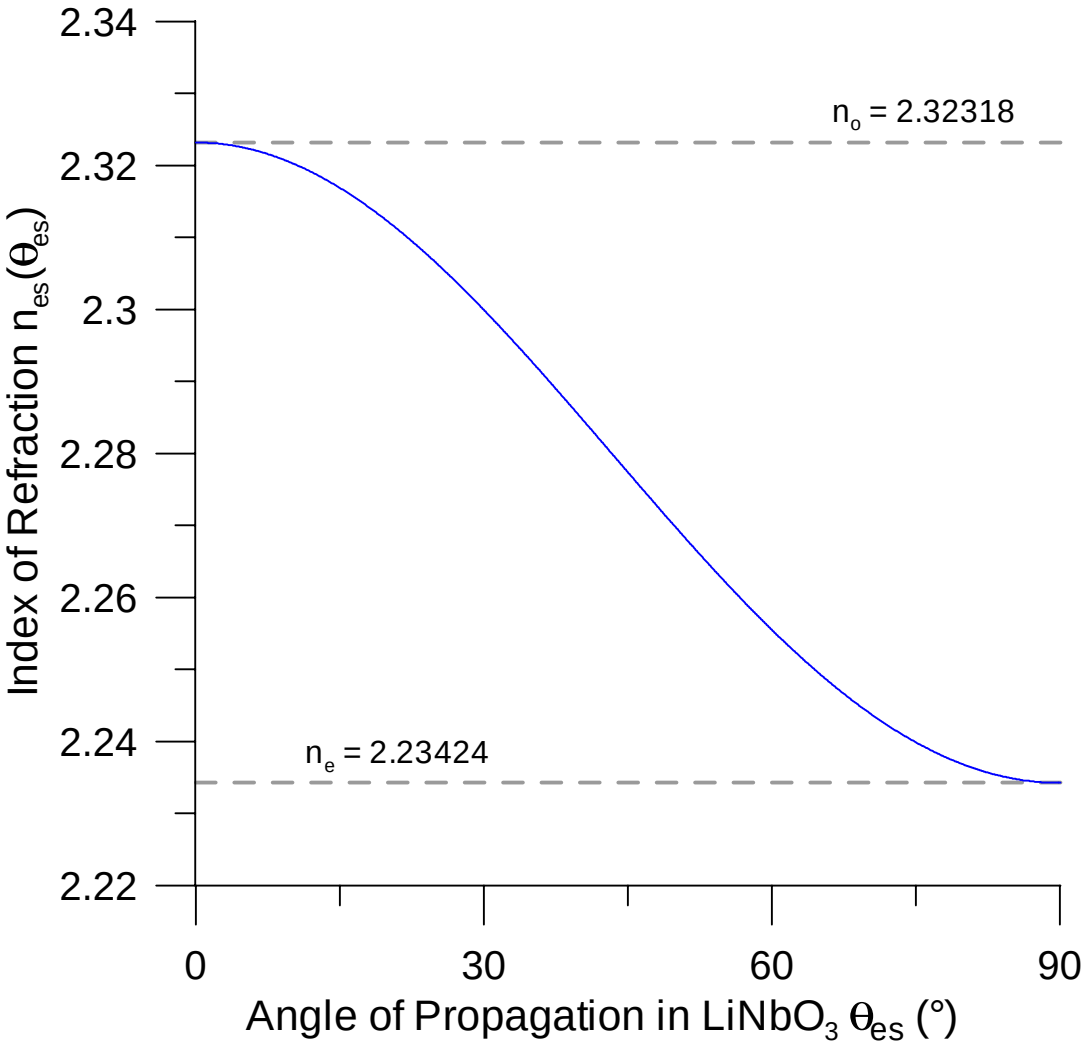

Figure 2.8 The index of refraction for the second-harmonic wavelength as a function of propagation angle in $LiNbO_3$.

The particular solutions to Equations (7a-c) may be written as

$$E^{p}_{e,t1,x} = A_{e,t1,x} e^{i(K_{xep}x + K_{zep}z - \omega_s t)}, \tag{41a}$$

$$E^{p}_{e,t1,z} = A_{e,t1,z} e^{i(K_{xep}x + K_{zep}z - \omega_s t)}, \tag{41b}$$

where $K_{xep} = k_s n_{e,p}(\theta_{ep}) \sin\theta_{ep}$ and $K_{zep} = k_s n_{e,p}(\theta_{ep}) \cos\theta_{ep}$. Therefore, the general solutions are

$$E_{e,t1,x} = E^{o}_{e,t1,x} e^{i(K_{xes}x + K_{zes}z - \omega_s t)} + A_{e,t1,x} e^{i(K_{xep}x + K_{zep}z - \omega_s t)}, \tag{42a}$$

$$E_{e,t1,z} = E^{o}_{e,t1,z} e^{i(K_{xes}x + K_{zes}z - \omega_s t)} + A_{e,t1,z} e^{i(K_{xep}x + K_{zep}z - \omega_s t)}. \tag{42b}$$

The *x*-oriented field amplitude of the particular solution for an *e*-polarized pump $A_{e,t1,x}$ may be found by substituting Equation (41a) into Equation (7a) and using Equation (37):

$$A_{e,t1,x} = \frac{4d^{(2)}_{15}\left(K^2_{xep} - k_s^2 n^2_{e,s}\right)E^{o}_{p,t1,x}E^{o}_{p,t1,z}}{\left(k_s^2 n^2_{o,s} n^2_{e,s} - n^2_{o,s}K^2_{xep} - n^2_{e,s}K^2_{zep}\right)} + \frac{2K_{xep}K_{zep}\left(d^{(2)}_{31}\left(E^{o}_{p,t1,x}\right)^2 + d^{(2)}_{33}\left(E^{o}_{p,t1,z}\right)^2\right)}{\left(k_s^2 n^2_{o,s} n^2_{e,s} - n^2_{o,s}K^2_{xep} - n^2_{e,s}K^2_{zep}\right)}. \tag{43}$$

Similarly the *z*-oriented field amplitude of the particular solution for an *e*-polarized pump $A_{e,t1,z}$ is

$$A_{e,t1,z} = \frac{4d^{(2)}_{15}K_{xep}K_{zep}E^{o}_{p,t1,x}E^{o}_{p,t1,z}}{\left(k_s^2 n^2_{o,s} n^2_{e,s} - n^2_{o,s}K^2_{xep} - n^2_{e,s}K^2_{zep}\right)} + \frac{2\left(K^2_{zep} - k_s^2 n^2_{o,s}\right)\left(d^{(2)}_{31}\left(E^{o}_{p,t1,x}\right)^2 + d^{(2)}_{33}\left(E^{o}_{p,t1,z}\right)^2\right)}{\left(k_s^2 n^2_{o,s} n^2_{e,s} - n^2_{o,s}K^2_{xep} - n^2_{e,s}K^2_{zep}\right)}. \tag{44}$$

It is convenient to express these amplitudes in terms of the input pump field. The pump field amplitude products found in Equations (43) and (44) may be written in terms of the input pump field by using Equations (16c) and (19):

$$\left(E^{o}_{p,r2,x}\right)^2 = t1^2_e \cos^2\theta_{ep}\left(E^{o}_{p,e}\right)^2 e^{i2K_{pez}L}, \tag{45a}$$

$$\left(E^{o}_{p,r2,z}\right)^2 = \frac{n^4_{op}}{n^4_{ep}}\tan^2\theta_{ep} t1^2_e \cos^2\theta_{ep}\left(E^{o}_{p,e}\right)^2 e^{i2K_{pez}L}, \tag{45b}$$

$$E^{o}_{p,r2,x}\cdot E^{o}_{p,r2,z} = \frac{n^2_{op}}{n^2_{ep}}\tan\theta_{ep} t1^2_e \cos^2\theta_{ep}\left(E^{o}_{p,e}\right)^2 e^{i2K_{pez}L}. \tag{45c}$$

Recognizing that $K_{zep} = 2K_{pez}$ and substituting Equations (45a-c) into Equations (43) and (44) results in the following expressions for the field amplitudes of the particular solution in terms of the input pump field:

$$A_{e,t1,x} = \left\{ \begin{array}{l} \dfrac{-4d^{(2)}_{15}\left(K^2_{xep} - k^2_s n^2_{e,s}\right)\dfrac{n^2_{o,p}}{n^2_{e,p}}\tan\theta_{ep}}{\left(k^2_s n^2_{o,s} n^2_{e,s} - n^2_{o,s}K^2_{xep} - n^2_{e,s}K^2_{zep}\right)} \\ \\ \quad + \dfrac{2K_{xep}K_{zep}\left(d^{(2)}_{31} + d^{(2)}_{33}\dfrac{n^4_{o,p}}{n^4_{e,p}}\tan^2\theta_{ep}\right)}{\left(k^2_s n^2_{o,s} n^2_{e,s} - n^2_{o,s}K^2_{xep} - n^2_{e,s}K^2_{zep}\right)} \end{array} \right\} t1^2_e \cos^2\theta_{ep}\left(E^{o}_{p,e}\right)^2, \tag{46a}$$

$$A_{e,t1,z} = \left\{ \frac{-4d_{15}^{(2)} K_{xep} K_{zep} \dfrac{n_{o,p}^2}{n_{e,p}^2} \tan\theta_{ep}}{\left(k_s^2 n_{o,s}^2 n_{e,s}^2 - n_{o,s}^2 K_{xep}^2 - n_{e,s}^2 K_{zep}^2\right)} \right.$$

$$\left. + \frac{2\left(K_{zep}^2 - k_s^2 n_{o,s}^2\right)\left(d_{31}^{(2)} + d_{33}^{(2)} \dfrac{n_{o,p}^4}{n_{e,p}^4} \tan^2\theta_{ep}\right)}{\left(k_s^2 n_{o,s}^2 n_{e,s}^2 - n_{o,s}^2 K_{xep}^2 - n_{e,s}^2 K_{zep}^2\right)} \right\} t1_e^2 \cos^2\theta_{ep} \left(E_{p,e}^o\right)^2. \tag{46b}$$

Solving for the homogeneous field amplitudes is somewhat more involved. Here the boundary conditions at z = 0 are once again invoked. Representing the reflected second-harmonic field generated from an *e*-polarized pump in its *x*- and *z*-components results in

$$E_{e,r1,x} = E_{e,r1,x}^o e^{i(K_{xs}x - K_{zs}z - \omega_s t)} \text{ and} \tag{47a}$$

$$E_{e,r1,z} = E_{e,r1,z}^o e^{i(K_{xs}x - K_{zs}z - \omega_s t)} \tag{47b}$$

where $K_{xs} = k_s \sin\theta_r$ and $K_{zs} = k_s \cos\theta_r$. The boundary conditions at the first surface for the second-harmonic fields may now be written as

$$E_{e,r1,x}\Big|_{z=0} = E_{e,t1,x}\Big|_{z=0} \text{ and} \tag{48a}$$

$$H_{e,r1,y}\Big|_{z=0} = H_{e,t1,y}\Big|_{z=0}. \tag{48b}$$

Substituting into equations (48a,b) for the various fields leads to

$$E_{e,r1,x}^o e^{i(K_{xs}x)} = E_{e,t1,x}^o e^{i(K_{xes}x)} + A_{e,t1,x} e^{i(K_{xep}x)}, \tag{49a}$$

$$\left(K_{xs}E_{e,r1,z}^o + K_{zs}E_{e,r1,x}^o\right)e^{i(K_{xs}x)} = \left(K_{xes}E_{e,t1,z}^o - K_{zes}E_{e,t1,x}^o\right)e^{i(K_{xes}x)} + \left(K_{xep}A_{e,t1,z} - K_{zep}A_{e,t1,x}\right)e^{i(K_{xep}x)}. \tag{49b}$$

In order for these equations to be satisfied, the amplitudes on the right must equal the amplitudes on the left and all the phases must be equal; that is,

$$E^{o}_{e,r1,x} = E^{o}_{e,t1,x} + A_{e,t1,x}\,, \tag{50a}$$

$$K_{xs}E^{o}_{e,r1,z} + K_{zs}E^{o}_{e,r1,x} = K_{xes}E^{o}_{e,t1,z} - K_{zes}E^{o}_{e,t1,x} + K_{xep}A_{e,t1,z} - K_{zep}A_{e,t1,x}\,, \tag{50b}$$

$$K_{xs} = K_{xes} = K_{xep}\,. \tag{50c}$$

Equation (50c) represents the phase relationships of *e*-polarized reflected and transmitted second-harmonic waves at the first boundary. These phases can be related to the incident pump phase by combining Equations (50c) and (15) resulting in a nonlinear Snell's law:

$$\sin\theta_r = n_{e,s}(\theta_{es})\sin\theta_{es} = n_{e,p}(\theta_{ep})\sin\theta_{ep} = \sin\theta_i\,. \tag{51}$$

All the angles in Equation (51) can now be expressed in terms of the incident pump angle as

$$\theta_r = \theta_i\,, \tag{52a}$$

$$\theta_{es} = \sin^{-1}\left(\frac{n_{e,s}\sin\theta_i}{\sqrt{\left(n_{o,s}n_{e,s}\right)^2 - \left(n^2_{o,s} - n^2_{e,s}\right)\sin^2\theta_i}}\right), \tag{52b}$$

$$\theta_{ep} = \sin^{-1}\left(\frac{n_{e,p}\sin\theta_i}{\sqrt{\left(n_{o,p}n_{e,p}\right)^2 - \left(n^2_{o,p} - n^2_{e,p}\right)\sin^2\theta_i}}\right). \tag{52c}$$

All that is left is to solve for the homogeneous field amplitudes of the *e*-polarized second harmonic waves found in Equations (50a,b). Using the

same technique that was employed for the pump waves, the *z*-oriented components may be expressed in terms of the *x*-oriented components

$$E^{o}_{e,r1,z} = \frac{K_{xs}}{K_{zs}} E^{o}_{e,r1,x}, \tag{53a}$$

$$E^{o}_{e,t1,z} = -\left(\frac{n_{o,s}}{n_{e,s}}\right)^{2} \frac{K_{xes}}{K_{zes}} E^{o}_{e,t1,x}. \tag{53b}$$

Finally, combining Equations (50a,b) and (53a,b) leads to the solution

$$E^{o}_{e,t1,x} = \frac{K_{xep} A_{e,t1,z} - \left(K_{zep} + b_2\right) A_{e,t1,x}}{b_1 + b_2}, \tag{54}$$

where the factors

$$b_1 = \frac{n^2_{o,s}}{n^2_{e,s}} \frac{K^2_{xes}}{K_{zes}} + K_{zes} \text{ and} \tag{55a}$$

$$b_2 = \frac{K^2_{xs}}{K_{zs}} + K_{zs} \tag{55b}$$

are used for simplification.

Propagating the transmitted second-harmonic field through the substrate to the second surface results in a second set of reflected and transmitted waves and a second set of boundary conditions. Figure 2.9 depicts the second-harmonic fields associated with the second surface of the sample. The *e*-polarized reflected and transmitted waves originating from the second surface may be represented as

$$E_{e,r2,x} = E^{o}_{e,r2,x} e^{i(K_{xes}x - K_{zes}(z-L) - \omega_s t)} + A_{e,r2,x} e^{i(K_{xep}x - K_{zep}(z-L) - \omega_s t)}, \tag{56a}$$

$$E_{e,r2,z} = E^{o}_{e,r2,z} e^{i(K_{xes}x - K_{zes}(z-L) - \omega_s t)} + A_{e,r2,z} e^{i(K_{xep}x - K_{zep}(z-L) - \omega_s t)}, \tag{56b}$$

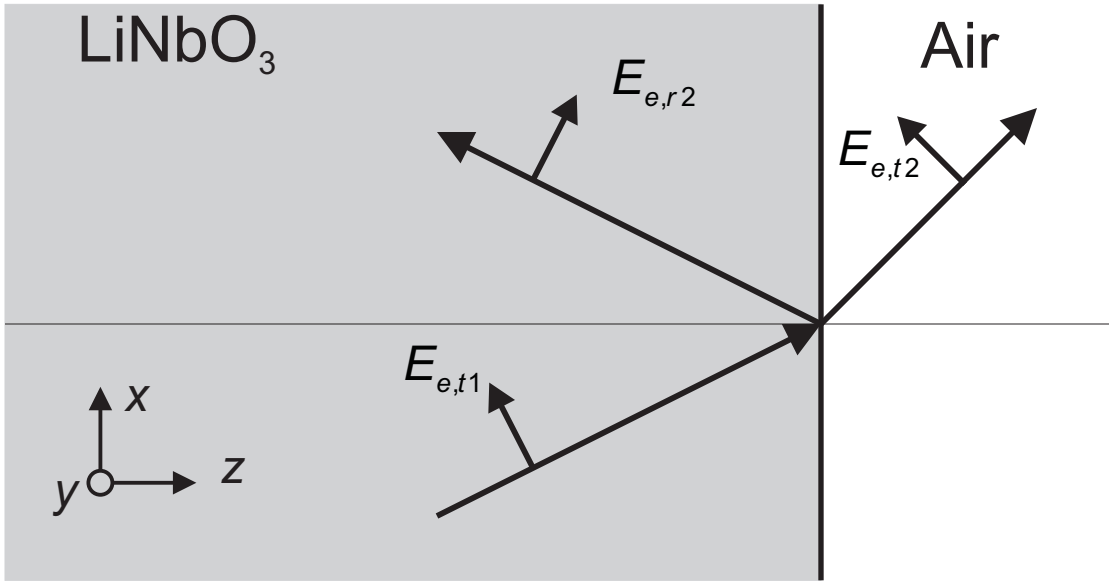

Figure 2.9 Second surface *e*-polarized second-harmonic fields.

and

$$E_{e,t2,x} = E^{o}_{e,t2,x} e^{i(K_{xs}x + K_{zs}(z-L) - \omega_s t)}, \tag{57a}$$

$$E_{e,t2,z} = E^{o}_{e,t2,z} e^{i(K_{xs}x + K_{zs}(z-L) - \omega_s t)}. \tag{57b}$$

The continuity of the transverse phases at the second surface has already been accounted for by the use of the propagation constants K_{xes}, K_{xep}, and K_{xs}. As was done for the forward propagating fields, the amplitudes of the particular solution for the backward-travelling fields are

$$A_{e,r2,x} = \frac{4d_{15}^{(2)}\left(K_{xep}^2 - k_s^2 n_{e,s}^2\right)E^{o}_{p,r2,x}E^{o}_{p,r2,z}}{\left(k_s^2 n_{o,s}^2 n_{e,s}^2 - n_{o,s}^2 K_{xep}^2 - n_{e,s}^2 K_{zep}^2\right)} - \frac{2K_{xep}K_{zep}\left(d_{31}^{(2)}\left(E^{o}_{p,r2,x}\right)^2 + d_{33}^{(2)}\left(E^{o}_{p,r2,z}\right)^2\right)}{\left(k_s^2 n_{o,s}^2 n_{e,s}^2 - n_{o,s}^2 K_{xep}^2 - n_{e,s}^2 K_{zep}^2\right)}, \tag{58a}$$

$$A_{e,r2,z} = \frac{-4d_{15}^{(2)}K_{xep}K_{zep}E^{o}_{p,r2,x}E^{o}_{p,r2,z}}{\left(k_s^2 n_{o,s}^2 n_{e,s}^2 - n_{o,s}^2 K_{xep}^2 - n_{e,s}^2 K_{zep}^2\right)} + \frac{2\left(K_{zep}^2 - k_s^2 n_{o,s}^2\right)\left(d_{31}^{(2)}\left(E^{o}_{p,r2,x}\right)^2 + d_{33}^{(2)}\left(E^{o}_{p,r2,z}\right)^2\right)}{\left(k_s^2 n_{o,s}^2 n_{e,s}^2 - n_{o,s}^2 K_{xep}^2 - n_{e,s}^2 K_{zep}^2\right)}. \tag{58b}$$

Expressing these backward-travelling amplitudes in terms of the input pump field by substituting Equations (19), (29a), and (30b) into Equations (58a,b) results in

$$A_{e,r2,x} = \left\{ \frac{4d_{15}^{(2)}\left(K_{xep}^2 - k_s^2 n_{e,s}^2\right)\frac{n_{o,p}^2}{n_{e,p}^2}\tan\theta_{ep}}{\left(k_s^2 n_{o,s}^2 n_{e,s}^2 - n_{o,s}^2 K_{xep}^2 - n_{e,s}^2 K_{zep}^2\right)} \right.$$

$$\left. - \frac{2K_{xep}K_{zep}\left(d_{31}^{(2)} + d_{33}^{(2)}\frac{n_{o,p}^4}{n_{e,p}^4}\tan^2\theta_{ep}\right)}{\left(k_s^2 n_{o,s}^2 n_{e,s}^2 - n_{o,s}^2 K_{xep}^2 - n_{e,s}^2 K_{zep}^2\right)} \right\} \tag{59a}$$

$$\times t1_e^2 r2_e^2 \cos^2\theta_{ep}\left(E_{p,e}^o\right)^2 e^{iK_{zep}L},$$

$$A_{e,r2,z} = \left\{ \frac{-4d_{15}^{(2)}K_{xep}K_{zep}\frac{n_{o,p}^2}{n_{e,p}^2}\tan\theta_{ep}}{\left(k_s^2 n_{o,s}^2 n_{e,s}^2 - n_{o,s}^2 K_{xep}^2 - n_{e,s}^2 K_{zep}^2\right)} \right.$$

$$\left. + \frac{2\left(K_{zep}^2 - k_s^2 n_{o,s}^2\right)\left(d_{31}^{(2)} + d_{33}^{(2)}\frac{n_{o,p}^4}{n_{e,p}^4}\tan^2\theta_{ep}\right)}{\left(k_s^2 n_{o,s}^2 n_{e,s}^2 - n_{o,s}^2 K_{xep}^2 - n_{e,s}^2 K_{zep}^2\right)} \right\} \tag{59b}$$

$$\times t1_e^2 r2_e^2 \cos^2\theta_{ep}\left(E_{p,e}^o\right)^2 e^{iK_{zep}L}.$$

These field amplitudes can be greatly simplified by recognizing that their relationships with the forward-travelling amplitudes are

$$A_{e,r2,x} = -A_{e,t1,x} \cdot r2_e^2 \cdot e^{iK_{zep}L} \text{ and} \tag{60a}$$

$$A_{e,r2,z} = A_{e,t1,z} \cdot r2_e^2 \cdot e^{iK_{zep}L}. \tag{60b}$$

Applying the boundary conditions to the second surface of the sample provides a means to solve for the remaining field amplitudes. The boundary conditions at z = L are

$$\left(E_{e,t1,x} + E_{e,r2,x}\right)\Big|_{z=L} = E_{e,t2,x}\Big|_{z=L} \text{ and} \tag{61a}$$

$$\left(H_{e,t1,y} + H_{e,r2,y}\right)\Big|_{z=L} = H_{e,t2,y}\Big|_{z=L}. \tag{61b}$$

Substituting into Equations (61a,b) for the various fields and setting their amplitudes equal across the boundary leads to

$$E^{o}_{e,t1,x} e^{iK_{zes}L} + A_{e,t1,x} e^{iK_{zep}L} + E^{o}_{e,r2,x} + A_{e,r2,x} = E^{o}_{e,t2,x}, \tag{62a}$$

$$\begin{aligned}\left(K_{zes}E^{o}_{e,t1,x} - K_{xes}E^{o}_{e,t1,z}\right)e^{iK_{zes}L} + \left(K_{zep}A_{e,t1,x} - K_{xep}A_{e,t1,z}\right)e^{iK_{zep}L} \\ - K_{zes}E^{o}_{e,r2,x} - K_{xes}E^{o}_{e,r2,z} - K_{zep}A_{e,r2,x} - K_{xep}A_{e,r2,z} = \\ K_{zs}E^{o}_{e,t2,x} - K_{xs}E^{o}_{e,t2,z}.\end{aligned} \tag{62b}$$

Expressing $E^{o}_{r2,z}$ and $E^{o}_{t2,z}$ in terms of $E^{o}_{r2,x}$ and $E^{o}_{t2,x}$ results in

$$E^{o}_{e,r2,z} = \left(\frac{n_{o,s}}{n_{e,s}}\right)^2 \frac{K_{xes}}{K_{zes}} E^{o}_{e,r2,x}, \tag{63a}$$

$$E^{o}_{e,t2,z} = \frac{-K_{xs}}{K_{zs}} E^{o}_{e,t2,x}. \tag{63b}$$

Combining Equations (60a,b), (62a,b), and (63a,b) results in the expression

$$E^{o}_{e,t2,x} = B_{1,ee} e^{iK_{zes}L} + \left(B_{2,ee} + B_{3,ee}\right)e^{iK_{zep}L} \tag{64}$$

for the transmitted *x*-oriented second-harmonic field amplitude, where the factors

$$B_{1,ee} = \frac{2b_1}{b_1 + b_2} E^{o}_{e,t1,x}, \tag{65a}$$

$$B_{2,ee} = \frac{\left(K_{zep} + b_1\right)A_{e,t1,x} - K_{xep}A_{e,t1,z}}{b_1 + b_2}, \tag{65b}$$

$$B_{3,ee} = \frac{\left(K_{zep} - b_1\right)A_{e,t1,x} - K_{xep}A_{e,t1,z}}{b_1 + b_2} \cdot r2_e^2, \tag{65c}$$

have been employed. Using a similar procedure, the backward-travelling homogeneous field amplitude is found to be

$$E^o_{e,r2,x} = C_{1,ee}e^{iK_{zes}L} + \left(C_{2,ee} + C_{3,ee}\right)e^{iK_{zep}L}, \tag{66}$$

where

$$C_{1,ee} = \frac{b_1 - b_2}{b_1 + b_2} E^o_{t1,x}, \tag{67a}$$

$$C_{2,ee} = \frac{\left(-b_2 + K_{zep}\right)A_{e,t1,x} - K_{xep}A_{e,t1,z}}{b_1 + b_2}, \tag{67b}$$

$$C_{3,ee} = \frac{\left(b_2 + K_{zep}\right)A_{e,t1,x} - K_{xep}A_{e,t1,z}}{b_1 + b_2} \cdot r2_e^2. \tag{67c}$$

An interesting note about Equations (64) and (66) concerns the phase associated with the coefficients B_2, B_3 and C_2, C_3. The phase for all these coefficients is $K_{zep}L$, but this value comes about in two distinct ways. The phase of the coefficients B_2 and C_2 comes from the source polarization terms while the phase of the B_3 and C_3 terms comes from the pump wave propagation.

Now that these amplitudes have been described, the optical power leaving the sample from the second surface may be examined. The power leaving the sample is proportional to the square of the amplitude of the transmitted SHG field:

$$P_{e-SHG} \propto \left|E^o_{t2,x}\right|^2 + \left|E^o_{t2,z}\right|^2 = \left|E^o_{t2,x}\right|^2 \sec^2\theta_i. \tag{68}$$

The *e*-polarized, second-harmonic power leaving the sample is then

$$P_{e-SHG}^{e-pump} \propto \left[B_{1,ee}^2 + \left(B_{2,ee} + B_{3,ee}\right)^2 + 2B_{1,ee}\left(B_{2,ee} + B_{3,ee}\right)\cos\left(\left(K_{zes} - K_{zep}\right)L\right)\right] \cdot \sec^2\theta_i. \tag{69}$$

Figure 2.10 is a plot of P_{e-SHG}^{e-pump} as a function of pump angle of incidence.

Following a similar procedure, as has been outlined in the previous pages, the second-harmonic output for the remaining pump-SHG configurations are given below. The *o*-polarized SHG produced from *e*-polarized pumping is

$$P_{o-SHG}^{e-pump} \propto \left[B_{1,eo}^2 + \left(B_{2,eo} + B_{3,eo}\right)^2 + 2B_{1,eo}\left(B_{2,eo} + B_{3,eo}\right)\cos\left(\left(K_{zos} - K_{zep}\right)L\right)\right], \tag{70}$$

where

$$B_{1,eo} = \frac{2K_{zos}}{K_{zos} + K_{zs}} E_{e,t1,y}^{o}, \tag{71a}$$

$$B_{2,eo} = \frac{K_{zos} + K_{zep}}{K_{zos} + K_{zs}} A_{e,t1,y}, \tag{71b}$$

$$B_{3,eo} = \frac{K_{zos} - K_{zep}}{K_{zos} + K_{zs}} A_{e,t1,y} r2_e^2, \tag{71c}$$

$$E_{e,t1,y}^{o} = \frac{-\left(K_{zs} + K_{zep}\right)}{K_{zs} + K_{zos}} A_{e,t1,y}, \tag{71d}$$

$$A_{e,t1,y} = \frac{2d_{22}^{(2)}k_s^2}{\left(k_s^2 n_{o,s}^2 - K_{xep}^2 - K_{zep}^2\right)} \cdot t1_e^2 \cdot \cos^2\theta_{ep} \cdot \left(E_{p,e}^{o}\right)^2, \tag{71e}$$

$$K_{zos} = k_s n_{o,s} \cos\theta_{os} \tag{71f}$$

Figure 2.11 is a plot of P_{o-SHG}^{e-pump} as a function of pump angle of incidence.

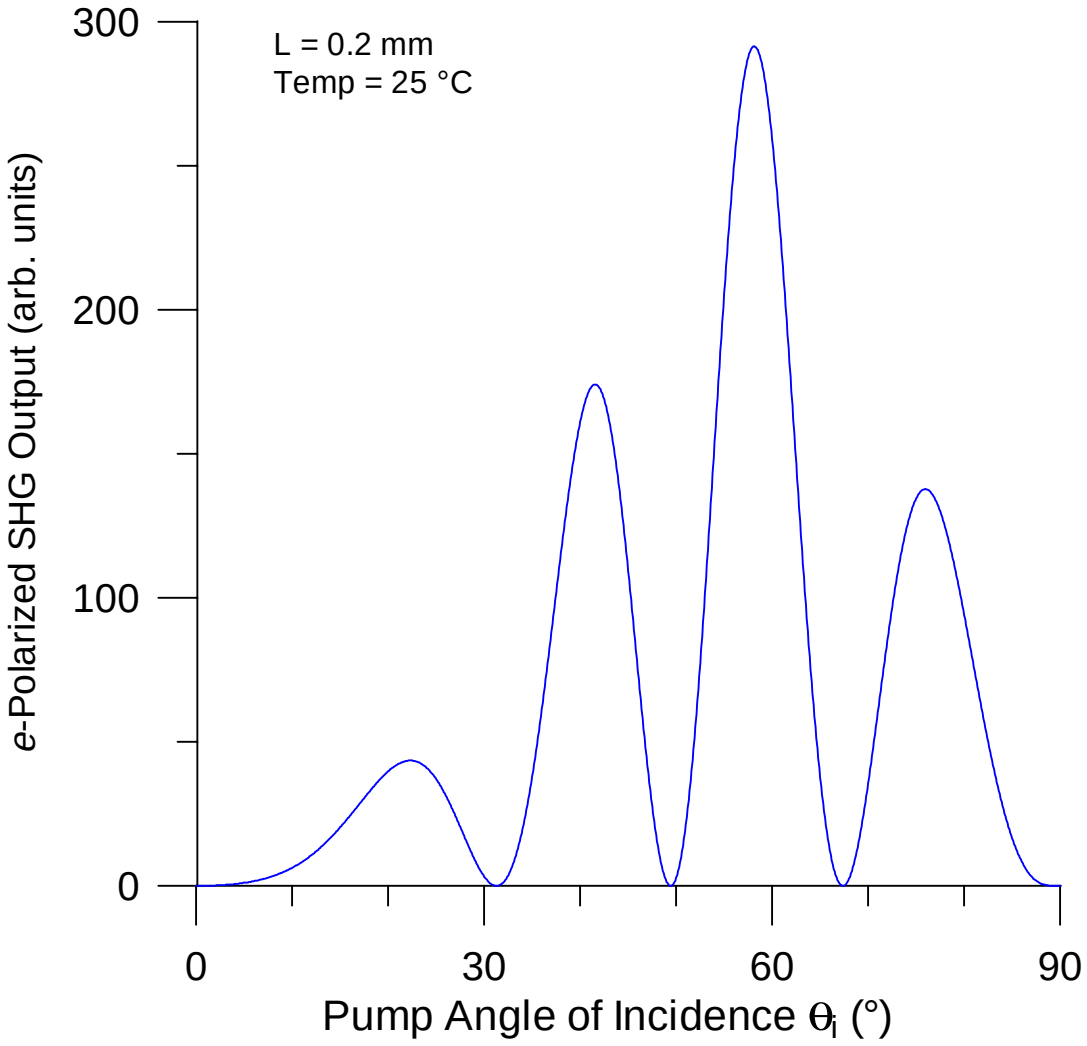

Figure 2.10 Single-pass *e*-polarized second-harmonic output resulting from an *e*-polarized pump.

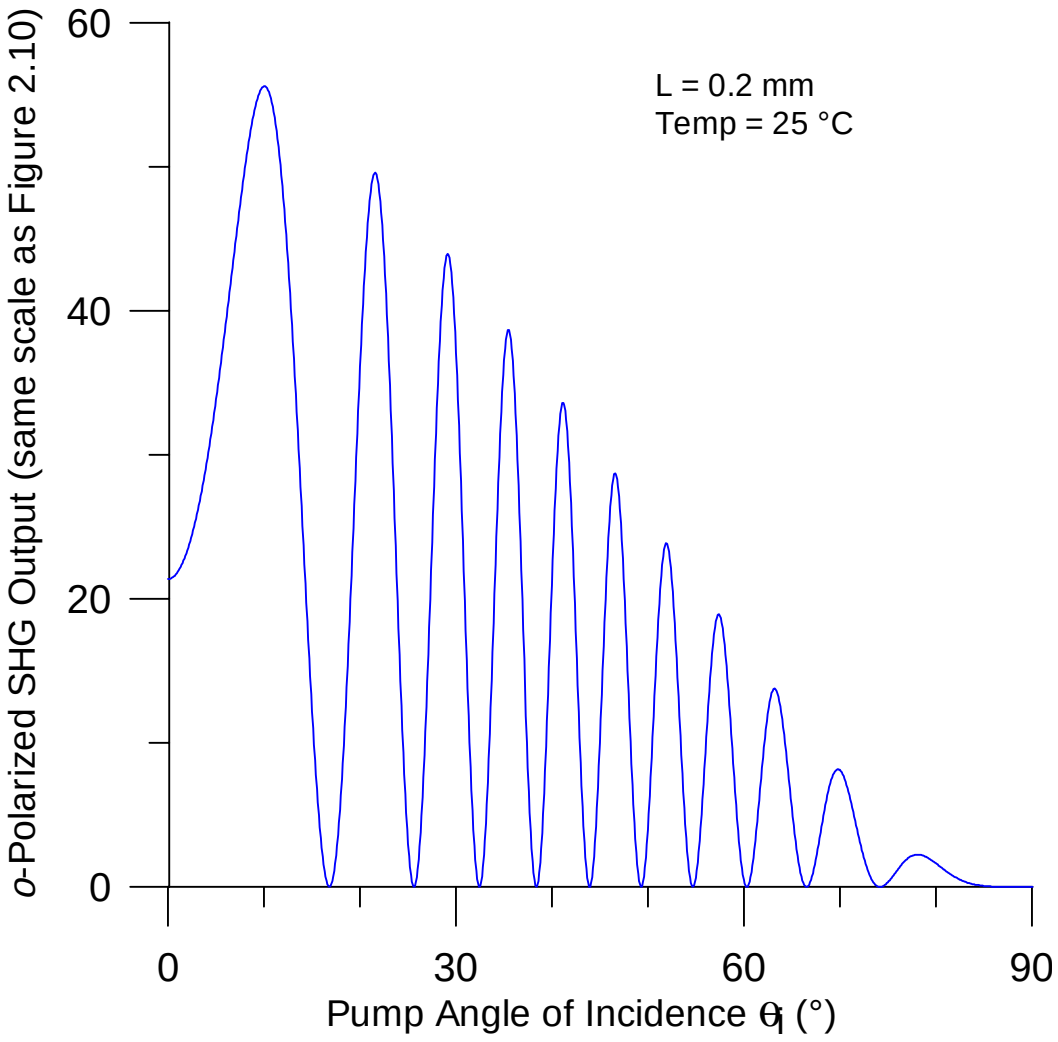

Figure 2.11 Single-pass *o*-polarized second-harmonic output resulting from an *e*-polarized pump.

The *o*-polarized SHG resulting from an *o*-polarized pump is

$$P_{o-SHG}^{o-pump} \propto \left[B_{1,oo}^2 + \left(B_{2,oo} + B_{3,oo}\right)^2 + 2B_{1,oo}\left(B_{2,oo} + B_{3,oo}\right)\cos\left(\left(K_{zos} - K_{zop}\right)L\right)\right], \tag{72}$$

where

$$B_{1,oo} = \frac{2K_{zos}}{K_{zos} + K_{zs}} E_{o,t1,y}^{o}, \tag{73a}$$

$$B_{2,oo} = \frac{K_{zos} + K_{zop}}{K_{zos} + K_{zs}} A_{o,t1,y}, \tag{73b}$$

$$B_{3,oo} = \frac{K_{zos} - K_{zop}}{K_{zos} + K_{zs}} A_{o,t1,y} r2_o^2, \tag{73c}$$

$$E_{o,t1,y}^{o} = \frac{-\left(K_{zs} + K_{zop}\right)}{K_{zs} + K_{zos}} A_{o,t1,y}, \tag{73d}$$

$$A_{o,t1,y} = \frac{2d_{22}^{(2)} k_s^2}{\left(k_s^2 n_{o,s}^2 - K_{xop}^2 - K_{zop}^2\right)} \cdot t1_o^2 \cdot \left(E_{p,o}^{o}\right)^2, \tag{73e}$$

$$K_{zos} = k_s n_{o,s} \cos\theta_{os}. \tag{73f}$$

Figure 2.12 is a plot of P_{o-SHG}^{o-pump} as a function of pump angle of incidence. The *e*-polarized SHG resulting from an *o*-polarized pump is

$$\begin{aligned} P_{e-SHG}^{o-pump} \propto \Big[& B_{1,oe}^2 + \left(B_{2,oe} + B_{3,oe}\right)^2 \\ & + 2B_{1,oe}\left(B_{2,oe} + B_{3,oe}\right)\cos\left(\left(K_{zes} - K_{zop}\right)L\right)\Big] \cdot \sec^2\theta_i, \end{aligned} \tag{74}$$

where

$$B_{1,oe} = \frac{2b_1}{b_1 + b_2} E_{o,t1,x}^{o}, \tag{75a}$$

$$B_{2,oe} = \frac{\left(K_{zop} + b_1\right)A_{o,t1,x} - K_{xop}A_{o,t1,z}}{b_1 + b_2}, \tag{75b}$$

$$B_{3,oe} = \frac{\left(K_{zop} - b_1\right)A_{o,t1,x} - K_{xop}A_{o,t1,z}}{b_1 + b_2} \cdot r2_o^2, \tag{75c}$$

$$E_{o,t1,x}^{o} = \frac{K_{xop}A_{o,t1,z} - \left(K_{zop} + b_2\right)A_{o,t1,x}}{b_1 + b_2}, \text{ and} \tag{75d}$$

$$A_{o,t1,x} = \frac{2d_{31}^{(2)}K_{xop}K_{zop}}{\left(k_s^2 n_{o,s}^2 n_{e,s}^2 - n_{o,s}^2 K_{xop}^2 - n_{e,s}^2 K_{zop}^2\right)} \cdot t1_o^2 \cdot \left(E_{p,o}^{o}\right)^2 \tag{75e}$$

$$A_{o,t1,z} = \frac{2d_{31}^{(2)}\left(K_{zop}^2 - k_s^2 n_{o,s}^2\right)}{\left(k_s^2 n_{o,s}^2 n_{e,s}^2 - n_{o,s}^2 K_{xop}^2 - n_{e,s}^2 K_{zop}^2\right)} \cdot t1_o^2 \cdot \left(E_{p,o}^{o}\right)^2 \tag{75f}$$

Figure 2.13 is a plot of P_{e-SHG}^{o-pump} as a function of pump angle of incidence.

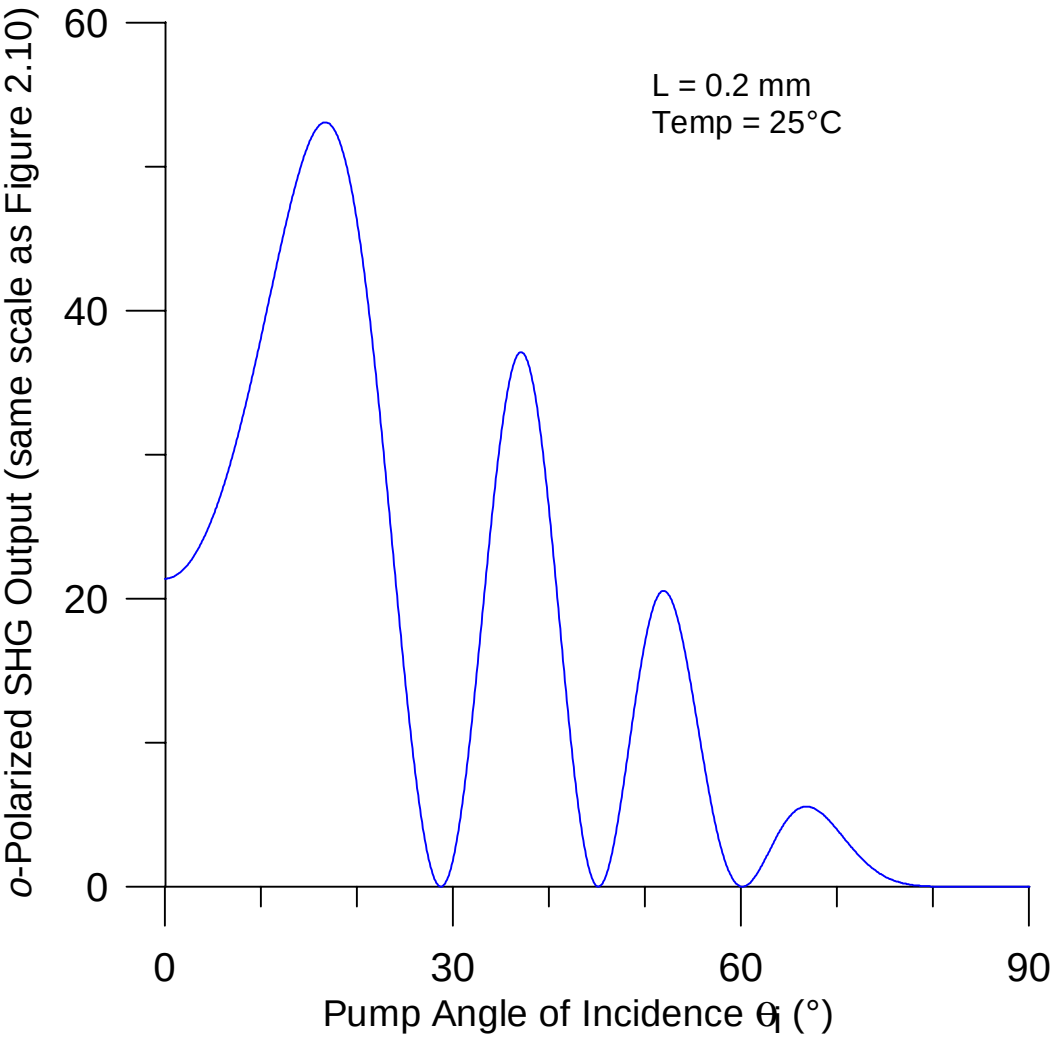

Figure 2.12 Single-pass *o*-polarized second-harmonic output resulting from an *o*-polarized pump.

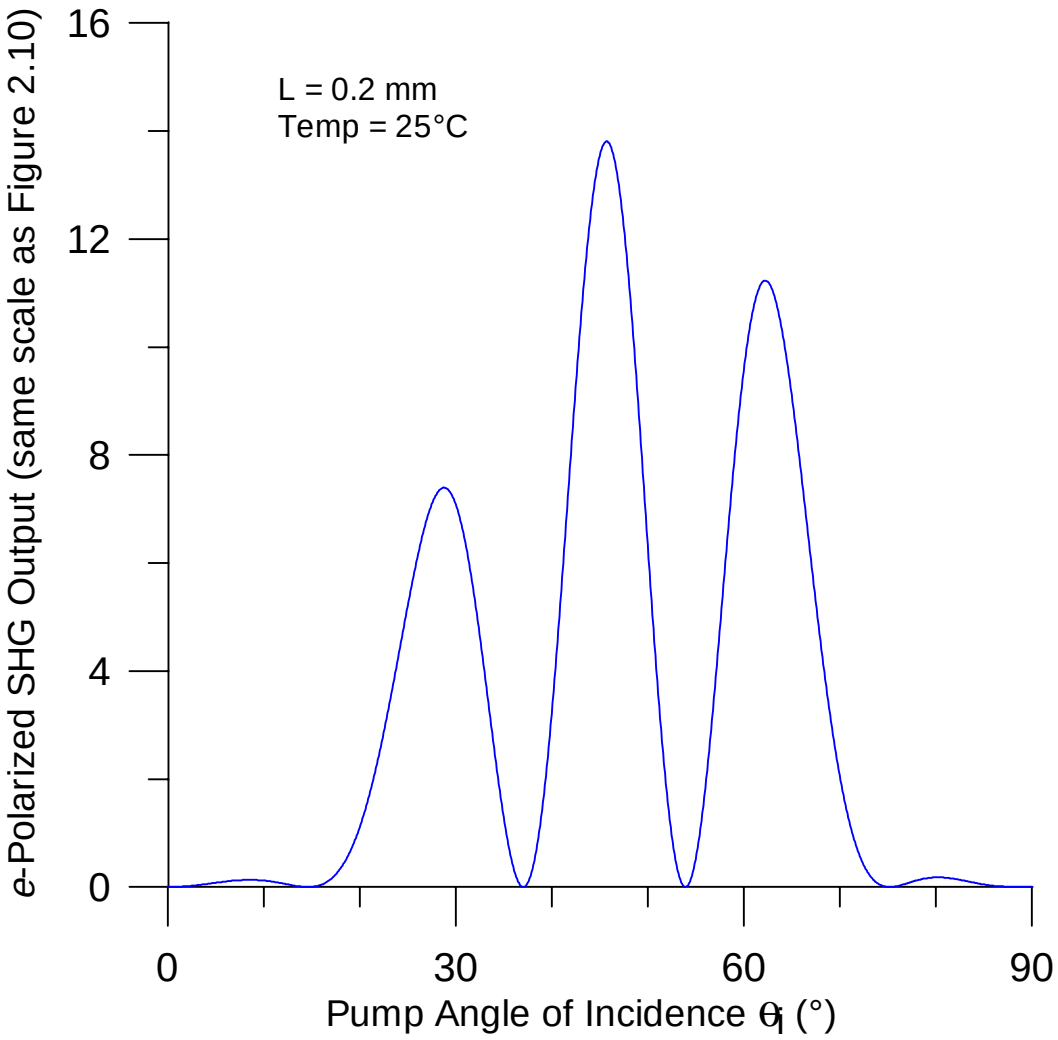

Figure 2.13 Single-pass *e*-polarized second-harmonic output resulting from an *o*-polarized pump.

2.3 Second-Pass Correction

Comparing the single-pass approximation to actual data shows that the single-pass approximation, while good, fails to reproduce the high frequency components in the data. Figure 2.14 shows *e*-polarized second-harmonic data for *e*-polarized pumping along with the single-pass *e*- to *e*-polarized theory. In this example the high frequency components of the data are visible but they are not very prominent. This is because the high frequency component of the second harmonic output is strongest at normal incidence, while the *e*-polarized second-harmonic signal approaches zero at normal incidence. Better examples of the high frequency signal will be shown later in this discussion.

A better approximation to the high frequency component of the Maker fringe signal is obtained by including a second pass in the development of the pump and second-harmonic generation.

2.3.1 Second-Pass Pump Field

Following the propagation of the pump field reflected from the rear surface of the substrate back to the front surface results in yet another set of boundary conditions. Figure 2.15 is a simple ray diagram illustrating the pump and second-harmonic fields that contribute to the second-pass

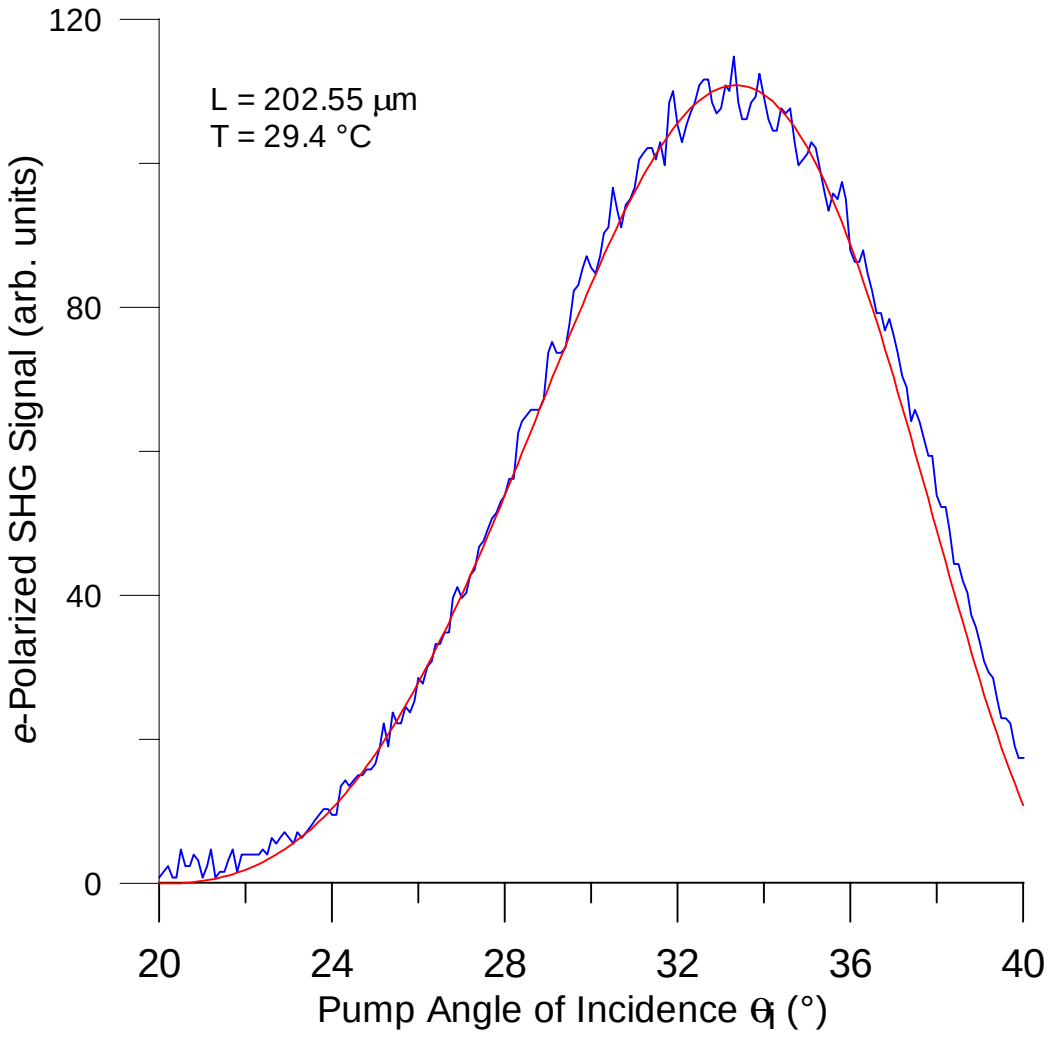

Figure 2.14 Comparison of single-pass *e*-*e* Maker-fringe theory (red) with data (blue).

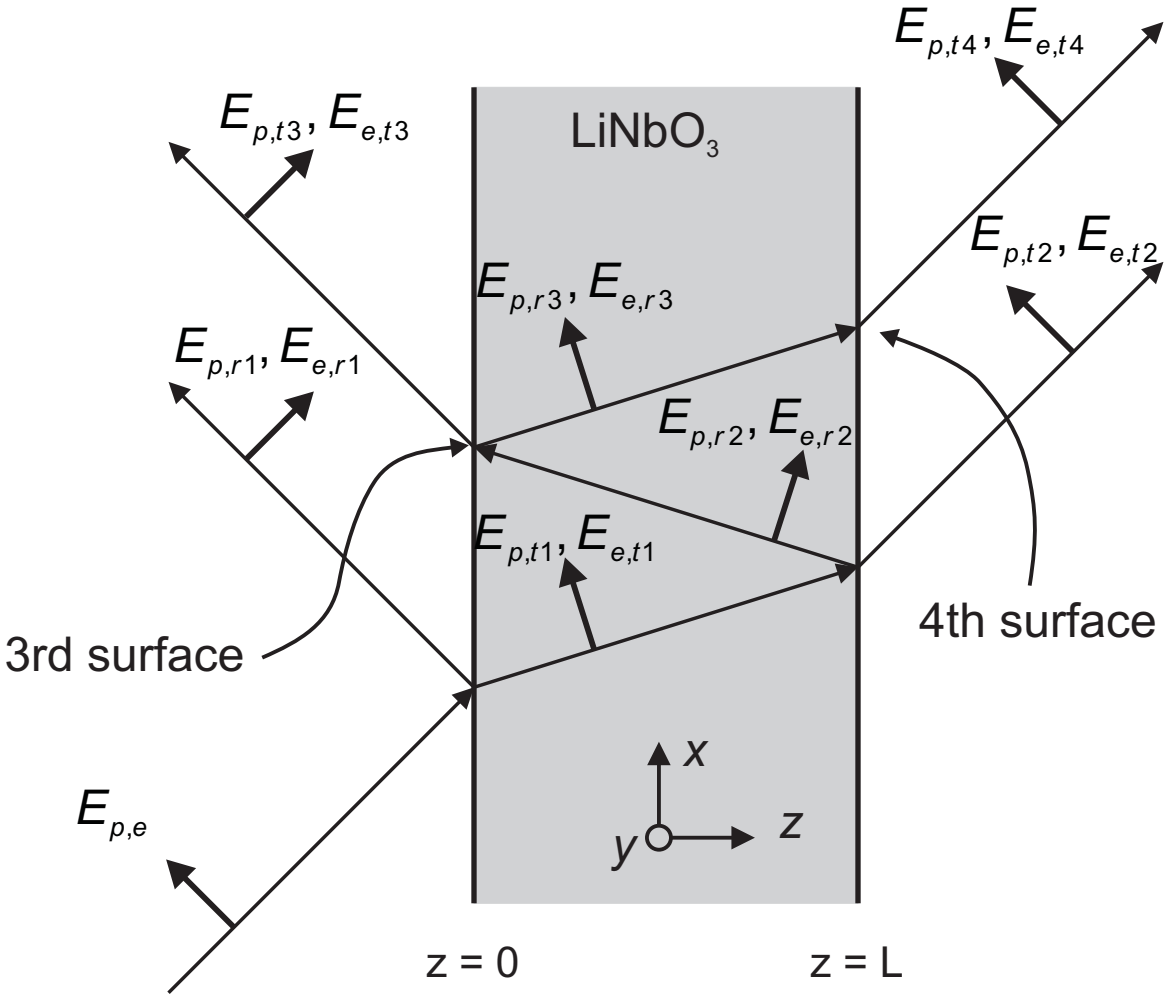

Figure 2.15 Schematic representation of *e*-polarized electric fields involved in the second-pass correction.

correction. The pump fields at this “third surface” may be written as

$$E_{p,r2,x} = E^{o}_{p,r2,x} e^{i(K_{pex}x - K_{pez}(z-L) - \omega_p t)}, \tag{76a}$$

$$E_{p,r2,z} = E^{o}_{p,r2,z} e^{i(K_{pex}x - K_{pez}(z-L) - \omega_p t)}, \tag{76b}$$

$$E_{p,r3,x} = E^{o}_{p,r3,x} e^{i(K_{pex}x + K_{pez}z - \omega_p t)}, \tag{76c}$$

$$E_{p,r3,z} = E^{o}_{p,r3,z} e^{i(K_{pex}x + K_{pez}z - \omega_p t)}, \tag{76d}$$

$$E_{p,t3,x} = E^{o}_{p,t3,x} e^{i(K_{xp}x - K_{zp}z - \omega_p t)}, \tag{76e}$$

$$E_{p,t3,z} = E^{o}_{p,t3,z} e^{i(K_{xp}x - K_{zp}z - \omega_p t)}. \tag{76f}$$

The boundary conditions for this surface are

$$E_{p,t3,x}\Big|_{z=0} = \left(E_{p,r2,x} + E_{p,r3,x}\right)\Big|_{z=0}, \tag{77a}$$

$$H_{p,t3,y}\Big|_{z=0} = \left(H_{p,r2,y} + H_{p,r3,y}\right)\Big|_{z=0}. \tag{77b}$$

Solving for $E^{o}_{p,r3,x}$ following the procedures of the previous sections results in

$$E^{o}_{p,r3,x} = t1_e \cdot r2_e^2 \cdot \cos\theta_{ep} \cdot E^{o}_{p,e} e^{i2K_{pez}L}. \tag{78}$$

Continuing to propagate the pump ($E^{o}_{p,r3,x}$) to the rear surface of the substrate leads to the final boundary condition considered for the pump. The fields at this fourth boundary are

$$E_{p,r3,x} = E^{o}_{p,r3,x} e^{i(K_{pex}x + K_{pez}z - \omega_p t)}, \tag{79a}$$

$$E_{p,r3,z} = E^{o}_{p,r3,z} e^{i(K_{pex}x + K_{pez}z - \omega_p t)}, \tag{79b}$$

$$E_{p,r4,x} = E^{o}_{p,r4,x} e^{i(K_{pex}x - K_{pez}(z-L) - \omega_p t)}, \tag{79c}$$

$$E_{p,r4,z} = E^{o}_{p,r4,z} e^{i(K_{pex}x - K_{pez}(z-L) - \omega_p t)}, \tag{79d}$$

$$E_{p,t4,x} = E^{o}_{p,t4,x} e^{i(K_{xp}x + K_{zp}(z-L) - \omega_p t)}, \tag{79e}$$

$$E_{p,t4,z} = E^{o}_{p,t4,z} e^{i(K_{xp}x + K_{zp}(z-L) - \omega_p t)}, \tag{79f}$$

while the boundary conditions are

$$\left(E_{p,r3,x} + E_{p,r4,x}\right)\Big|_{z=L} = E_{p,t4,x}\Big|_{z=L}, \tag{80a}$$

$$\left(H_{p,r3,y} + H_{p,r4,y}\right)\Big|_{z=L} = H_{p,t4,y}\Big|_{z=L}. \tag{80b}$$

Solving this set of boundary conditions for $E^{o}_{p,r4,x}$ results in

$$E^{o}_{p,r4,x} = t1_e \cdot r2_e^3 \cdot \cos\theta_{ep} \cdot E^{o}_{p,e} e^{j3K_{pez}L}. \tag{81}$$

This concludes the discussion of the pump field. The results from Equations (78) and (81) will be used later to reduce the second harmonic driving terms into functions of the input pump amplitude.

2.3.2 Second-Pass Second-Harmonic Generation

The second pass of the second-harmonic fields must are now derived. Once again, Figure 2.15 illustrates the progression of the second-harmonic field through the sample that makes up the second-pass correction. The second-harmonic fields and boundary conditions at the third surface are

$$E_{e,r2,x} = E^{o}_{e,r2,x} e^{i(K_{xes}x - K_{zes}(z-L) - \omega_s t)} + A_{e,r2,x} e^{i(K_{xep}x - K_{zep}(z-L) - \omega_s t)}, \tag{82a}$$

$$E_{e,r2,z} = E^{o}_{e,r2,z} e^{i(K_{xes}x - K_{zes}(z-L) - \omega_s t)} + A_{e,r2,z} e^{i(K_{xep}x - K_{zep}(z-L) - \omega_s t)}, \tag{82b}$$

$$E_{e,r3,x} = E^{o}_{e,r3,x} e^{i(K_{xes}x + K_{zes}z - \omega_s t)} + A_{e,r3,x} e^{i(K_{xep}x + K_{zep}z - \omega_s t)}, \tag{82c}$$

$$E_{e,r3,z} = E^{o}_{e,r3,z} e^{i(K_{xes}x + K_{zes}z - \omega_s t)} + A_{e,r3,z} e^{i(K_{xep}x + K_{zep}z - \omega_s t)}, \tag{82d}$$

$$E_{e,t3,x} = E^{o}_{e,t3,x} e^{i(K_{xs}x - K_{zs}z - \omega_s t)}, \tag{82e}$$

$$E_{e,t3,z} = E^{o}_{e,t3,z} e^{i(K_{xs}x - K_{zs}z - \omega_s t)}, \tag{82f}$$

and

$$E_{e,t3,x}\Big|_{z=0} = \left(E_{e,r2,x} + E_{e,r3,x}\right)\Big|_{z=0}, \tag{83a}$$

$$H_{e,t3,y}\Big|_{z=0} = \left(H_{e,r2,y} + H_{e,r3,y}\right)\Big|_{z=0}. \tag{83b}$$

Solving for $E^{o}_{e,r3,x}$ results in

$$E^{o}_{e,r3,x} = G^{(3)}_{1,ee} e^{iK_{zes}L} + G^{(3)}_{2,ee} e^{iK_{zep}L} + G^{(3)}_{3,ee}, \tag{84}$$

where

$$G^{(3)}_{1,ee} = \frac{b_1 - b_2}{b_1 + b_2} E^{o}_{e,r2,x}, \tag{85a}$$

$$G^{(3)}_{2,ee} = \frac{\left(K_{zep} - b_2\right)A_{e,r2,x} + K_{xep}A_{e,r2,z}}{b_1 + b_2}, \tag{85b}$$

$$G^{(3)}_{3,ee} = \frac{-\left(K_{zep} + b_2\right)A_{e,r3,x} + K_{xep}A_{e,r3,z}}{b_1 + b_2}, \tag{85c}$$

$$A_{e,r2,x} = -r2^2_e A_{e,t1,x} e^{iK_{zep}L}, \tag{85d}$$

$$A_{e,r2,z} = r2^2_e A_{e,t1,z} e^{iK_{zep}L}, \tag{85e}$$

$$A_{e,r3,x} = r2^4_e A_{e,t1,x} e^{i2K_{zep}L}, \tag{85f}$$

$$A_{e,r3,z} = r2^4_e A_{e,t1,z} e^{i2K_{zep}L}, \tag{85g}$$

and where Equation (78) has been used to express the third-pass driving terms $A_{e,r3}$ as functions of the first-pass driving terms $A_{e,r1}$. Rewriting Equation (84) in terms of the first-pass driving terms leads to

$$E^{o}_{e,r3,x} = C^{(3)}_{1,ee} E^{o}_{e,r2,x} e^{iK_{zes}L} + \left(C^{(3)}_{2,ee} + C^{(3)}_{3,ee}\right) e^{i2K_{zep}L}, \tag{86}$$

where

$$C^{(3)}_{1,ee} = \frac{b_1 - b_2}{b_1 + b_2}, \tag{87a}$$

$$C^{(3)}_{2,ee} = \frac{-\left(K_{zep} - b_2\right)A_{e,t1,x} + K_{xep}A_{e,t1,z}}{b_1 + b_2} r2^2_e, \tag{87b}$$

$$C^{(3)}_{3,ee} = \frac{-\left(K_{zep} + b_2\right)A_{e,t1,x} + K_{xep}A_{e,t1,z}}{b_1 + b_2} r2^4_e. \tag{87c}$$

Finally, propagating $E^{o}_{e,r3,x}$ to the rear surface of the substrate results in the following fields and boundary conditions:

$$E_{e,r3,x} = E^{o}_{e,r3,x} e^{i(K_{xes}x + K_{zes}z - \omega_s t)} + A_{e,r3,x} e^{i(K_{xep}x + K_{zep}z - \omega_s t)}, \tag{88a}$$

$$E_{e,r3,z} = E^{o}_{e,r3,z} e^{i(K_{xes}x + K_{zes}z - \omega_s t)} + A_{e,r3,z} e^{i(K_{xep}x + K_{zep}z - \omega_s t)}, \tag{88b}$$

$$E_{e,r4,x} = E^{o}_{e,r4,x} e^{i(K_{xes}x - K_{zes}(z-L) - \omega_s t)} + A_{e,r4,x} e^{i(K_{xep}x - K_{zep}(z-L) - \omega_s t)}, \tag{88c}$$

$$E_{e,r4,z} = E^{o}_{e,r4,z} e^{i(K_{xes}x - K_{zes}(z-L) - \omega_s t)} + A_{e,r4,z} e^{i(K_{xep}x - K_{zep}(z-L) - \omega_s t)}, \tag{88d}$$

$$E_{e,t4,x} = E^{o}_{e,t4,x} e^{i(K_{xs}x + K_{zs}(z-L) - \omega_s t)}, \tag{88e}$$

$$E_{e,t4,z} = E^{o}_{e,t4,z} e^{i(K_{xs}x + K_{zs}(z-L) - \omega_s t)}, \tag{88f}$$

and

$$\left(E_{e,r3,x} + E_{e,r4,x}\right)\Big|_{z=L} = E_{e,t4,x}\Big|_{z=L}, \tag{89a}$$

$$\left(H_{e,r3,y}+H_{e,r4,y}\right)\Big|_{z=L}=H_{e,t4,y}\Big|_{z=L}. \tag{89b}$$

Solving these boundary conditions with the fields in Equations (88a-f) results in the second-pass SHG field

$$E^{o}_{e,t4,x}=F^{(4)}_{1,ee}e^{iK_{zes}L}+F^{(4)}_{2,ee}e^{iK_{zep}L}+F^{(4)}_{3,ee}, \tag{90}$$

where

$$F^{(4)}_{1,ee}=\frac{2b_1}{b_1+b_2}E^{o}_{e,r3,x}, \tag{91a}$$

$$F^{(4)}_{2,ee}=\frac{\left(K_{zep}+b_1\right)A_{e,r3,x}-K_{xep}A_{e,r3,z}}{b_1+b_2}, \tag{91b}$$

$$F^{(4)}_{3,ee}=\frac{-\left(K_{zep}-b_1\right)A_{e,r4,x}-K_{xep}A_{e,r4,z}}{b_1+b_2}, \tag{91c}$$

$$A_{e,r4,x}=-r2^{6}_{e}A_{e,t1,x}e^{i3K_{zep}L}, \tag{91d}$$

$$A_{e,r4,z}=r2^{6}_{e}A_{e,t1,z}e^{i3K_{zep}L}. \tag{91e}$$

Rewriting Equation (90) in terms of the first-pass driving terms yields

$$E^{o}_{e,t4,x}=B^{(4)}_{1,ee}E^{o}_{e,r3,x}e^{iK_{zes}L}+\left(B^{(4)}_{2,ee}+B^{(4)}_{3,ee}\right)e^{i3K_{zep}L}, \tag{92}$$

where

$$B^{(4)}_{1,ee}=\frac{2b_1}{b_1+b_2}, \tag{93a}$$

$$B^{(4)}_{2,ee}=\frac{\left(K_{zep}+b_1\right)A_{e,t1,x}-K_{xep}A_{e,t1,z}}{b_1+b_2}r2^{4}_{e}, \tag{93b}$$

$$B_{3,ee}^{(4)} = \frac{(K_{zep} - b_1)A_{e,t1,x} - K_{xep}A_{e,t1,z}}{b_1 + b_2} r2_e^6. \tag{93c}$$

By substituting Equations (86) and (66) into Equation (92), the second-pass second-harmonic field becomes

$$\begin{aligned} E_{e,t4,x}^{o} = B_{1,ee}^{(4)} \Big\{ C_{1,ee}^{(3)} \big[C_{1,ee} e^{iK_{zes}L} + (C_{2,ee} + C_{3,ee}) e^{jK_{zep}L} \big] e^{iK_{zes}L} \\ + \big[C_{2,ee}^{(3)} + C_{3,ee}^{(3)} \big] e^{i2K_{zep}L} \Big\} e^{iK_{zes}L} + (B_{2,ee}^{(4)} + B_{3,ee}^{(4)}) e^{i2K_{zep}L}. \end{aligned} \tag{94}$$

By recognizing that several of these terms are quite small, Equation (94) can be simplified by retaining terms that contain factors up to $r2_e^2$ and ignoring terms containing higher powers of $r2_e$. Using these criteria eliminates $C_{3,ee}^{(3)}$, $B_{2,ee}^{(4)}$, and $B_{3,ee}^{(4)}$ from Equation (94) and results in the expression

$$E_{e,t4,x}^{o} = D_{1,ee} e^{i3K_{zes}L} + D_{2,ee} e^{i(2K_{zes} + K_{zep})L} + D_{3,ee} e^{i(K_{zes} + 2K_{zep})L}, \tag{95}$$

for the second-pass second-harmonic field leaving the sample, where

$$D_{1,ee} = B_{1,ee}^{(4)} C_{1,ee}^{(3)} C_{1,ee}, \tag{96a}$$

$$D_{2,ee} = B_{1,ee}^{(4)} C_{1,ee}^{(3)} (C_{2,ee} + C_{3,ee}), \tag{96b}$$

$$D_{3,ee} = B_{1,ee}^{(4)} C_{2,ee}^{(3)}. \tag{96c}$$

The second-harmonic power carried in the second-pass field is proportional to

$$\begin{aligned} P_{e-SHG,t4}^{e-pump} \propto \big\{ & D_{1,ee}^2 + D_{2,ee}^2 + D_{3,ee}^2 \\ & + 2D_{2,ee}(D_{1,ee} + D_{3,ee}) \cos\big[(K_{zes} - K_{zep})L\big] \\ & + 2D_{1,ee}D_{3,ee} \cos\big[(K_{zes} - K_{zep})2L\big] \big\} \cdot \sec^2 \theta_i. \end{aligned} \tag{97}$$

Equation (97) is plotted in Figure 2.16. Comparing the magnitude of the second-harmonic signal in Figures 2.10 and 2.16 shows that the perturbation to the single-pass second-harmonic output due to the second-pass correction

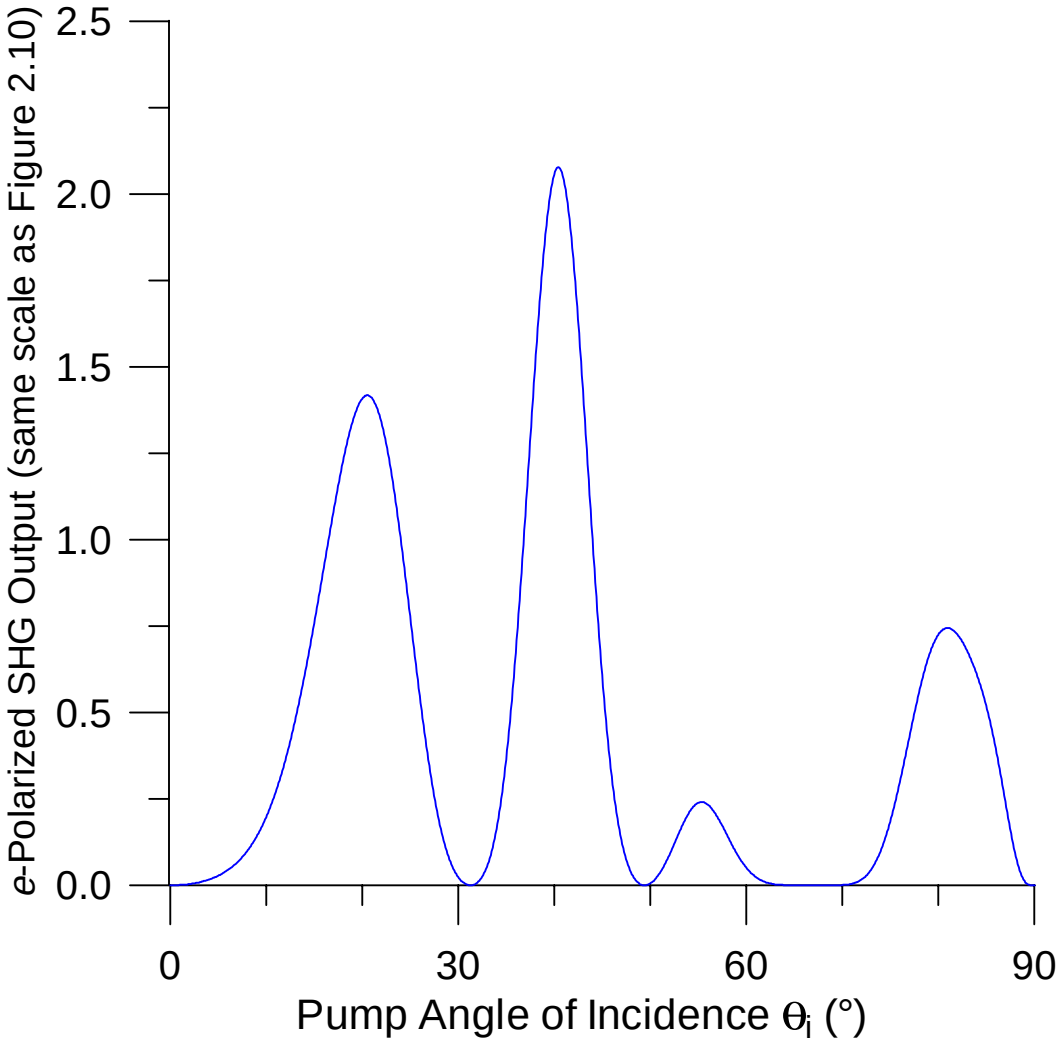

Figure 2.16 Second-pass contribution to theoretical *e*-polarized second-harmonic output P_{t4} for *e*-polarized pump.

is less than 1 %. However, as will be shown next, the coherent addition of the first- and second-pass second-harmonic signals adds a noticeable high frequency component to the total output signal. The total two-pass SHG power TPP_{e-SHG}^{e-pump} is proportional to

$$TPP_{e-SHG}^{e-pump} \propto P_{e-SHG}^{e-pump} + P_{e-SHG,t4}^{e-pump} + cross_{ee}, \tag{98}$$

where the cross terms between the first- and second-pass second-harmonic fields are incorporated into the term

$$\begin{aligned} cross_{ee} = \{ & 2B_{1,ee}D_{3,ee}\cos[2K_{zep}L] \\ & + 2(B_{1,ee}D_{2,ee} + B_{2,ee}D_{3,ee})\cos[(K_{zes} + K_{zep})L] \\ & + 2(B_{1,ee}D_{1,ee} + B_{2,ee}D_{2,ee})\cos[2K_{zes}L] \\ & + 2B_{2,ee}D_{1,ee}\cos[(3K_{zes} - K_{zep})L]\} \cdot \sec^2\theta_i. \end{aligned} \tag{99}$$

Figure 2.17 shows a plot of the full two-pass second-harmonic signal exiting the sample as described by Equation (98). For comparison, the single-pass SHG described by Equation (69) is also displayed.

While this solution is valid for infinite plane waves, it is far less accurate when considering beams of finite diameter. With finite beams there is the problem of walkoff between the first- and second-pass second-harmonic beams for increasing angles of incidence. This is illustrated in Figure 2.18. When these beams start to walk off, they go through a transition from overlapping spatially to being spatially separated. As this transition occurs, the addition of the beams goes from being coherent to being scalar. To simulate this walk off, a walkoff compensation factor η_s is defined that is

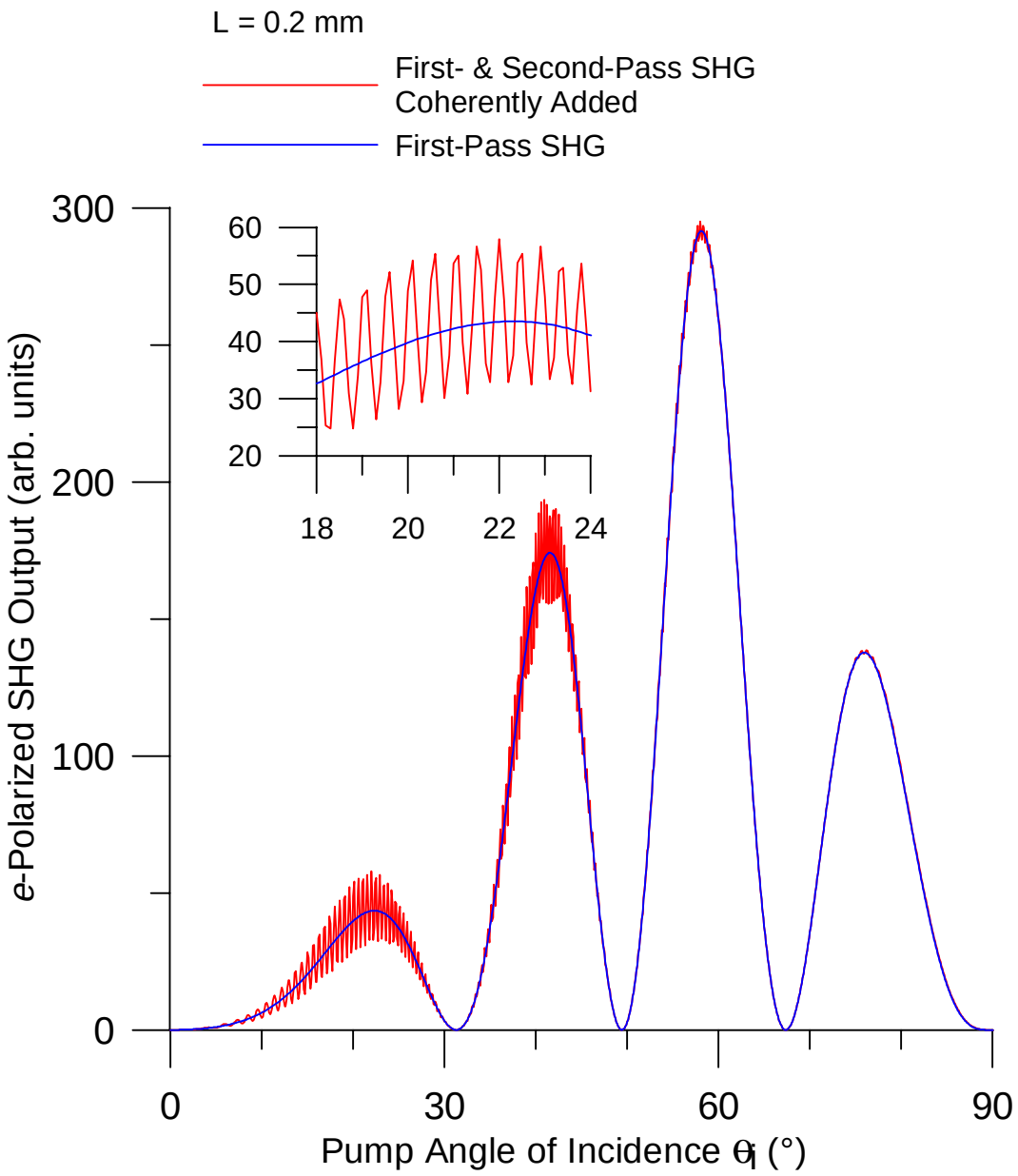

Figure 2.17 Coherent two-pass *e*-polarized second-harmonic output for *e*-polarized pump shown with single-pass solution. Inset shows blowup of high frequency fringes.

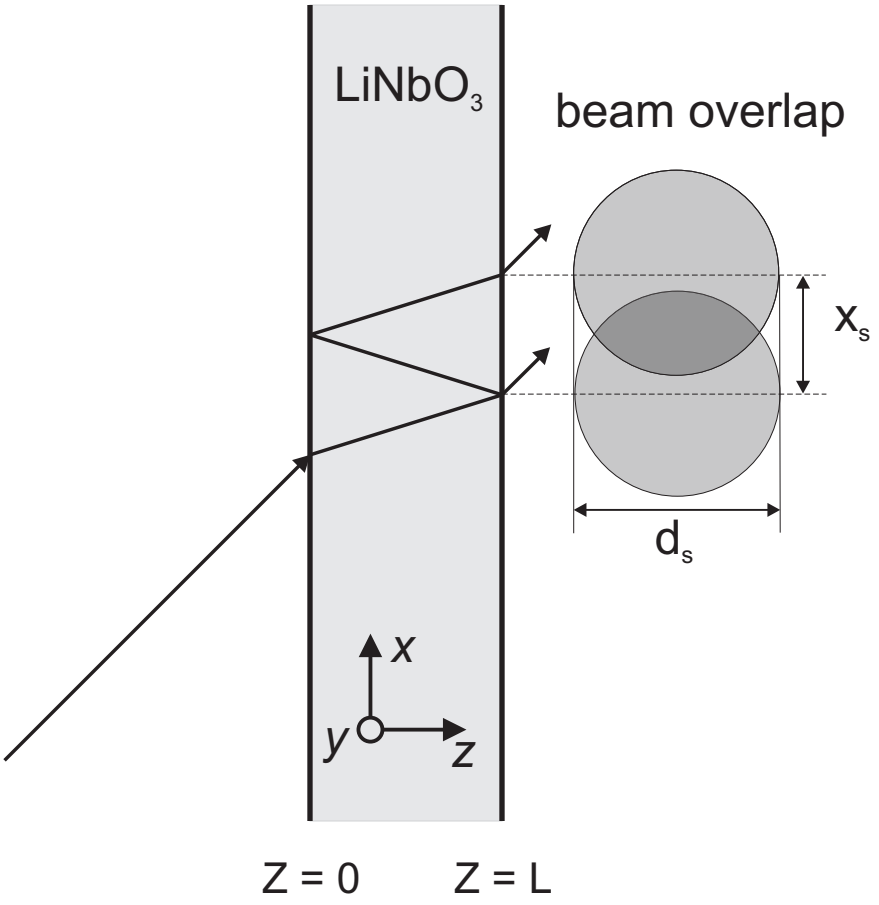

Figure 2.18 Schematic of beam walk off.

based on the physical dimensions of the Gaussian beam and the sample thickness:

$$\eta_s = \frac{2}{\pi d_s^2} \int_{-\infty}^{\infty} \int_{-\infty}^{\infty} \exp\left[\frac{-\left(x^2 + y^2\right)}{d_s^2}\right] \cdot \exp\left[\frac{-\left(\left(x - x_s\right)^2 + y^2\right)}{d_s^2}\right] dxdy \qquad (100)$$

where $x_{s,e} = 2L\tan\theta_{es}$, $d_s = d_p \big/ \sqrt{2}$, and d_s and d_p are the second-harmonic and pump beam diameters. Solving this double integral results in

$$\eta_{s,e} = \exp\left[\frac{-x_{s,e}^2}{2d_s^2}\right] \qquad (101)$$

Multiplying the cross term, $cross_{ee}$, of Equation (98) by η_s provides a heuristic means of simulating the beam walk off. Figure 2.19 illustrates the two-pass second-harmonic with the walkoff factor included along with the data first shown in Figure 2.14. A pump beam diameter of 70 μm and a sample thickness of 0.20255 mm have been used for this simulation. Figure 2.19, shows that the amplitude of the high frequency fringes matches that of the data fairly well. However, the frequency of this fringe component appears to be too large by a factor of 2.

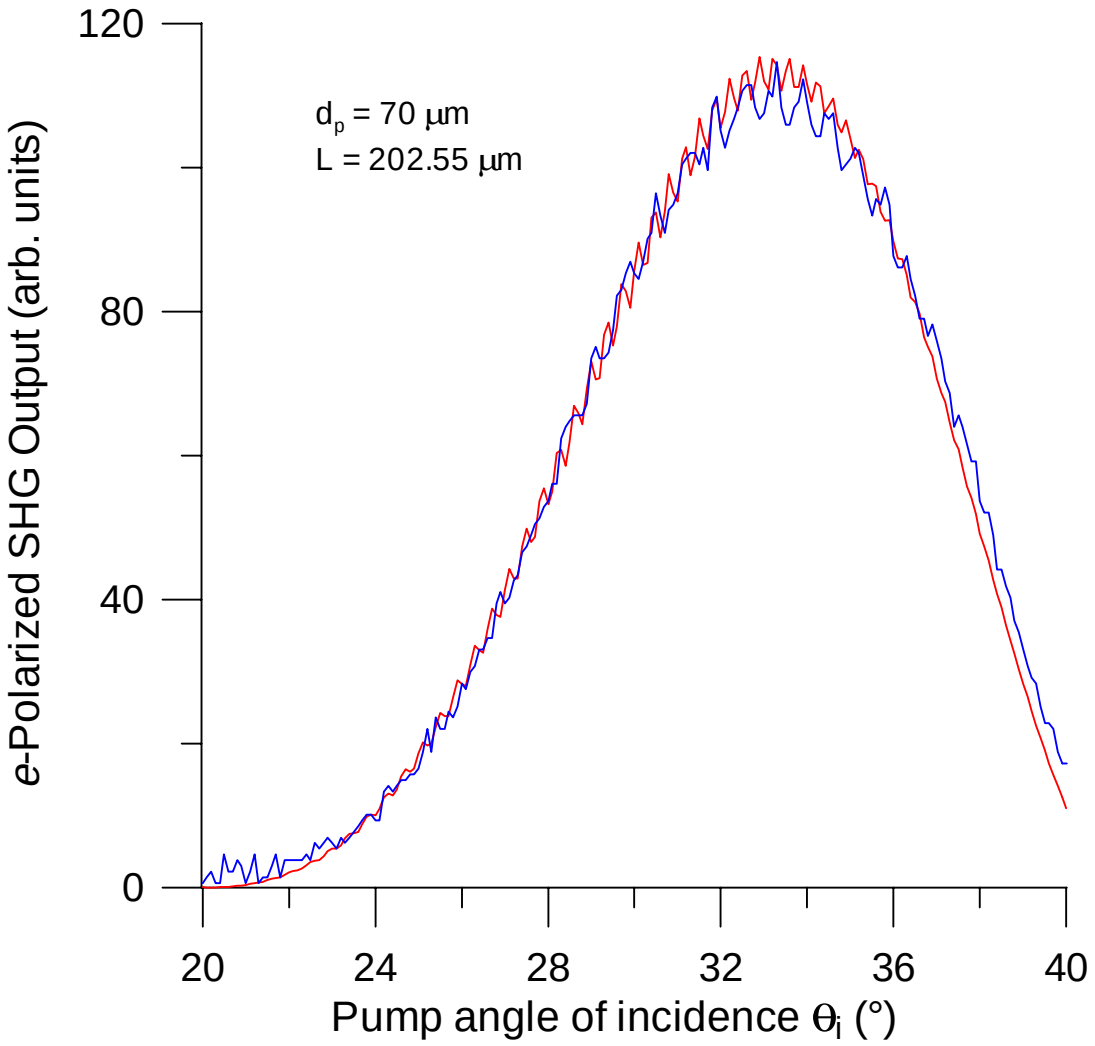

Figure 2.19 Comparison of two-pass *e*-polarized second-harmonic output with overlap factor for *e*-polarized pump (red) with data (blue).

2.4 Full Resonance Analysis

In the interest of developing a more rigorous solution to the Maker fringe signal, I now present a fully resonant approach. In this section the second-harmonic output is calculated by treating the sample under test as a Fabry-Perot resonator for both the pump and second-harmonic fields. The boundary conditions at the front and back of the sample are considered simultaneously. As depicted in Figure 2.20, the fields propagating through the system are composed of forward- and backward-travelling waves, each wave representing all the waves travelling in that particular direction at a particular location within the system. As an example, $E_{e,t1}$ represents all of the SHG waves travelling in the forward direction within the $LiNbO_3$.

2.4.1 Full Resonance Pump

The *e*-polarized pump wave incident on the sample may once again be written as

$$\vec{E}_{p,e} = \hat{x}E_{p,x} + \hat{z}E_{p,z} = E^o_{p,x}e^{i(K_{xp}x+K_{zp}z-\omega_p t)} + E^o_{p,z}e^{i(K_{xp}x+K_{zp}z-\omega_p t)}, \qquad (102)$$

with $K_{xp} = k_p \sin\theta_i$ and $K_{zp} = k_p \cos\theta_i$.

The reflected waves from the first surface may be represented as

$$E_{p,r1,x} = E^o_{p,r1,x}e^{i(K_{xp}x-K_{zp}z-\omega_p t)}, \qquad (103a)$$

$$E_{p,r1,z} = E^o_{p,r1,z}e^{i(K_{xp}x-K_{zp}z-\omega_p t)}. \qquad (103b)$$

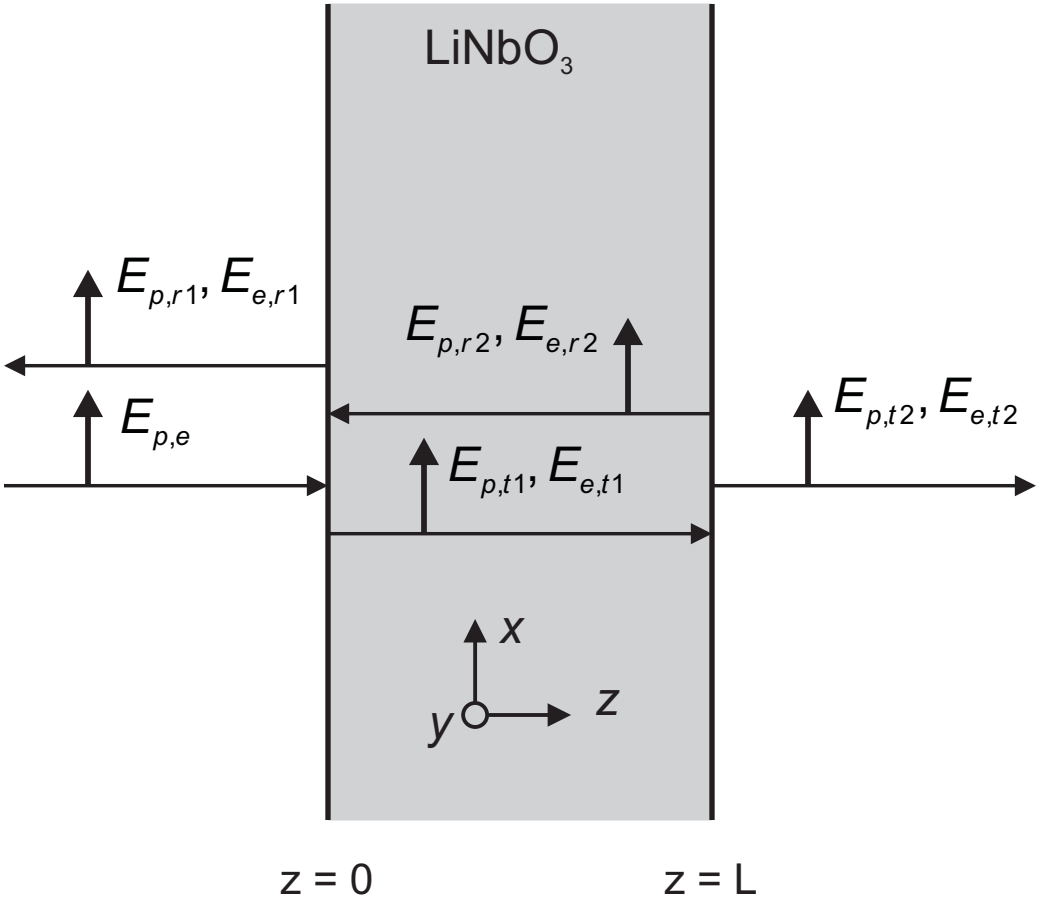

Figure 2.20 Schematic representation of the *e*-polarized forward and backward traveling electric fields associated the full resonance solution.

Equations (103a,b) use the knowledge that $\theta_i = \theta_r$. The wave equations developed earlier, Equations (7a-c), are still valid and describe the propagation of the waves through the sample. For the *e*-polarized pump, a solution to the homogeneous differential wave equations propagating in the forward direction is

$$E_{p,t1,x} = E^{o}_{p,t1,x} e^{i(K_{pex}x + K_{pez}z - \omega_p t)}, \tag{104a}$$

$$E_{p,t1,z} = E^{o}_{p,t1,z} e^{i(K_{pex}x + K_{pez}z - \omega_p t)}, \tag{104b}$$

with $K_{pex} = k_p n_{ep}(\theta_{ep})\sin\theta_{ep}$ and $K_{pez} = k_p n_{ep}(\theta_{ep})\cos\theta_{ep}$. The backward-propagating solution for the *e*-polarized pump field is represented by

$$E_{p,r2,x} = E^{o}_{p,r2,x} e^{i(K_{pex}x - K_{pez}(z-L) - \omega_p t)}, \tag{105a}$$

$$E_{p,r2,z} = E^{o}_{p,r2,z} e^{i(K_{pex}x - K_{pez}(z-L) - \omega_p t)}. \tag{105b}$$

The final pump field associated with this treatment is that transmitted through the entire system and is composed of

$$E_{p,t2,x} = E^{o}_{p,t2,x} e^{i(K_{xp}x + K_{zp}(z-L) - \omega_p t)}, \tag{106a}$$

$$E_{p,t2,z} = E^{o}_{p,t2,z} e^{i(K_{xp}x + K_{zp}(z-L) - \omega_p t)}. \tag{106b}$$

In order to solve for the field amplitudes in Equations (102), (103), (104), (105), and (106), the boundary conditions at the first and second surfaces of the lithium niobate substrate are invoked simultaneously. The boundary conditions are

$$\left(E_{p,x} + E_{p,r1,x}\right)\Big|_{z=0} = \left(E_{p,t1,x} + E_{p,r2,x}\right)\Big|_{z=0}, \tag{107a}$$

$$\left(H_{p,y} + H_{p,r1,y}\right)\Big|_{z=0} = \left(H_{p,t1,y} + H_{p,r2,y}\right)\Big|_{z=0}, \tag{107b}$$

for the first surface (z = 0) and

$$\left(E_{p,t1,x} + E_{p,r2,x}\right)\Big|_{z=L} = \left(E_{p,t2,x}\right)\Big|_{z=L} \tag{107c}$$

$$\left(H_{p,t1,y} + H_{p,r2,y}\right)\Big|_{z=L} = \left(H_{p,t2,y}\right)\Big|_{z=L}. \tag{107d}$$

for the second surface (z = L). Substituting the appropriate fields into Equations (107a-d) and equating the amplitudes from the left and right sides of these equations gives

$$-E^{o}_{p,r1,x} + E^{o}_{p,t1,x} + E^{o}_{p,r2,x}e^{iK_{pez}L} = E^{o}_{p,x}, \tag{108a}$$

$$bp_2 \cdot E^{o}_{p,r1,x} + bp_1 \cdot E^{o}_{p,r1,x} - bp_1 \cdot E^{o}_{p,r2,x}e^{iK_{pez}L} = bp_2 \cdot E^{o}_{p,x}, \tag{108b}$$

$$E^{o}_{p,t1,x}e^{iK_{pez}L} + E^{o}_{p,r2,x} - E^{o}_{p,t2,x} = 0, \tag{108c}$$

$$bp_1 \cdot E^{o}_{p,t1,x}e^{iK_{pez}L} - bp_1 \cdot E^{o}_{p,r2,x} - bp_2 E^{o}_{p,t2,x} = 0 \tag{108d}$$

where the factors

$$bp_1 = \left(\frac{n_{op}}{n_{ep}}\right)^2 \frac{K^2_{pex}}{K_{pez}} + K_{pez} \text{ and} \tag{109a}$$

$$bp_2 = \frac{K^2_{xp}}{K_{zp}} + K_{zp} \tag{109b}$$

are used to simplify the expressions. The field amplitudes may be found simultaneously using methods of linear algebra. Rewriting Equations (108a-d) in matrix format results in

$$\frac{1}{E^o_{p,x}}\begin{bmatrix} -1 & 1 & e^{iK_{pez}L} & 0 \\ bp_2 & bp_1 & -bp_1 e^{iK_{pez}L} & 0 \\ 0 & e^{iK_{pez}L} & 1 & -1 \\ 0 & bp_1 e^{iK_{pez}L} & -bp_1 & -bp_2 \end{bmatrix} \cdot \begin{bmatrix} E^o_{p,r1,x} \\ E^o_{p,t1,x} \\ E^o_{p,r2,x} \\ E^o_{p,t2,x} \end{bmatrix} = \begin{bmatrix} 1 \\ bp_2 \\ 0 \\ 0 \end{bmatrix}. \qquad (110)$$

The solutions to Equation (110) are

$$E^o_{p,r1,x} = \frac{-bp_1^2 + bp_2^2 + (bp_1^2 - bp_2^2)e^{i2K_{pez}L}}{(bp_1 + bp_2)^2 - (bp_1 - bp_2)^2 e^{i2K_{pez}L}} E^o_{p,x}, \qquad (111a)$$

$$E^o_{p,t1,x} = \frac{2bp_2(bp_1 + bp_2)}{(bp_1 + bp_2)^2 - (bp_1 - bp_2)^2 e^{i2K_{pez}L}} E^o_{p,x}, \qquad (111b)$$

$$E^o_{p,r2,x} = \frac{2bp_2(bp_1 - bp_2)e^{iK_{pez}L}}{(bp_1 + bp_2)^2 - (bp_1 - bp_2)^2 e^{i2K_{pez}L}} E^o_{p,x}, \qquad (111c)$$

$$E^o_{p,t2,x} = \frac{4bp_1 bp_2 e^{iK_{pez}L}}{(bp_1 + bp_2)^2 - (bp_1 - bp_2)^2 e^{i2K_{pez}L}} E^o_{p,x}. \qquad (111d)$$

Equations (111a-d) can be rewritten by substituting the expressions for bp_1 and bp_2, using $K_{zep} = 2K_{pez}$, and by putting $E^o_{p,x}$ in terms of $E^o_{p,e}$. The resulting expressions are

$$E^o_{p,r1,x} = r1_{e,FR} \cdot \cos\theta_i \cdot E^o_{p,e}, \qquad (112a)$$

$$E^o_{p,t1,x} = t1_{e,FR} \cdot \cos\theta_i \cdot E^o_{p,e}, \qquad (112b)$$

$$E^o_{p,r2,x} = t1_{e,FR} r2_{e,FR} \cdot \cos\theta_i \cdot E^o_{p,e} e^{iK_{pez}L}, \qquad (112c)$$

$$E^o_{p,t2,x} = t2_{e,FR} \cdot \cos\theta_i \cdot E^o_{p,e} e^{iK_{pez}L}, \qquad (112d)$$

where the resonant transmission and reflection coefficients in terms of the single-pass coefficients are

$$r1_{e,FR} = \frac{r1_e(1-e^{i2K_{pez}L})}{1-r1_e^2 e^{iK_{zep}L}}, \tag{113a}$$

$$t1_{e,FR} = \frac{t1_e}{1-r1_e^2 e^{iK_{zep}L}}, \tag{113b}$$

$$r2_{e,FR} = r2_e, \tag{113c}$$

$$t2_{e,FR} = \frac{t1_e t2_e}{1-r1_e^2 e^{iK_{zep}L}}. \tag{113d}$$

Examination of the quantities $r1_{e,FR}$ and $t2_{e,FR}$ reveals that these factors are the same as the Fabry-Perot coefficients found in optics texts such as [Hecht '87] with the added complexity that they describe uniaxial media as opposed to isotropic media. Comparing the first-surface transmission and reflection coefficients for the full resonance and single-pass developments shows that the full resonance coefficients follow the same trend as the single-pass coefficients, but that a high frequency modulation is superimposed. This comparison is illustrated in Figure 2.21. As was discussed during Section 2.3.2, due to walkoff of the multiple reflections within the sample, the resonance condition decreases as the pump incidence angle increases. To first approximation at high angles the reflectance and transmittance of the system are equal to the single-pass case. To simulate this condition a pump beam walk off factor η_p will be introduced later.

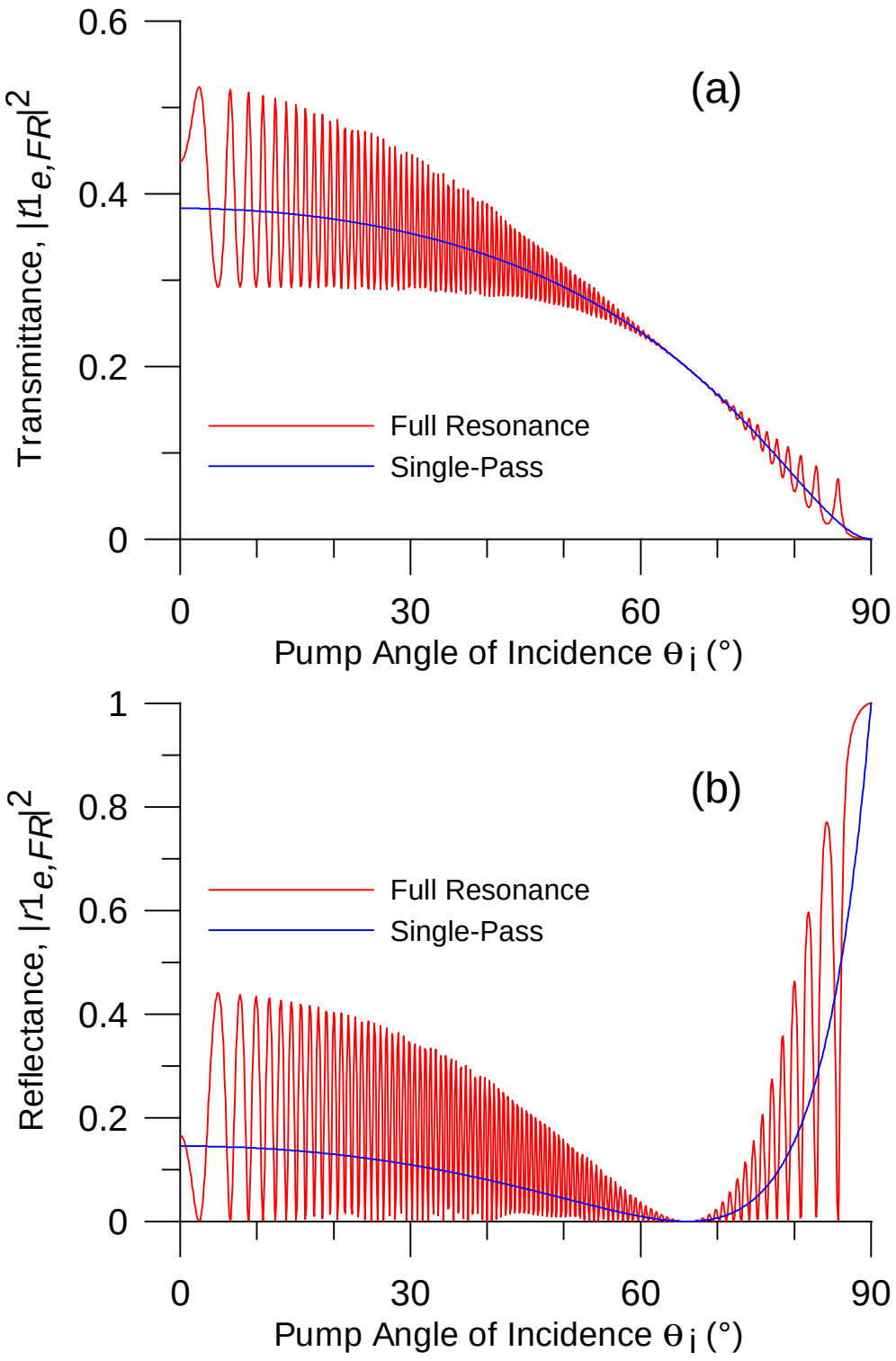

Figure 2.21 Comparison of the transittance (a) and reflectance (b) for the single-pass and full resonance developments.

2.4.2 Full Resonance Second-Harmonic Generation

With the pump fields accounted for, it is time to consider the SHG fields for the full resonance case. In addition to the pump fields, Figure 2.20 depicts the SHG fields for this treatment. These fields may be written as

$$E_{r1,x} = E^{o}_{r1,x} e^{i(K_{xp}x - K_{zp}z - \omega_s t)}, \tag{114a}$$

$$E_{r1,z} = E^{o}_{r1,z} e^{i(K_{xp}x - K_{zp}z - \omega_s t)}, \tag{114b}$$

$$E_{t1,x} = E^{o}_{t1,x} e^{i(K_{xes}x + K_{zes}z - \omega_s t)} + A^{FR}_{e,t1,x} e^{i(K_{xep}x + K_{zep}z - \omega_s t)}, \tag{114c}$$

$$E_{t1,z} = E^{o}_{t1,z} e^{i(K_{xes}x + K_{zes}z - \omega_s t)} + A^{FR}_{e,t1,z} e^{i(K_{xep}x + K_{zep}z - \omega_s t)}, \tag{114d}$$

$$E_{r2,x} = E^{o}_{r2,x} e^{i(K_{xes}x - K_{zes}(z-L) - \omega_s t)} + A^{FR}_{e,r2,x} e^{i(K_{xep}x - K_{zep}(z-L) - \omega_s t)}, \tag{114e}$$

$$E_{r2,z} = E^{o}_{r2,z} e^{i(K_{xes}x - K_{zes}(z-L) - \omega_s t)} + A^{FR}_{e,r2,z} e^{i(K_{xep}x - K_{zep}(z-L) - \omega_s t)}, \tag{114f}$$

$$E_{t2,x} = E^{o}_{t2,x} e^{i(K_{xp}x + K_{zp}(z-L) - \omega_s t)}, \tag{114g}$$

$$E_{t2,z} = E^{o}_{t2,z} e^{i(K_{xp}x + K_{zp}(z-L) - \omega_s t)}. \tag{114h}$$

The field amplitudes of the driving terms are derived just as they were in the single-pass case. It is no surprise that the results here are identical to that of the single-pass case except for the definition of the pump transmission coefficient. For the full resonance case the driving terms are

$$A_{e,t1,x}^{FR} = \left\{ \frac{-4d_{15}^{(2)}\left(K_{xep}^2 - k_s^2 n_{e,s}^2\right)\dfrac{n_{o,p}^2}{n_{e,p}^2}\tan\theta_{ep}}{k_s^2 n_{o,s}^2 n_{e,s}^2 - n_{o,s}^2 K_{xep}^2 - n_{e,s}^2 K_{zep}^2} \right.$$

$$\left. + \frac{2K_{xep}K_{zep}\left(d_{31}^{(2)} + d_{33}^{(2)}\dfrac{n_{o,p}^4}{n_{e,p}^4}\tan^2\theta_{ep}\right)}{k_s^2 n_{o,s}^2 n_{e,s}^2 - n_{o,s}^2 K_{xep}^2 - n_{e,s}^2 K_{zep}^2} \right\} t1_{e,FR}^2 \cos^2\theta_i \left(E_p^o\right)^2, \tag{115a}$$

$$A_{e,t1,z}^{FR} = \left\{ \frac{-4d_{15}^{(2)}K_{xep}K_{zep}\dfrac{n_{o,p}^2}{n_{e,p}^2}\tan\theta_{ep}}{k_s^2 n_{o,s}^2 n_{e,s}^2 - n_{o,s}^2 K_{xep}^2 - n_{e,s}^2 K_{zep}^2} \right.$$

$$\left. + \frac{2\left(K_{zep}^2 - k_s^2 n_{o,s}^2\right)\left(d_{31\,31}^{(2)} + d_{33}^{(2)}\dfrac{n_{o,p}^4}{n_{e,p}^4}\tan^2\theta_{ep}\right)}{k_s^2 n_{o,s}^2 n_{e,s}^2 - n_{o,s}^2 K_{xep}^2 - n_{e,s}^2 K_{zep}^2} \right\}$$

$$\times t1_{e,FR}^2 \cos^2\theta_i \left(E_p^o\right)^2, \tag{115b}$$

$$A_{e,r2,x}^{FR} = -A_{e,t1,x}^{FR} r2_{e,FR}^2 e^{iK_{zep}L}, \tag{115c}$$

$$A_{e,r2,z}^{FR} = A_{e,t1,z}^{FR} r2_{e,FR}^2 e^{iK_{zep}L}. \tag{115d}$$

The boundary conditions for the full resonance SHG fields are

$$\left(E_{r1,x}\right)\Big|_{z=0} = \left(E_{t1,x} + E_{r2,x}\right)\Big|_{z=0} \text{ and} \tag{116a}$$

$$\left(H_{r1,y}\right)\Big|_{z=0} = \left(H_{t1,y} + H_{r2,y}\right)\Big|_{z=0} \tag{116b}$$

for the first surface (z = 0) and

$$\left(E_{t1,x}+E_{r2,x}\right)\Big|_{z=L}=\left(E_{t2,x}\right)\Big|_{z=L} \text{ and} \tag{116c}$$

$$\left(H_{t1,y}+H_{r2,y}\right)\Big|_{z=L}=\left(H_{t2,y}\right)\Big|_{z=L} \tag{116d}$$

for the second surface (z = L). Setting the amplitudes of the left and right sides of Equations (116a-d) equal and writing them in matrix format yields

$$\begin{bmatrix} -1 & 1 & e^{iK_{zes}L} & 0 \\ b_2 & b_1 & -b_1 e^{iK_{zes}L} & 0 \\ 0 & e^{iK_{zes}L} & 1 & -1 \\ 0 & b_1 e^{iK_{pez}L} & -b_1 & -b_2 \end{bmatrix} \cdot \begin{bmatrix} E^o_{r1,x} \\ E^o_{t1,x} \\ E^o_{r2,x} \\ E^o_{t2,x} \end{bmatrix} = \begin{bmatrix} -(1-r2^2_{e,FR}e^{i2K_{zep}L})A^{FR}_{e,r2,x} \\ -(1+r2^2_{e,FR}e^{i2K_{zep}L})b_3 \\ -(1-r2^2_{e,FR})A^{FR}_{e,r2,x}e^{iK_{zep}L} \\ -(1+r2^2_{e,FR})b_3 e^{iK_{zep}L} \end{bmatrix}, \tag{117}$$

where the expressions

$$b_1=\left(\frac{n_{os}}{n_{es}}\right)^2\frac{K^2_{xes}}{K_{zes}}+K_{zes}, \tag{118a}$$

$$b_2=\frac{K^2_{xs}}{K_{zs}}+K_{zs}, \tag{118b}$$

$$b_{3,e}=-K_{xep}A^{FR}_{e,t1,z}+K_{zep}A^{FR}_{e,t1,x} \tag{118c}$$

are used to simplify the notation. Solving for the transmitted *e*-polarized SHG field results in

$$\begin{aligned} E^o_{t2,e}=&B_{1,ee,FR}e^{iK_{zep}L}+B_{2,ee,FR}e^{iK_{zes}L} \\ &+B_{3,ee,FR}e^{i(2K_{zep}+K_{zes})L}+B_{4,ee,FR}e^{i(K_{zep}+2K_{zes})L}, \end{aligned} \tag{119}$$

where

$$B_{1,ee,FR}=\frac{(b_1+b_2)(b_3(1+r2^2_{e,FR})+b_1(1-r2^2_{e,FR})A^{FR}_{e,t1,x})}{(b_1+b_2)^2-(b_1-b_2)^2e^{i2K_{zes}L}}, \tag{120a}$$

$$B_{2,ee,FR}=\frac{-2b_1(b_3+b_2A^{FR}_{e,t1,x})}{(b_1+b_2)^2-(b_1-b_2)^2e^{i2K_{zes}L}}, \tag{120b}$$

$$B_{3,ee,FR} = \frac{-2b_1 r2_{e,FR}^2 (b_3 - b_2 A_{e,t1,x}^{FR})}{(b_1 + b_2)^2 - (b_1 - b_2)^2 e^{i2K_{zes}L}}, \tag{120c}$$

$$B_{4,ee,FR} = \frac{(b_1 - b_2)(b_3(1 + r2_{e,FR}^2) - b_1(1 - r2_{e,FR}^2) A_{e,t1,x}^{FR}}{(b_1 + b_2)^2 - (b_1 - b_2)^2 e^{i2K_{zes}L}}. \tag{120d}$$

The *e*-polarized SHG power leaving the sample for this full resonance treatment is proportional to

$$FRP_{e-SHG}^{e-pump} \approx \left(\left| B_{1,ee,FR} \right|^2 + \left| B_{2,ee,FR} \right|^2 + \left| B_{3,ee,FR} \right|^2 + \left| B_{4,ee,FR} \right|^2 + C_{1,ee,FR} + C_{2,ee,FR} + C_{3,ee,FR} \right) \cdot \sec^2 \theta_i, \tag{121}$$

where

$$C_{1,ee,FR} = \mathrm{Re}\{2(B_{1,ee,FR} B_{2,ee,FR}^* + B_{3,ee,FR} B_{4,ee,FR}^*) \cos[(K_{zep} - K_{zes})L]\}, \tag{122a}$$

$$C_{2,ee,FR} = \mathrm{Re}\{2(B_{1,ee,FR} B_{3,ee,FR}^* + B_{2,ee,FR} B_{4,ee,FR}^*) \cos[(K_{zep} + K_{zes})L]\}, \tag{122b}$$

$$C_{3,ee,FR} = \mathrm{Re}\{2[(B_{1,ee,FR} B_{4,ee,FR}^*) \cos(2K_{zes}L) + (B_{2,ee,FR} B_{3,ee,FR}^*) \cos(2K_{zep}L)]\}. \tag{122c}$$

The *e*-polarized SHG produced by an *e*-polarized pump, described by Equation (121), is plotted in Figure 2.22. This is the solution assuming infinite plane waves. Once again, the beam walkoff must be included for this development to accurately represent the second-harmonic output for finite beams since the resonance condition decreases as the incidence angle increases. The second-harmonic beam walkoff factor η_s is the same as was developed in Equation (101). The pump beam walkoff factor η_p is derived

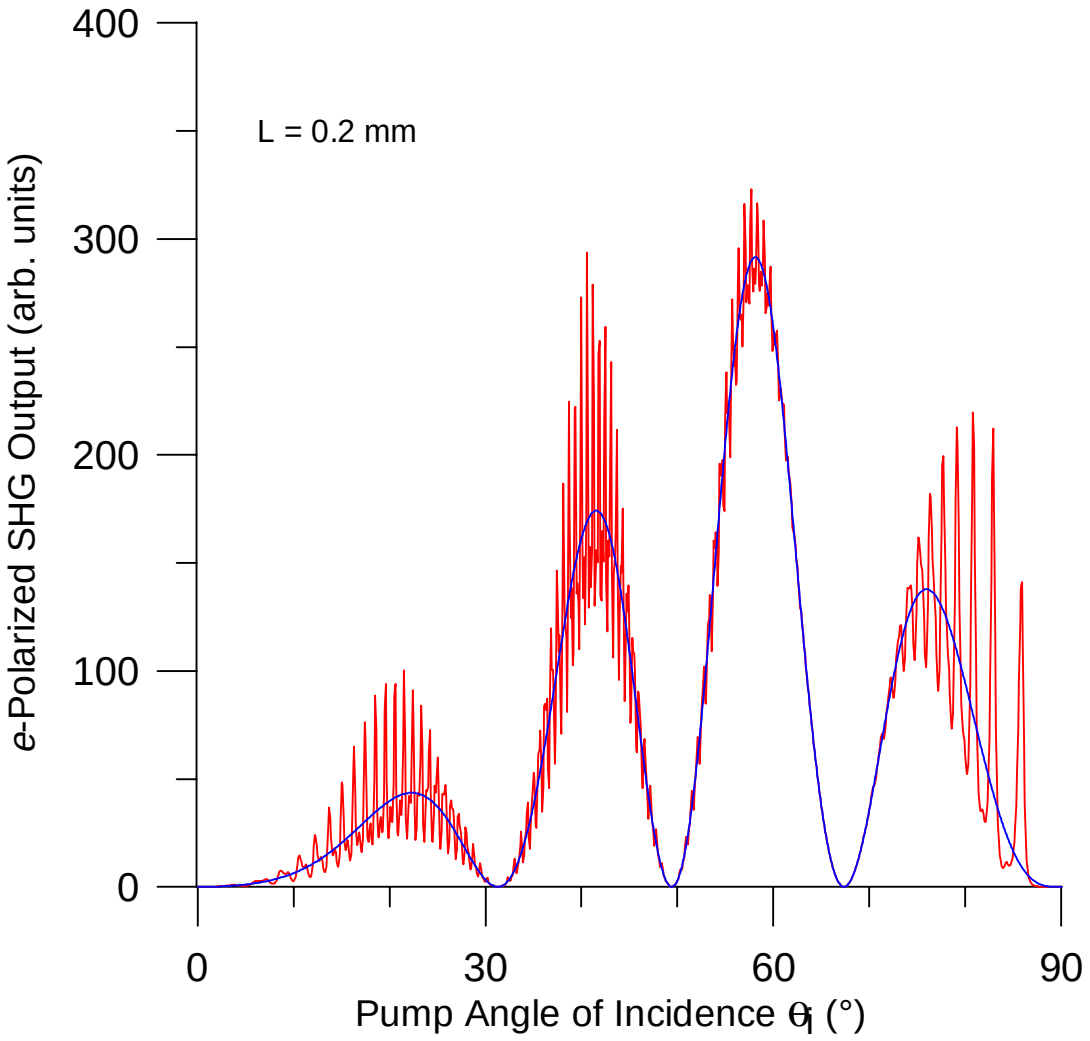

Figure 2.22 Comparison of full resonance $FRP_{e\text{-}SHG}^{e\text{-}pump}$ (red) and single-pass second-harmonic output (blue).

similarly and is

$$\eta_{p,e} = \exp\left[\frac{-x_{p,e}^2}{2d_p^2}\right], \tag{123}$$

where $x_{p,e} = 2L\tan\theta_{ep}$ and d_p is the pump beam diameter. With the overlap factors included, the first surface pump transmission coefficient becomes

$$t1_{e,FR} = \frac{t1_e}{1-\eta_{p,e} r1_e e^{iK_{zep}L}}, \tag{124}$$

and the factors from Equations (120a-d) become

$$B_{1,ee,FR} = \frac{(b_1+b_2)(b_3(1+r2_{e,FR}^2)+b_1(1-r2_{e,FR}^2)A_{e,t1,x}^{FR})}{(b_1+b_2)^2-(b_1-b_2)^2\eta_{s,e}e^{i2K_{zes}L}}, \tag{125a}$$

$$B_{2,ee,FR} = \frac{-2b_1(b_3+b_2A_{e,t1,x}^{FR})}{(b_1+b_2)^2-(b_1-b_2)^2\eta_{s,e}e^{i2K_{zes}L}}, \tag{125b}$$

$$B_{3,ee,FR} = \frac{-2b_1r2_{e,FR}^2(b_3-b_2A_{e,t1,x}^{FR})}{(b_1+b_2)^2-(b_1-b_2)^2\eta_{s,e}e^{i2K_{zes}L}}\eta_{s,e}, \tag{125c}$$

$$B_{4,ee,FR} = \frac{(b_1-b_2)(b_3(1+r2_{e,FR}^2)-b_1(1-r2_{e,FR}^2)A_{e,t1,x}^{FR}}{(b_1+b_2)^2-(b_1-b_2)^2\eta_{s,e}e^{i2K_{zes}L}}\eta_{s,e}. \tag{125d}$$

The resulting second harmonic signal is plotted in Figure 2.23 where d_p = 70 μm and L = 0.2 mm. If the pump diameter is taken to be large, ~1 mm, the full resonance case becomes identical to the single-pass solution. An expanded comparison of the two-pass second-harmonic solution and the full resonance second-harmonic solution is presented in Figure 2.24. This comparison shows that the amplitude of the high frequency component of the full resonance second-harmonic output is larger than that of the two-pass second-harmonic output. The full resonance solution clearly exhibits multiple

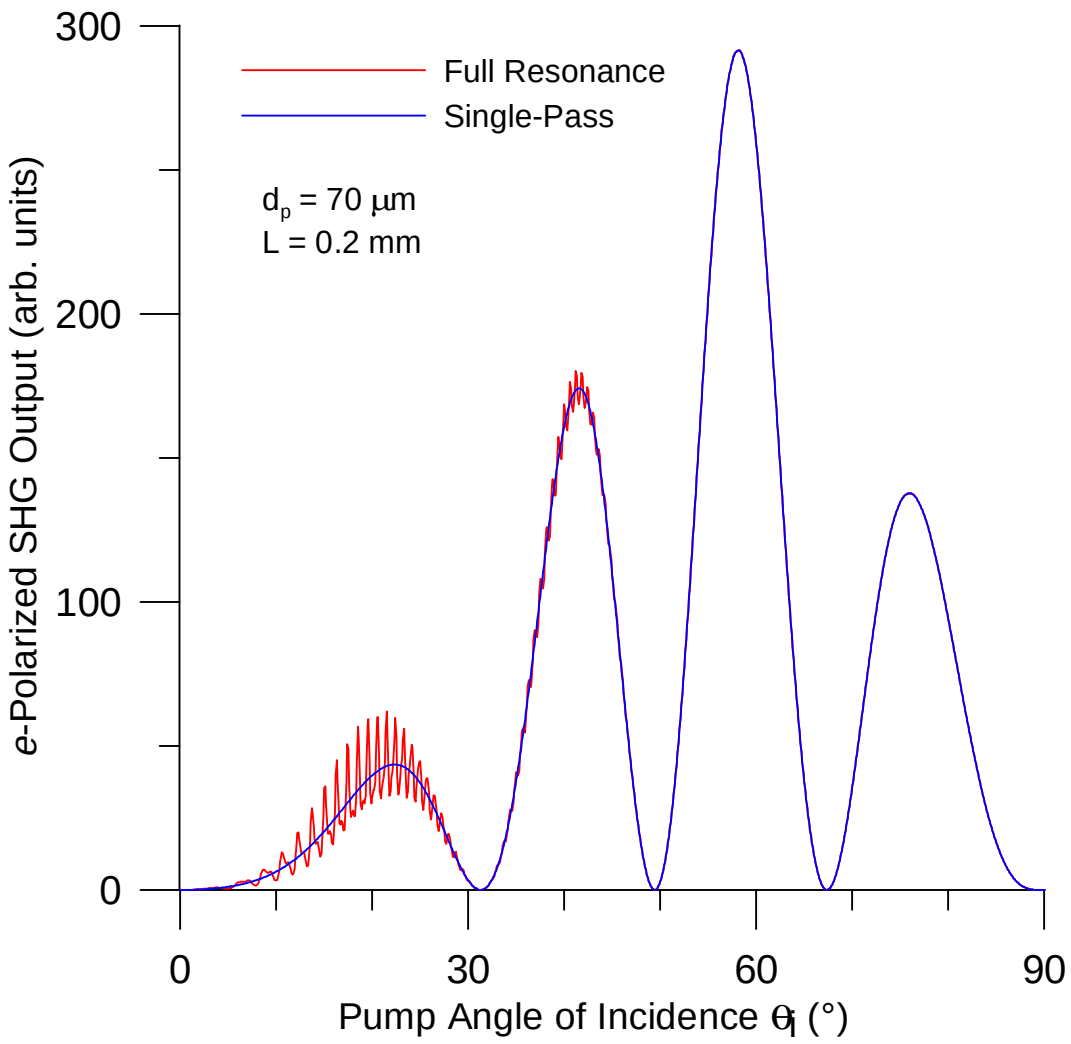

Figure 2.23 Comparison of full resonance *e*-polarized SHG output including the overlap factor, $FROP_{e\text{-}SHG}^{e\text{-}pump}$ (red) with the single-pass solution (blue).

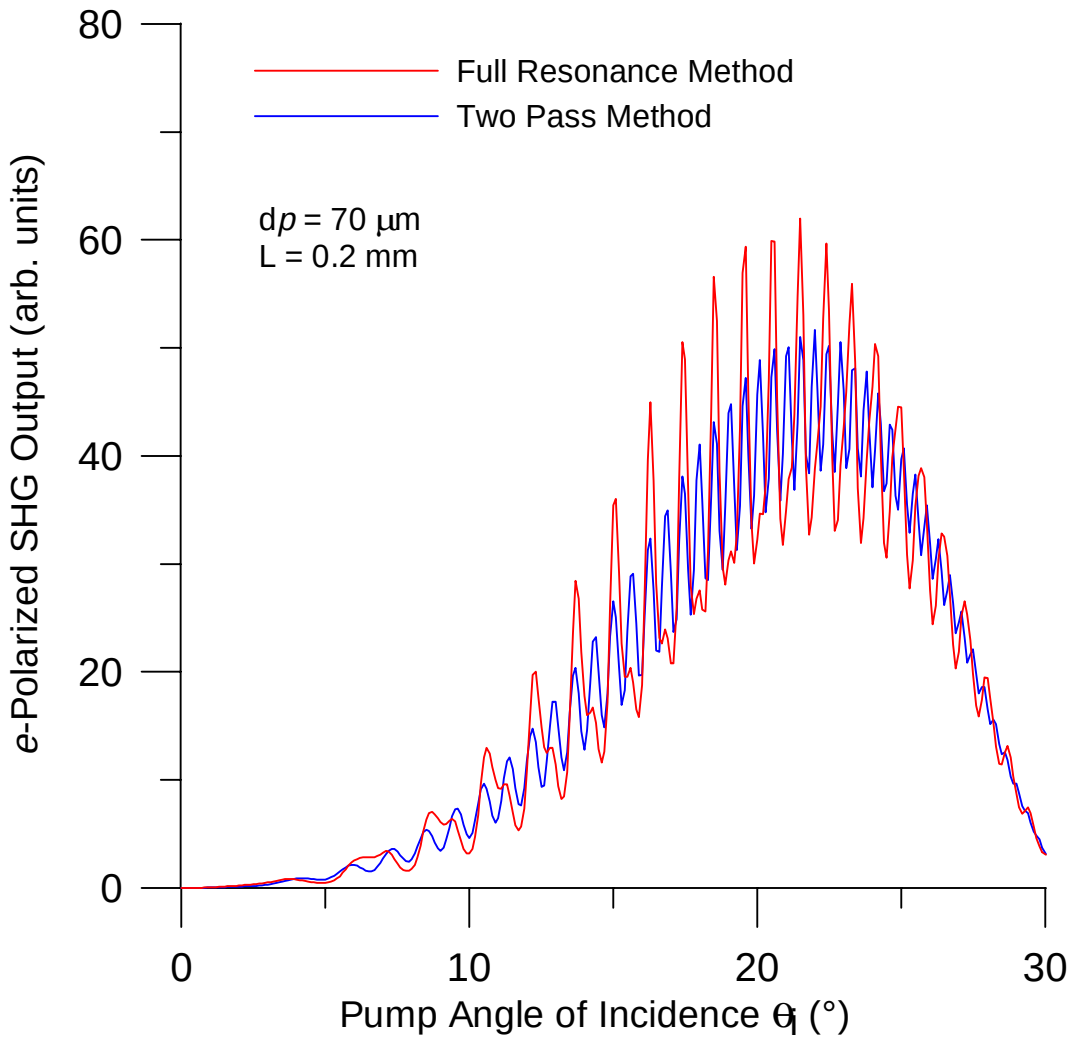

Figure 2.24 Comparison of the *e*-*e* Maker-fringe signal described by the full resonance solution including overlap factors (red) and the two-pass solution including overlap factors (blue).

frequency components, while the two-pass solution visually appears to have only a single high frequency component. Figure 2.25 shows how the full resonance solution fits the data first shown in Figure 2.14. Once again, the pump-beam diameter is 70 μm and the sample thickness is 0.20255 mm. The full resonance solution depicted here is superior to that of the two-pass solution shown in Figure 2.19. The improvement is most noticeable in the agreement of the high frequency fringes.

The preceding pages have detailed the development of the *e*-polarized second-harmonic power generated from an *e*-polarized pump. Using this same procedure, I find that the *o*-polarized second-harmonic power generated from an *e*-polarized pump is proportional to

$$FRP_{o-SHG}^{e-pump} \propto \left|B_{1,eo,FR}\right|^2 + \left|B_{2,eo,FR}\right|^2 + \left|B_{3,eo,FR}\right|^2 + \left|B_{4,eo,FR}\right|^2 + C_{1,eo,FR} + C_{2,eo,FR} + C_{3,eo,FR}, \tag{126}$$

where

$$B_{1,eo,FR} = \frac{(K_{zos}+K_{zs})(K_{zos}(1+r2_{e,FR}^2)+K_{zep}(1-r2_{e,FR}^2))A_{e,t1,y}^{FR}}{(K_{zos}+K_{zs})^2-(K_{zos}-K_{zs})^2\eta_{s,o}e^{i2K_{zos}L}}, \tag{127a}$$

$$B_{2,eo,FR} = \frac{-2K_{zos}(K_{zep}+K_{zs})A_{e,t1,y}^{FR}}{(K_{zos}+K_{zs})^2-(K_{zos}-K_{zs})^2\eta_{s,o}e^{i2K_{zos}L}}, \tag{127b}$$

$$B_{3,eo,FR} = \frac{2K_{zos}(K_{zep}-K_{zs})r2_{e,FR}^2A_{e,t1,y}^{FR}}{(K_{zos}+K_{zs})^2-(K_{zos}-K_{zs})^2\eta_{s,o}e^{i2K_{zos}L}}\eta_{s,o}, \tag{127c}$$

$$B_{4,eo,FR} = \frac{-(K_{zos}-K_{zs})(K_{zos}(1+r2_{e,FR}^2)-K_{zep}(1-r2_{e,FR}^2))A_{e,t1,y}^{FR}}{(K_{zos}+K_{zs})^2-(K_{zos}-K_{zs})^2\eta_{s,o}e^{i2K_{zos}L}}\eta_{s,o}, \tag{127d}$$

$$C_{1,eo,FR} = \mathrm{Re}\left\{2(B_{1,eo,FR}B_{2,eo,FR}^* + B_{3,eo,FR}B_{4,eo,FR}^*)\cos[(K_{zep}-K_{zos})L]\right\}, \tag{127e}$$

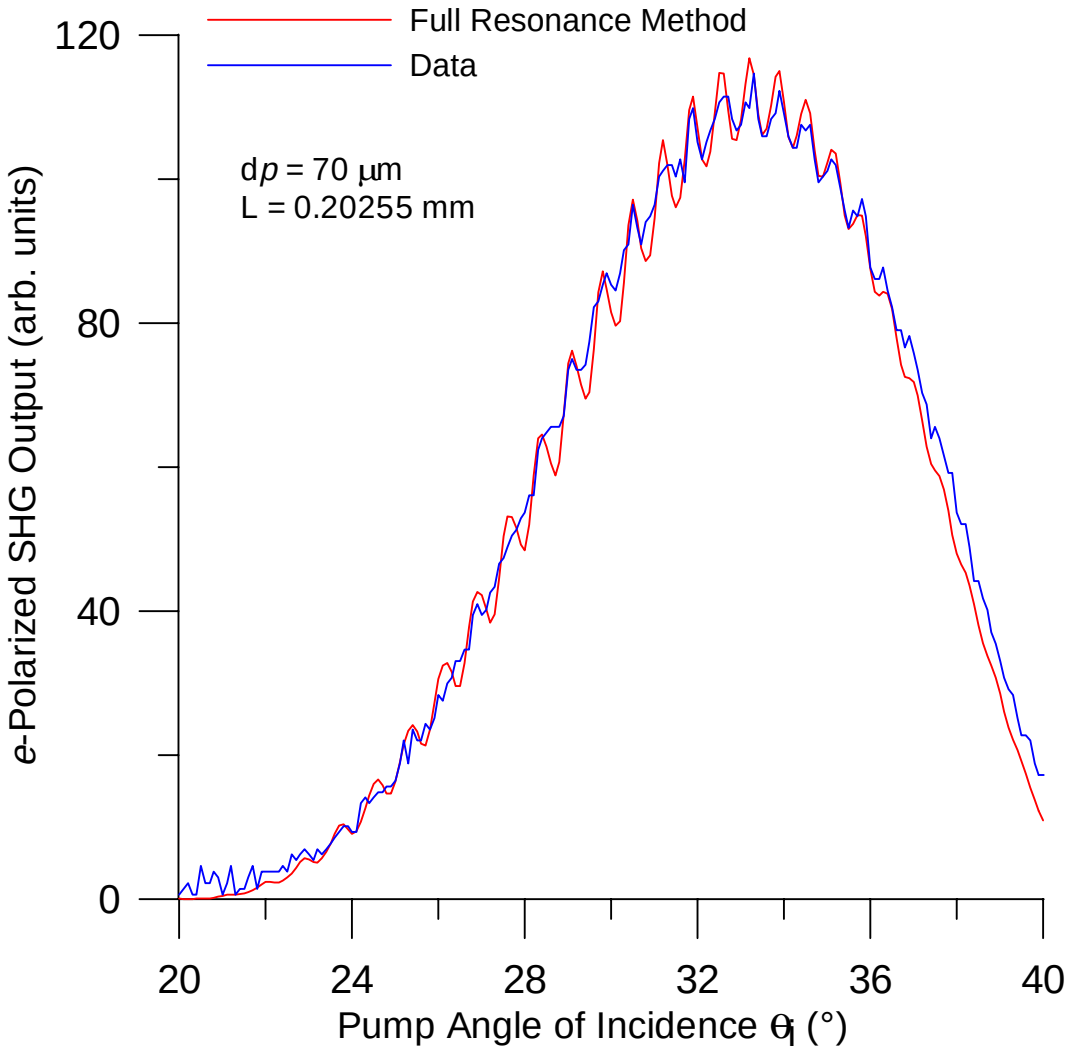

Figure 2.25 Comparison of full resonance solution including overlap factors (red) with data (blue).

$$C_{2,eo,FR} = \mathrm{Re}\left\{2(B_{1,eo,FR}B^*_{3,eo,FR} + B_{2,eo,FR}B^*_{4,eo,FR})\cos[(K_{zep} + K_{zos})L]\right\}, \quad (127f)$$

$$C_{3,eo,FR} = \mathrm{Re}\left\{2[(B_{1,eo,FR}B^*_{4,eo,FR})\cos(2K_{zos}L) + (B_{2,eo,FR}B^*_{3,eo,FR})\cos(2K_{zep}L)]\right\}, \quad (127g)$$

$$A^{FR}_{e,t1,y} = \frac{2d^{(2)}_{22}k_s^2}{k_s^2 n_{o,s}^2 - K_{xep}^2 - K_{zep}^2} t1^2_{e,FR}\cos^2\theta_i\left(E^o_{p,e}\right)^2, \quad (127h)$$

$$K_{zos} = k_s n_{o,s}\cos\theta_{os}, \quad (127i)$$

$$\eta_{s,o} = \exp\left[\frac{-x^2_{s,o}}{2d_s^2}\right], \quad (127j)$$

$$x_{s,o} = 2L\tan\theta_{os}. \quad (127k)$$

The *o*-polarized second-harmonic signal generated from an *e*-polarized pump is plotted in Figure 2.26.

The two remaining cases involve an *o*-polarized pump

$$\vec{E}_{p,o} = \hat{y}E_{p,y} = E^o_{p,y}e^{i(K_{xp}x + K_{zp}z - \omega_p t)}. \quad (128)$$

By going through the development of the fully resonant pump field, as was done in Section 2.4.1 for the *e*-polarized pump, I find that

$$E^o_{p,t1,y} = t1_{o,FR}E^o_{p,y}, \quad (129a)$$

$$E^o_{p,r2,y} = t1_{o,FR}r2_{o,FR}E^o_{p,y}e^{iK_{poz}L}, \quad (129b)$$

where

$$t1_{o,FR} = \frac{2t1_o}{1 - \eta_{p,o}r1_o^2 e^{iK_{zop}L}}, \quad (130a)$$

$$r2_{o,FR} = r2_o, \quad (130b)$$

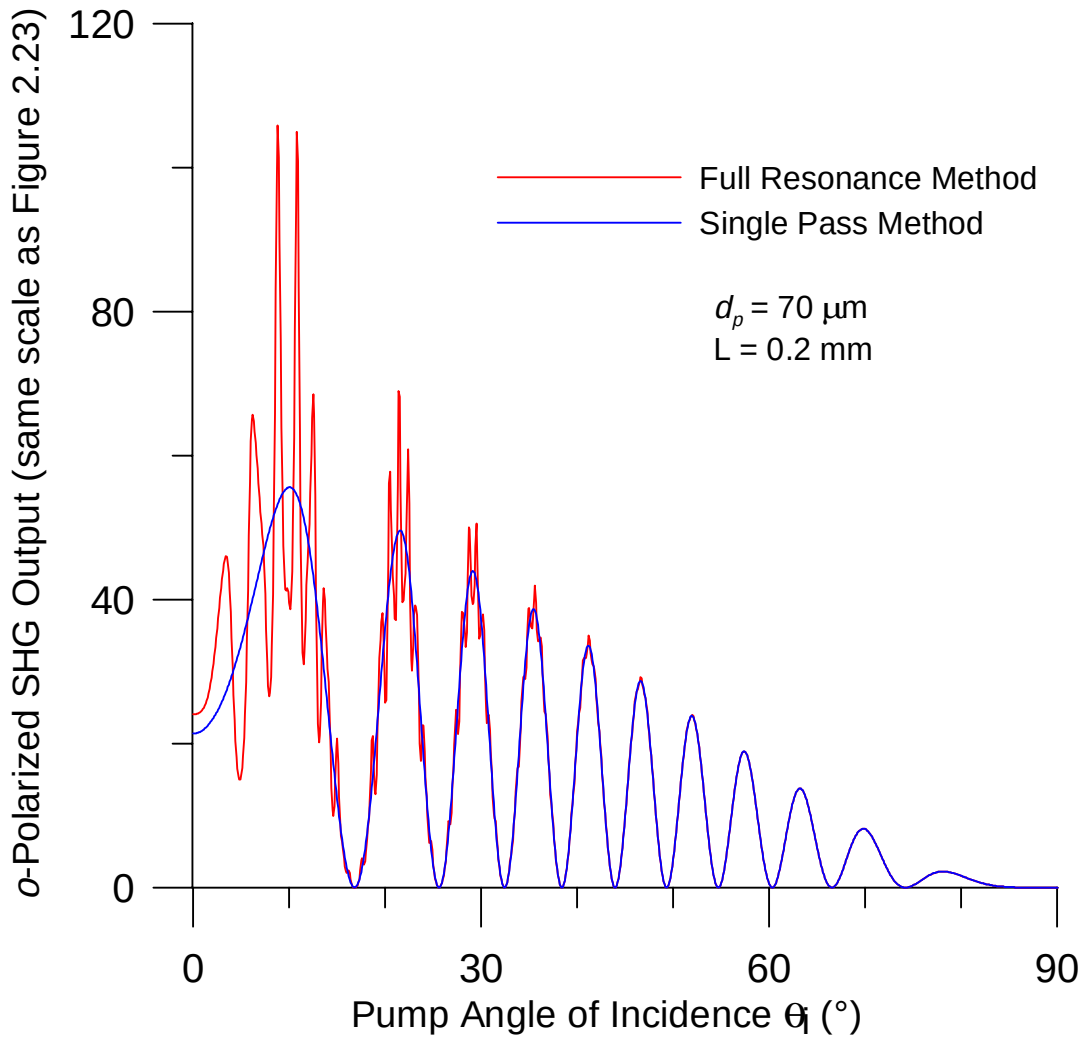

Figure 2.26 Comparison of full resonance *o*-polarized SHG for *e*-polarized pump, including overlap factors, $FRP_{o\text{-}SHG}^{e\text{-}pump}$ (red) with single-pass solution (blue).

$$K_{poz} = k_p n_{o,p} \cos\theta_{op}, \tag{130c}$$

$$K_{zop} = k_s n_{o,p} \cos\theta_{op} = 2K_{poz}, \tag{130d}$$

$$\eta_{p,o} = \exp\left[\frac{-x_{p,o}^2}{2d_p^2}\right], \tag{130e}$$

$$x_{p,o} = 2L\tan\theta_{op}. \tag{130f}$$

The *o*-polarized SHG output for an *o*-polarized pump is given by

$$FRP_{o-SHG}^{o-pump} \propto \left|B_{1,oo,FR}\right|^2 + \left|B_{2,oo,FR}\right|^2 + \left|B_{3,oo,FR}\right|^2 + \left|B_{4,oo,FR}\right|^2 + C_{1,oo,FR} + C_{2,oo,FR} + C_{3,oo,FR}, \tag{131}$$

where

$$B_{1,oo,FR} = \frac{(K_{zos}+K_{zs})(K_{zos}(1+r2_{o,FR}^2)+K_{zop}(1-r2_{o,FR}^2))A_{o,t1,y}^{FR}}{(K_{zos}+K_{zs})^2-(K_{zos}-K_{zs})^2\eta_{s,o}e^{i2K_{zos}L}}, \tag{132a}$$

$$B_{2,oo,FR} = \frac{-2K_{zos}(K_{zop}+K_{zs})A_{o,t1,y}^{FR}}{(K_{zos}+K_{zs})^2-(K_{zos}-K_{zs})^2\eta_{s,o}e^{i2K_{zos}L}}, \tag{132b}$$

$$B_{3,oo,FR} = \frac{2K_{zos}(K_{zop}-K_{zs})r2_{o,FR}^2 A_{o,t1,y}^{FR}}{(K_{zos}+K_{zs})^2-(K_{zos}-K_{zs})^2\eta_{s,o}e^{i2K_{zos}L}}\eta_{s,o}, \tag{132c}$$

$$B_{4,oo,FR} = \frac{-(K_{zos}-K_{zs})(K_{zos}(1+r2_{o,FR}^2)-K_{zop}(1-r2_{o,FR}^2))A_{o,t1,y}^{FR}}{(K_{zos}+K_{zs})^2-(K_{zos}-K_{zs})^2\eta_{s,o}e^{i2K_{zos}L}}\eta_{s,o}, \tag{132d}$$

$$C_{1,oo,FR} = \mathrm{Re}\{2(B_{1,oo,FR}B_{2,oo,FR}^* + B_{3,oo,FR}B_{4,oo,FR}^*)\cos[(K_{zop}-K_{zos})L]\}, \tag{132e}$$

$$C_{2,oo,FR} = \mathrm{Re}\{2(B_{1,oo,FR}B_{3,oo,FR}^* + B_{2,oo,FR}B_{4,oo,FR}^*)\cos[(K_{zop}+K_{zos})L]\}, \tag{132f}$$

$$C_{3,oo,FR} = \mathrm{Re}\{2[(B_{1,oo,FR}B_{4,oo,FR}^*)\cos(2K_{zos}L) + (B_{2,oo,FR}B_{3,oo,FR}^*)\cos(2K_{zop}L)]\}, \tag{132g}$$

$$A_{o,t1,y}^{FR} = \frac{-2d_{22}^{(2)}k_s^2}{k_s^2 n_{o,s}^2 - K_{xop}^2 - K_{zop}^2} t1_{o,FR}^2 \left(E_{p,y}^o\right)^2, \tag{132h}$$

$$K_{xop} = k_s n_{o,p} \sin\theta_{op}, \tag{132i}$$

$$K_{zop} = k_s n_{o,p} \cos\theta_{op}. \tag{132j}$$

The *o*-polarized second-harmonic signal generated from an *o*-polarized pump is plotted in Figure 2.27.

The fully resonant *e*-polarized SHG output is then given by

$$FRP_{e-SHG}^{o-pump} \propto \left(\left|B_{1,oe,FR}\right|^2 + \left|B_{2,oe,FR}\right|^2 + \left|B_{3,oe,FR}\right|^2 + \left|B_{4,oe,FR}\right|^2 + C_{1,oe,FR} + C_{2,oe,FR} + C_{3,oe,FR}\right) \cdot \sec^2\theta_i, \tag{133}$$

where

$$B_{1,oe,FR} = \frac{(b_1 + b_2)(b_{3,o}(1 + r2_{o,FR}^2) + b_1(1 - r2_{o,FR}^2)A_{o,t1,x}^{FR})}{(b_1 + b_2)^2 - (b_1 - b_2)^2 \eta_{s,e} e^{i2K_{zes}L}}, \tag{134a}$$

$$B_{2,oe,FR} = \frac{-2b_1(b_{3,o} + b_2 A_{o,t1,x}^{FR})}{(b_1 + b_2)^2 - (b_1 - b_2)^2 \eta_{s,e} e^{i2K_{zes}L}}, \tag{134b}$$

$$B_{3,oe,FR} = \frac{-2b_1(b_{3,o} - b_2 A_{o,t1,x}^{FR}) r2_{o,FR}^2}{(b_1 + b_2)^2 - (b_1 - b_2)^2 \eta_{s,e} e^{i2K_{zes}L}} \eta_{s,e}, \tag{134c}$$

$$B_{4,oe,FR} = \frac{(b_1 - b_2)(b_{3,o}(1 + r2_{o,FR}^2) - b_1(1 - r2_{o,FR}^2)A_{o,t1,x}^{FR})}{(b_1 + b_2)^2 - (b_1 - b_2)^2 \eta_{s,e} e^{i2K_{zes}L}} \eta_{s,e}, \tag{134d}$$

$$C_{1,oe,FR} = \mathrm{Re}\{2(B_{1,oe,FR}B_{2,oe,FR}^* + B_{3,oe,FR}B_{4,oe,FR}^*)\cos[(K_{zop} - K_{zes})L]\}, \tag{134e}$$

$$C_{2,oe,FR} = \mathrm{Re}\{2(B_{1,oe,FR}B_{3,oe,FR}^* + B_{2,oe,FR}B_{4,oe,FR}^*)\cos[(K_{zop} + K_{zes})L]\}, \tag{134f}$$

$$C_{3,oe,FR} = \mathrm{Re}\{2[(B_{1,oe,FR}B_{4,oe,FR}^*)\cos(2K_{zes}L) + (B_{2,oe,FR}B_{3,oe,FR}^*)\cos(2K_{zop}L)]\}, \tag{134g}$$

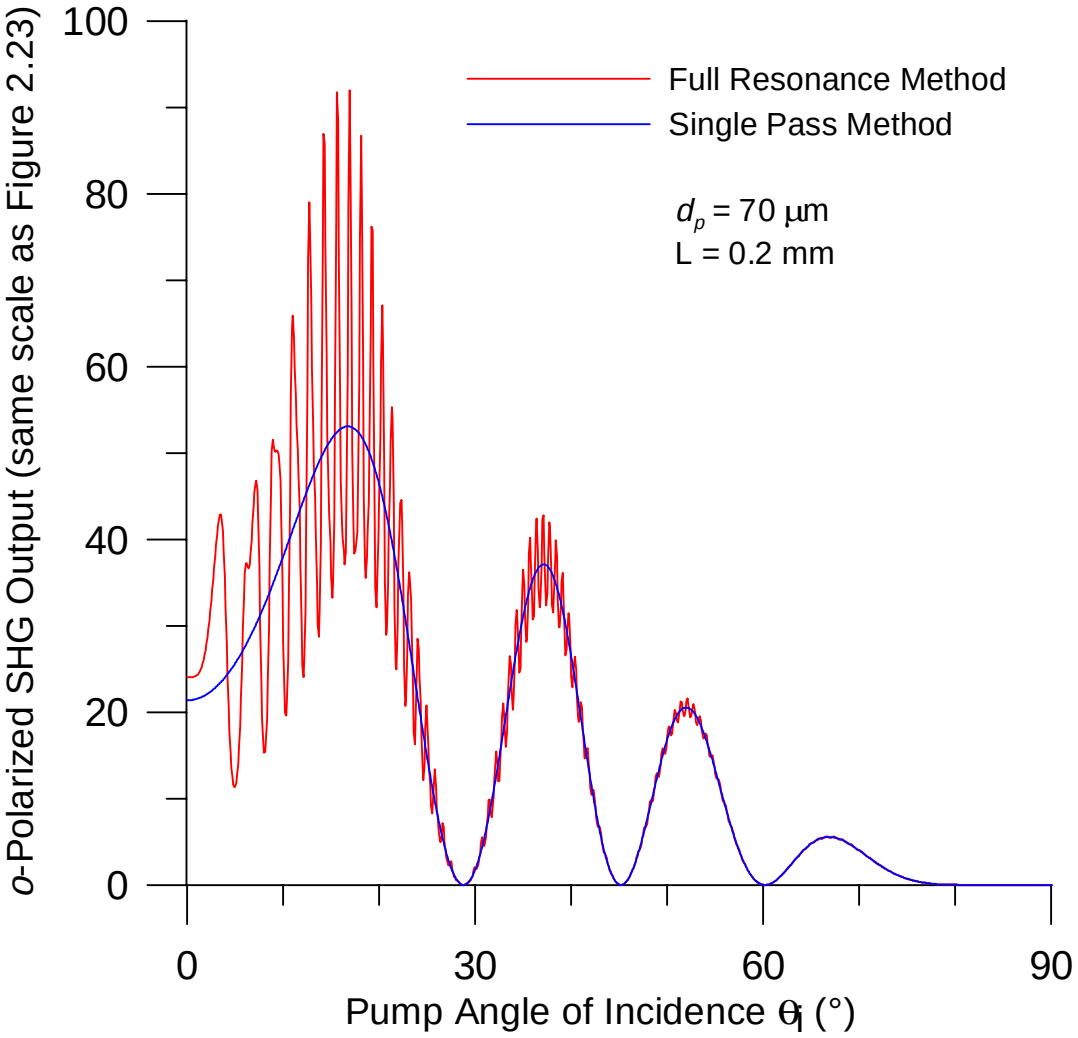

Figure 2.27 Comparison of full resonance *o*-polarized SHG for *o*-polarized pump, with overlap factor, $FROP^{o\text{-}pump}_{o\text{-}SHG}$ (red) with single-pass solution (blue).

$$b_{3,o} = -K_{xop}A^{FR}_{o,t1,z} + K_{zop}A^{FR}_{o,t1,x}\,, \tag{134h}$$

$$A^{FR}_{o,t1,x} = \frac{2d^{(2)}_{31}K_{xop}K_{zop}}{k_s^2 n^2_{o,s}n^2_{e,s} - n^2_{o,s}K^2_{xop} - n^2_{e,s}K^2_{zop}}\, t1^2_{o,FR}\left(E^o_{p,y}\right)^2, \tag{134i}$$

$$A^{FR}_{o,t1,z} = \frac{2d^{(2)}_{31\ 31}(K^2_{zop} - k_s^2 n^2_{o,s})}{k_s^2 n^2_{o,s}n^2_{e,s} - n^2_{o,s}K^2_{xop} - n^2_{e,s}K^2_{zop}}\, t1^2_{o,FR}\left(E^o_{p,y}\right)^2. \tag{134j}$$

The *e*-polarized second-harmonic signal generated from an *o*-polarized pump is plotted in Figure 2.28.

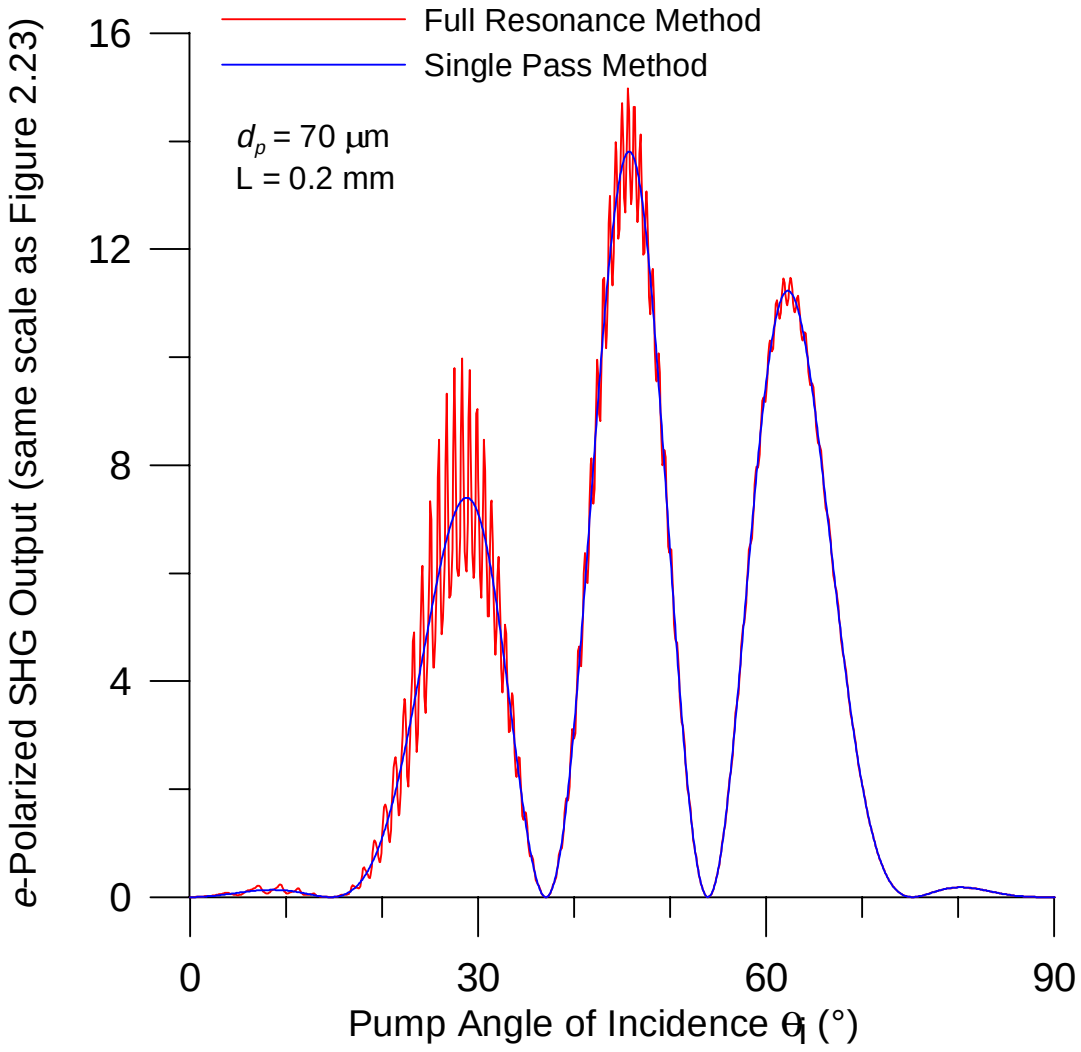

Figure 2.28 Comparison of full resonance *e*-polarized SHG for *o*-polarized pump, with overlap factor, $FRP_{e\text{-}SHG}^{o\text{-}pump}$ (red) with single-pass solution (blue).

Chapter 3

Experiments

3.0 Introduction

Due to the breadth of the research undertaken during this thesis there are two significant experimental setups to discuss. The first was the Maker fringe system used to generate and record second-harmonic signals from a number of $LiNbO_3$ samples. The second was the electric-field poling system used to perform spontaneous polarization domain reversal within $LiNbO_3$ wafers.

3.1 Maker Fringe System

The Maker fringe experiment consisted of a 4-axis positioning system, Nd:YAG laser operated at 1.064 μm, photomultiplier tubes (PMTs) with associated electronics, various optics, and a control computer. This system is schematically represented in Figure 3.1 (a). A picture of the system is shown in Figure 3.1 (b). The positioning system provided motion in x, y, z, and θ. The computer controlled the positioning system and the data acquisition. Wafers were mounted to the positioning system with a sample holder that provided reference flats so that repeatable registration of the samples was possible.

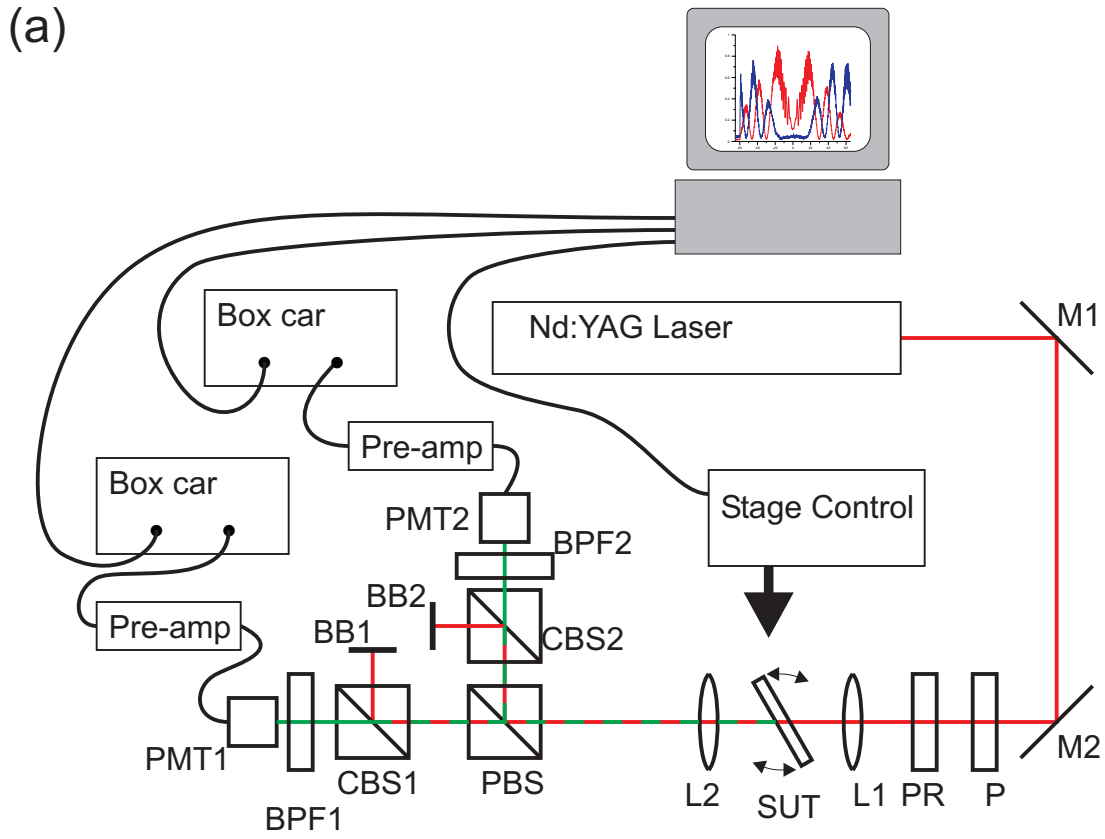

Figure 3.1 Maker-fringe apparatus (a) schematic representation, (b) photograph. M mirror, P polarizer, PR polarization rotator, L lens, SUT sample under test, PBS polarizing beam splitter, CBS chromatic beam splitter, BB beam block, BPF band pass filter, PMT photomultiplier tube.

The samples were oriented in the holder so that the crystallographic *y*-axis of the $LiNbO_3$ was oriented vertically and the *x*-axis was oriented horizontally. Rotation was about the *y*-axis. The pump beam intersected the sample at the rotation axis.

The pump laser polarization was set to either the *o*- or *e*-polarization by means of a half-wave plate. The pump was focused using a 300 mm focal length lens to 1/e diameter of approximately 60 μm at the test sample. The output SHG was collected and refocused with a 300 mm focal length lens. The *o*- and *e*-polarized SHG signals were separated from one another using a Glan type polarizing beam splitter which directed each signal to its own PMT. In the most recent iteration of the system, the pump laser was operated mode-locked and Q-switched. The PMT signals were run through box car averagers and finally into an analog to digital (A/D) converter. Earlier versions of the system used a continuous wave (CW) laser, optical chopper, and lock-in detection of the SHG signals.

The SHG signals were recorded as a function of pump beam angle of incidence. This was accomplished by rotating the sample as the data were taken. The angular resolution of the data was 0.1º. The data acquisition was synchronized to the encoder pulse signal (0.0008º/pulse) from the rotation stage.

The software written to control the Maker fringe system was designed to allow flexibility in the data acquisition. The angular range of a scan was selectable, as was the number of points to be scanned and the distance

between points in the *x*- and *y*-directions. This allowed for doing single-point scans as well as full wafer maps. Once stored, these SHG signals were analyzed using the Maker fringe theory presented in Chapter 2.

3.2 Electric-Field Poling System

The major component of the electric-field poling system was a high-voltage, variable-width pulse generator capable of delivering pulses from 0.5 to 15.5 kV for up to 5 ms. The rest of the system consisted of a data acquisition computer, a digital storage oscilloscope, an electronic filter, and an acrylic poling cell. Figure 3.2 (a) shows a schematic of the system while Figure 3.2 (b) shows a picture of the actual setup.

The HV pulse generator provided two built-in monitoring ports. One port provided a 1000:1 reduction of the high voltage supplied to the sample. The other port provided a voltage signal proportional to the current flowing through the system. The response of this signal was 2.0 V/A. The voltage-monitoring signal was connected directly to the oscilloscope. The current-monitoring signal ran through a conditioning filter and then to the oscilloscope. The conditioning filter was used to remove DC and 60 Hz noise from the current signal. The computer was used to arm the oscilloscope for recording single pulse events. Both the voltage and current traces were downloaded to the computer where they were stored and approximate delivered charge measurements were made.

(a)

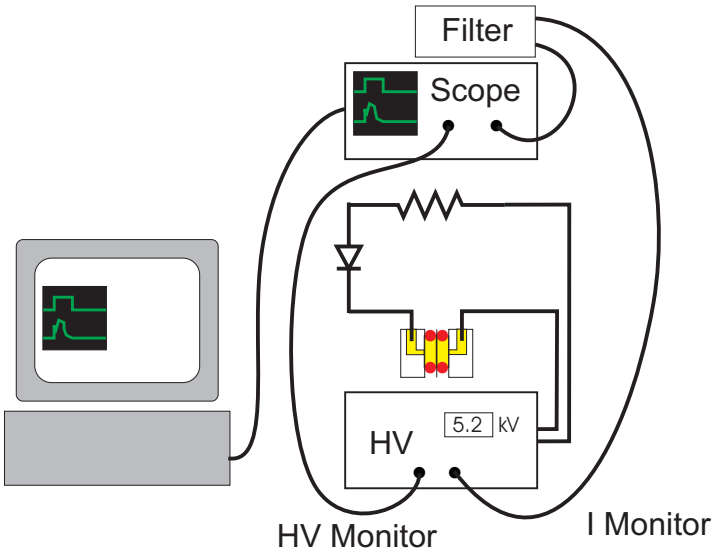

(b)

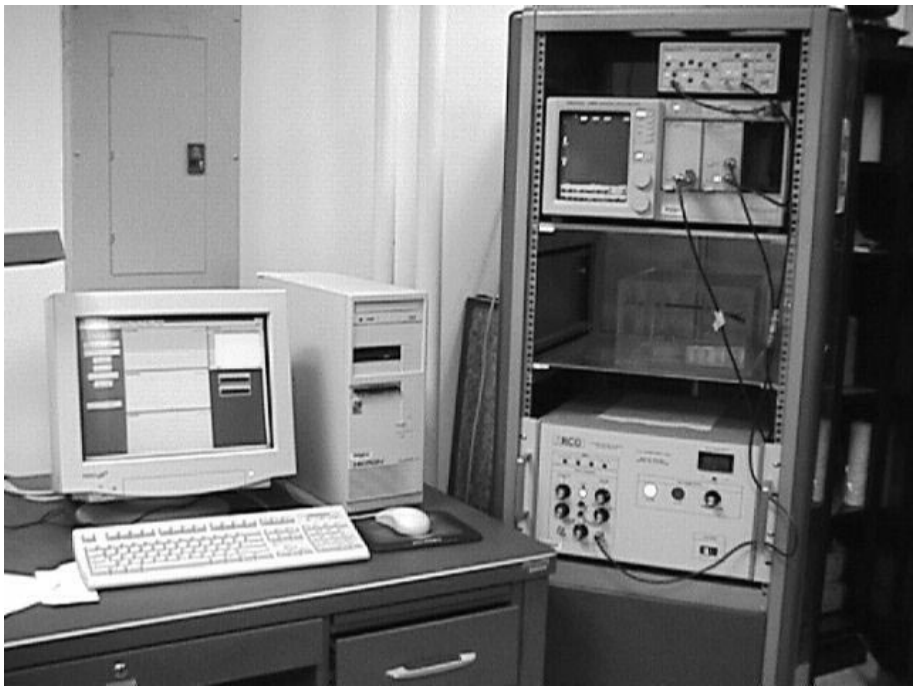

Figure 3.2 Electric-field poling setup (a) schematic, (b) photograph.

The poling cell was modeled after that used by Myers [Myers ‘95]. The cell was constructed from two acrylic blocks approximately 25 × 50 × 50 mm. Each block had a reservoir with a feed through leading to the sample’s position. A silicone o-ring was used to seal the acrylic block to the sample. The entire cell was held together using 4 bolts around the perimeter of the blocks. During later stages of the poling experiments, springs were used in series with the bolts to equalize the pressure generated by each bolt. Figures 3.3 (a) and (b) show a cross-sectional view of the poling cell and a picture of the actual cell used.

Electrical contact was made to the sample by filling the reservoirs with an electrolyte, that consisted of LiCl dissolved in de-ionized water in a ratio of 2:1 by mass. The circuit from the HV pulse generator to the poling cell and back was completed in the following manner. An RG 11A coaxial cable connected the high-voltage output to the poling circuit. The poling circuit, pictured in Figure 3.4, was constructed on an acrylic base plate and consisted of a 10 kΩ resistor, a high-voltage diode, and the poling cell, all connected in series using 16 AWG copper wire. The series resistor provided protection for the pulse generator in the event of a short in the poling circuit. The diode was needed to prevent domain “flip-back” after the voltage pulse had finished. Figure 3.5 shows the difference between current traces taken with and without the high-voltage diode in the circuit. Without the diode a current flows in the opposite direction to the poling current after the voltage pulse has

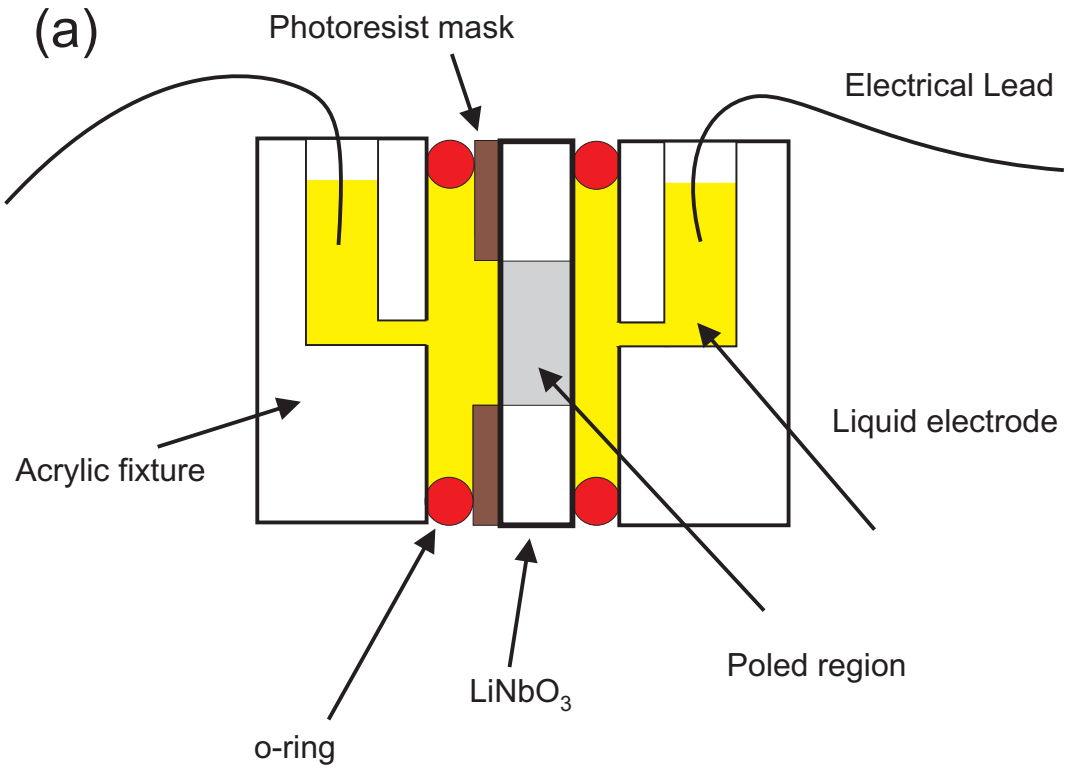

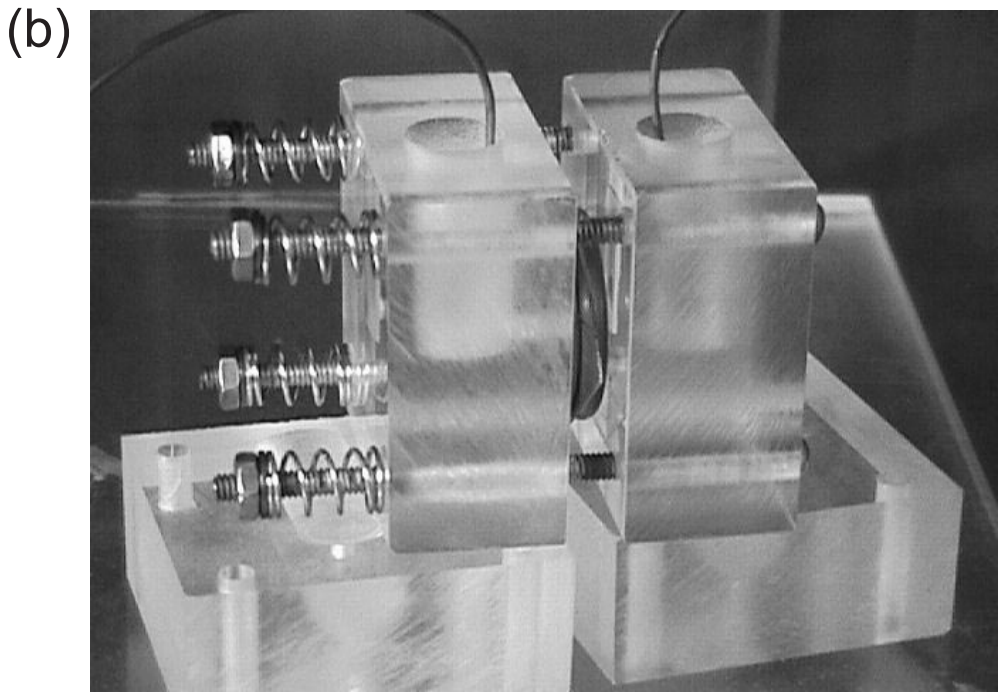

Figure 3.3 Details of the poling cell (a) cross sectional view, (b) photograph.

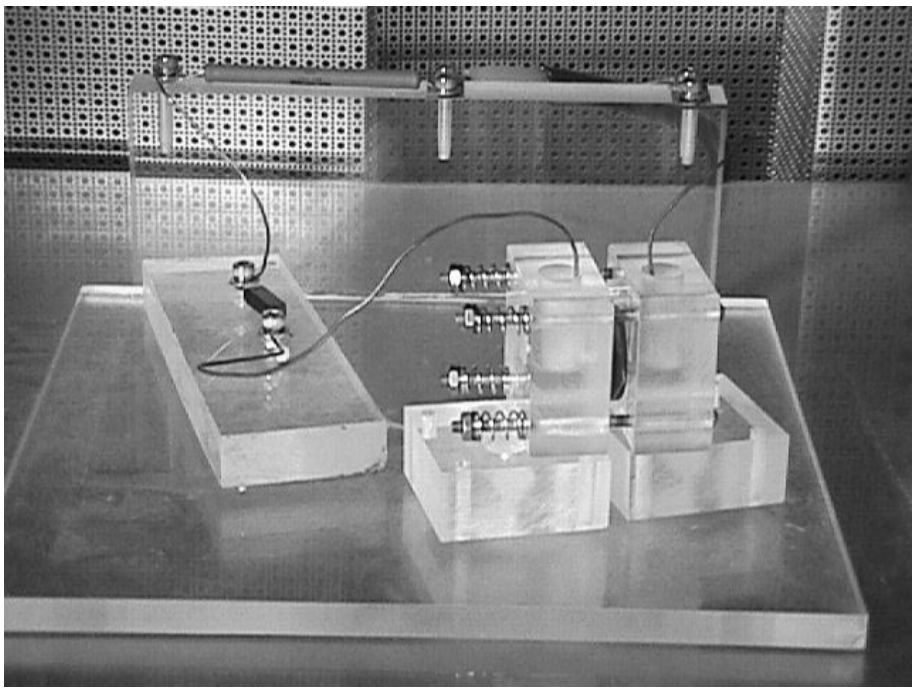

Figure 3.4 Photograph of the poling cell in the electric-field poling system.

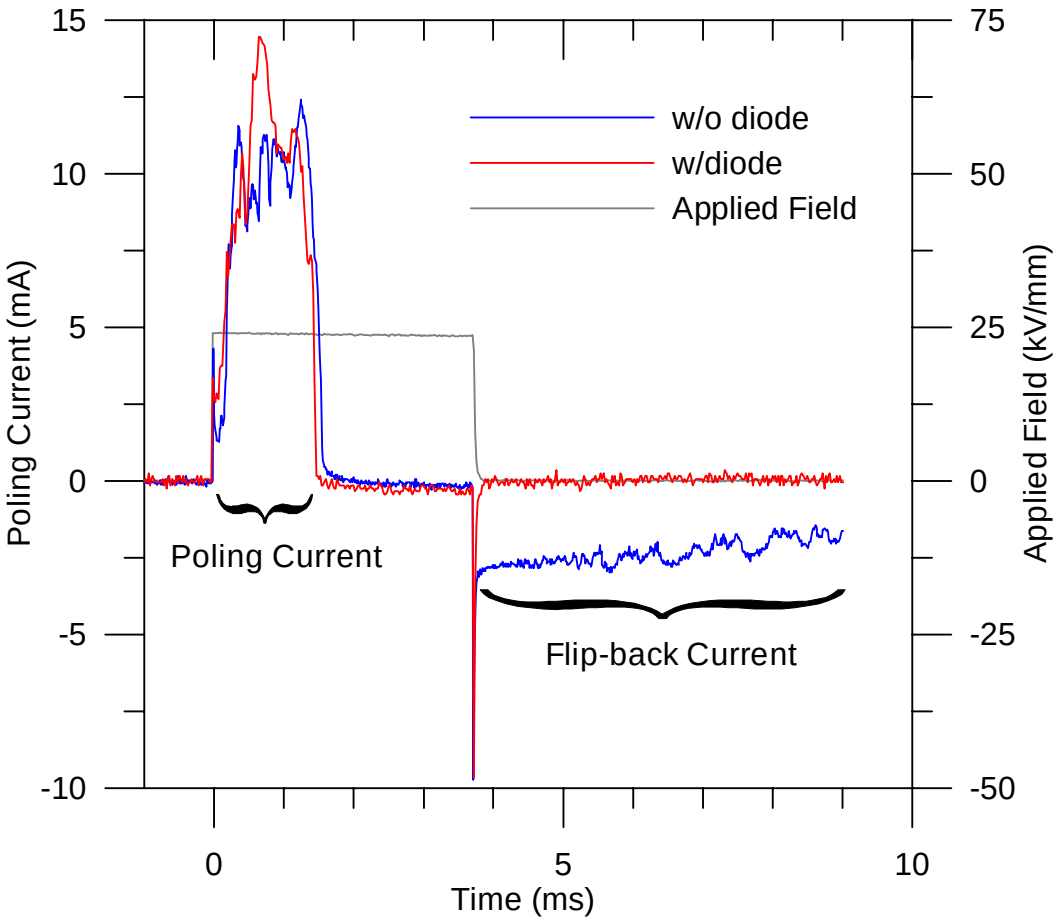

Figure 3.5 Effect of the high-voltage diode in the poling circuit. The blue trace is without the diode. The red trace is with the diode. The gray trace is a supperposition of the applied electric field.

ended. This current is due to the reversed domain flipping back to its original direction. With the diode in the poling circuit, the only current seen after the voltage pulse has ended is the capacitance discharge of the sample.

The poling experiments proceeded one pulse at a time. With each pulse the voltage and the current traces were recorded. The charge delivered to the sample was calculated by integrating the current trace. Complete domain reversal is accomplished when the total charge Q delivered to the sample is

$$Q = \int i\,dt = 2P_s A\,, \tag{135}$$

where i is the displacement current flowing in the circuit, P_s is the spontaneous polarization, and A is the area being poled.

The electric-field poling system was used for several different poling applications. It was used to pole test patches for analysis with the Maker fringe system (see Section 4.4). It was used to examine the poling current characteristics for different poling fields (see Section 4.5). And, finally, it was used to fabricate periodically poled $LiNbO_3$ (PPLN) chips for performing various nonlinear frequency conversions. The details pertaining to the PPLN can be found in Jeff Mitchell's Master of Science thesis [Mitchell '99].

Chapter 4

Data Analysis

4.0 Introduction

The data analysis is broken down into several subsections. While the order of these subsections makes for a smooth progression of the analysis, it is not the order in which they were encountered. Insight obtained from the final stages of this research has shed light onto some of the observations made early on and has led to a better understanding of the limitations of Maker fringe analysis.

I will start by examining the Maker-fringe signals from as-received samples of $LiNbO_3$. This will involve fitting to several parameter combinations involving thickness, index of refraction, electric field, nonlinear susceptibilities, and electrooptic coefficients. The results from this section suggest that the extraordinary index of refraction n_e deviates from that predicted by the Sellmeier equations [Edwards '83]. A close examination of the literature has led to a possible explanation for this observation.

Next I will examine the possibility of determining some of the nonlinear $d_{ij}^{(2)}$ and electrooptic r_{ij} coefficients using Maker fringe analysis. The ratio of $d_{33}^{(2)} / d_{31}^{(2)}$ will be investigated by observing how the amplitude of the Maker fringe theory changes with this ratio. The electrooptic coefficients r_{33} and r_{13}

will be examined by observing the change in the Maker fringe signal during the application of an electric field to the sample.

I will then examine the effect of electric-field-induced domain reversal in $LiNbO_3$ using Maker fringe analysis.

Last, I will explore one aspect of electric field poling, the maximum current density as a function of applied field, and attempt to correlate these results with those obtained during the Maker fringe analysis.

4.1 Maker-Fringe Analysis of As-Received $LiNbO_3$

The data analysis in this section involves several different fitting parameter combinations for fitting the Maker fringe theory, derived in Chapter 2, to the data. I have written several Fortran programs using Equations (121), (126), (131), and (133). These programs, later referred to as solvers, are used to solve each pump-SHG case separately or simultaneously. The first series of fits used just the thickness of the sample as the fitting parameter. This was done separately for each of the 4 pump-SHG cases. Next, the 4 pump-SHG cases were fitted simultaneously to sample thickness, and finally all 4 cases were fitted simultaneously to combinations of sample thickness and index deviations from the Sellmeier equations.

The Maker-fringe scans were typically taken over pump angles of incidence between -65º and +65º. The scans were analyzed by fitting over this entire angular range. However, in order to facilitate the visibility of the

fringe features, the Maker-fringe scans are displayed for positive angles only. A least squared error (LSE) approach was used to determine which parameters led to the best fits. In order to improve the fidelity of the least square error, both the data and the theoretical Maker-fringe signals were normalized to the areas under their curves before the LSE was calculated. The refractive indices used in the theoretical calculations were generated from Sellmeier equations derived by Edwards and Lawrence [Edwards '84]. Using these Sellmeier equations at a temperature of 25 ºC, the four indices of refraction are: n_{op} = 2.23218, n_{os} = 2.32318, n_{ep} = 2.15603, and n_{es} = 2.23424.

The first set of data for this section were taken from a portion of a 75 mm diameter, 0.2 mm thick $LiNbO_3$ wafer. The sub-wafer consisted of one quarter of the original wafer, produced by cutting the wafer in half once vertically and once horizontally. This sample will be referred to as Sample A.

The initial observation of these data was that the overlap factors used to predict the tapering-off of the high frequency fringe amplitude were inadequate, at least from an aesthetic point of view. Therefore, overlap factors were constructed by fitting the high frequency fringe amplitude of the theory to that of the data. This led to two different overlap factors, one for the *o*-polarized SHG η_o and one for the *e*-polarized SHG η_e. η_o was found by fitting the high frequency fringe amplitude as a function of pump incidence angle for the *o*-*o* case, while η_e was found by using the *o*-*e* case. The two factors were

$$\eta_o(\theta_i) = 0.8611\exp(-0.0596 \cdot \theta_i), \tag{136a}$$

$$\eta_e(\theta_i) = 0.00004 \cdot \theta_i^2 - 0.0035 \cdot \theta_i + 0.2015. \tag{136b}$$

Implementing these heuristic overlap factors into the Maker fringe code led to much better fits of the high frequency fringes. However, they ultimately resulted in the same fitting parameter solutions as the original overlap factors, thus demonstrating the overall robustness of the solution procedure.

Solving for the sample thickness over a range of 0.18 to 0.22 mm with 0.01 μm steps for each of the 4 cases individually resulted in the data found in Table 4.1.

Table 4.1 Thickness solutions for Sample A. Each pump-SHG case fit individually.

Pump-SHG case	*L* (mm)
o-o	0.19960
o-e	0.19951
e-o	0.19960
e-e	0.19395

Figure 4.1 shows the comparisons between the data and the theoretical fits for each of the pump-SHG cases using the sample thickness as the only fitting parameter. The theoretical traces match both the high and low frequency fringes of the data very well. The most obvious exception is the slight walkoff of the low frequency fringes at high angles of incidence for the *o-e* and *e-o* cases. However, one problem with these results is that all of these data were taken at the same location on the sample and therefore must have the same sample thickness. I will discuss the resolution of this problem next.

The relatively large discrepancy between the thickness found for the *e-e* case and that found for the other 3 cases is an example of what I call a

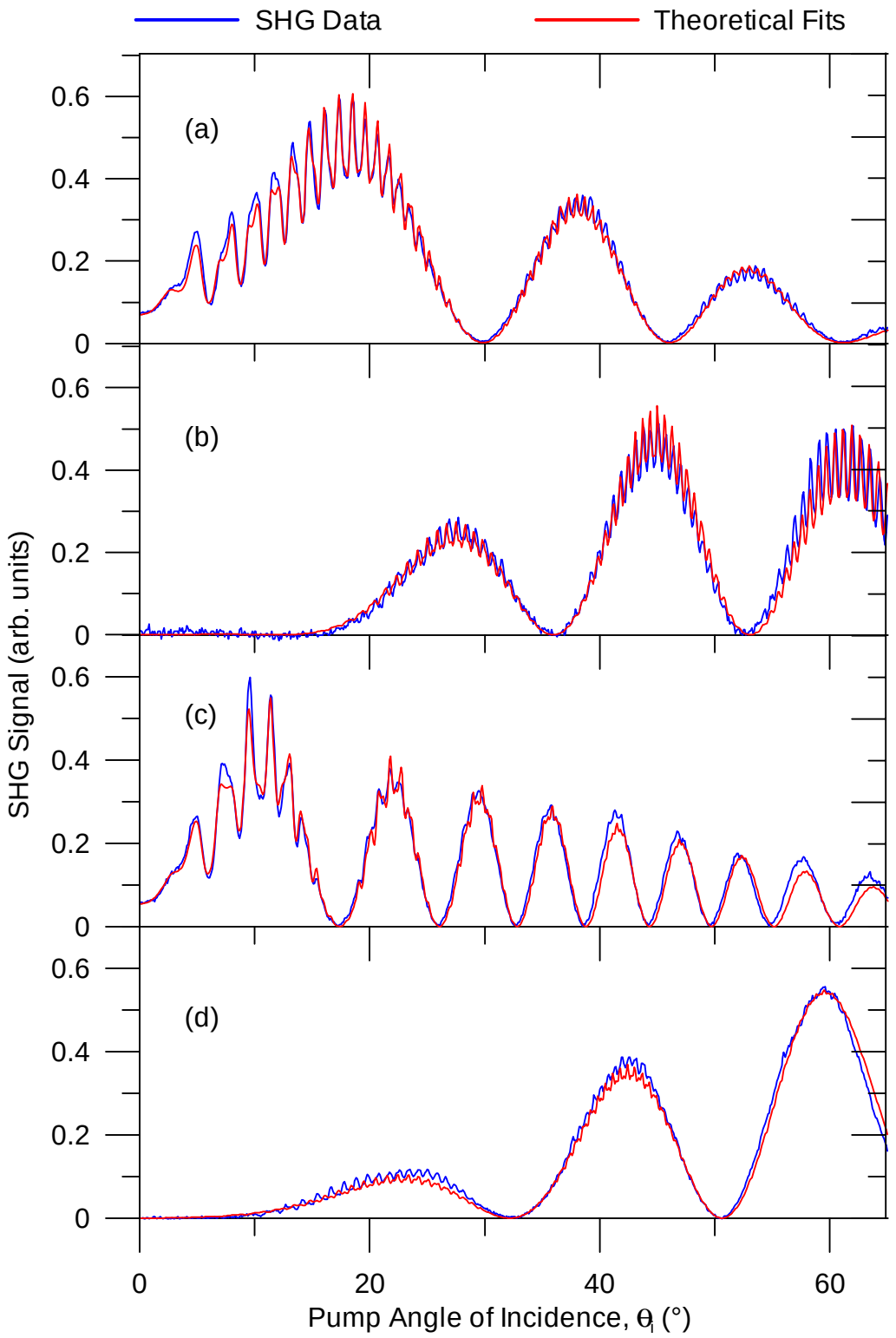

Figure 4.1 Comparison of Maker-fringe theory with data. All four pump-SHG cases solved individually (a) *o-o* case, (b) *o-e* case, (c) *e-o* case, (d) *e-e* case. Thickness values as given in Table 4.1.

"branch artifact." Branches occur when the arguments of the cosine terms in Equations (122), (127), (132), and (134) change by 2π. The main contributor to the distance between branches is the term containing the difference of the effective pump and SHG wave vectors. For the *e-e* case, branches in thickness will occur approximately every $L_{branch} = 2\pi/(K_{zep}-K_{zes})$. Calculated at $\theta_i = 0$ the value of L_{branch} is ~5.8 μm and is the same for the other 3 cases for $\theta_i = 0$.

Examining the least squared error as a function of sample thickness, Figure 4.2, reveals the oscillatory nature of the fitting parameter where local minima are separated by a branch step. When only one pump-SHG case is considered, it can be ambiguous as to which branch is the correct one. For any given data set, up to three different branch thicknesses may provide fitting parameters leading to acceptable theoretical fits to the data.

Measuring the distance between local minima from the least squared error data for each pump-SHG case results in the average branch step lengths found in Table 4.2.

Table 4.2 Measured average branch length for each pump-SHG case, Sample A.

Pump-SHG case	Measured L_{branch} (μm)
o-o	5.75
o-e	6.14
e-o	5.66
e-e	5.58

While these values are approximated by the value of L_{branch}, calculated above, each case has a different branch step size. This is due to the angular dependence of L_{branch} as well as the other cosine terms in Equations

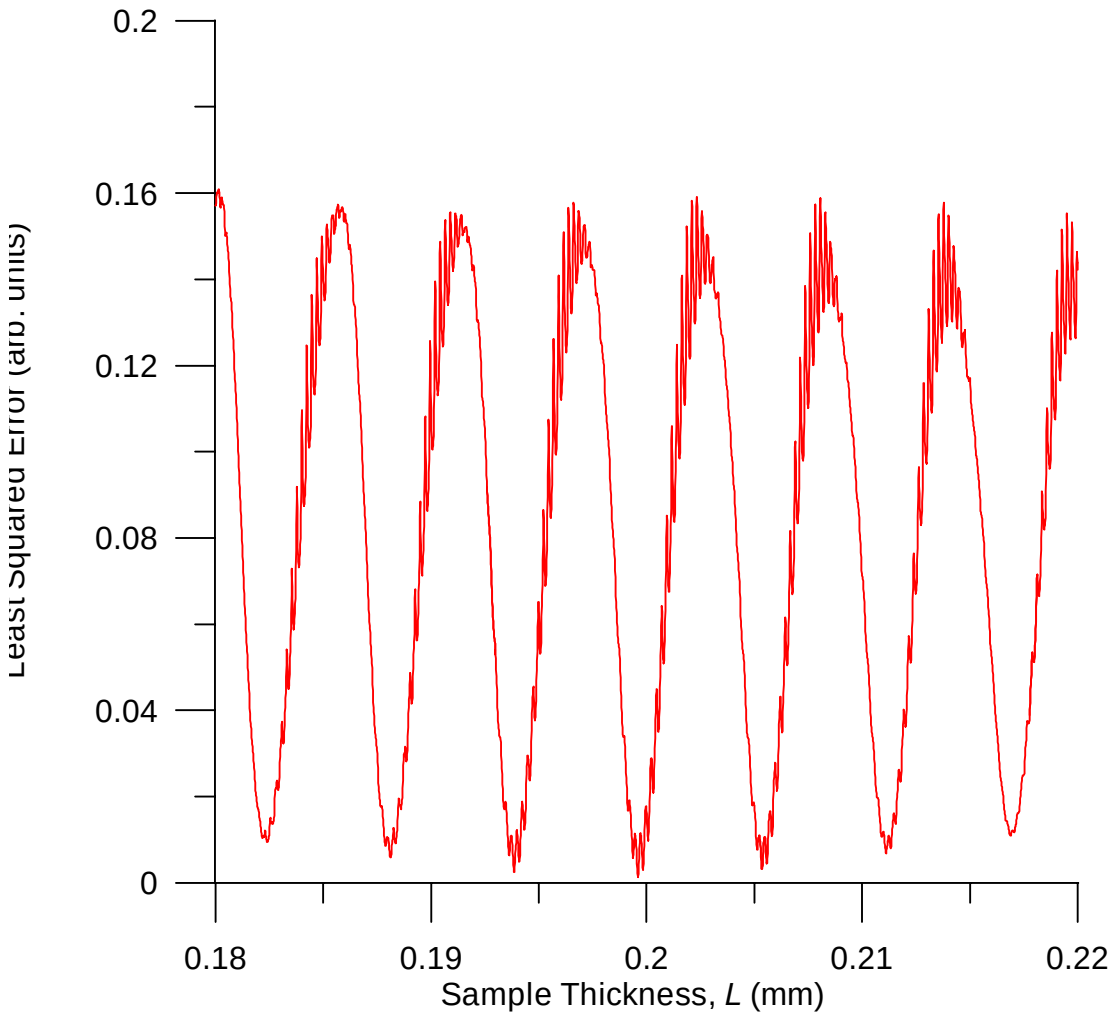

Figure 4.2 Least squared error obtained during thickness fit of the *o-o* theory to data.

(122), (127), (132), and (134) and can be used to eliminate the ambiguity in choosing the proper branch. When examining the LSE for all 4 cases simultaneously, it can be seen that there is only one thickness value where all cases have coincidental minima. In Figure 4.3 we see that this thickness occurs at ~0.1995 mm. Within this thickness branch, the *e-e* case has a LSE at a thickness of 0.19951 mm.

The next step in the analysis is to reconcile the small thickness deviations within the correct thickness branch. The first approximation is to run all four solvers simultaneously to obtain a consensus thickness. For the example data set given here, the consensus thickness is 0.19959 mm. Figure 4.4 shows the overlays of the theoretical fits for L = 0.19959 mm and the Maker fringe data. Again, the fits are quite reasonable, except for the matchup of the low frequency nulls at high angles of incidence for the *o-e* and *e-o* cases. Since the change in thickness between the fits in Figures 4.1 and 4.4 for the *o-o* and *e-o* cases is only 0.01 μm, the fits are very similar to one another. The only place where there is a distinguishable difference is in the 0° to 5° range.

To improve the fit, the parameter search range was expanded to include deviations from the indices predicted by the Sellmeier equations. The resolution of the index perturbations was 10^{-5}. Solving all 4 pump-SHG cases simultaneously for the five parameters L, Δn_{op}, Δn_{os}, Δn_{ep}, and Δn_{es} leads to a series of degenerate solutions, 8 of which are presented in Table 4.3. Within the range of degenerate solutions examined, there was no local

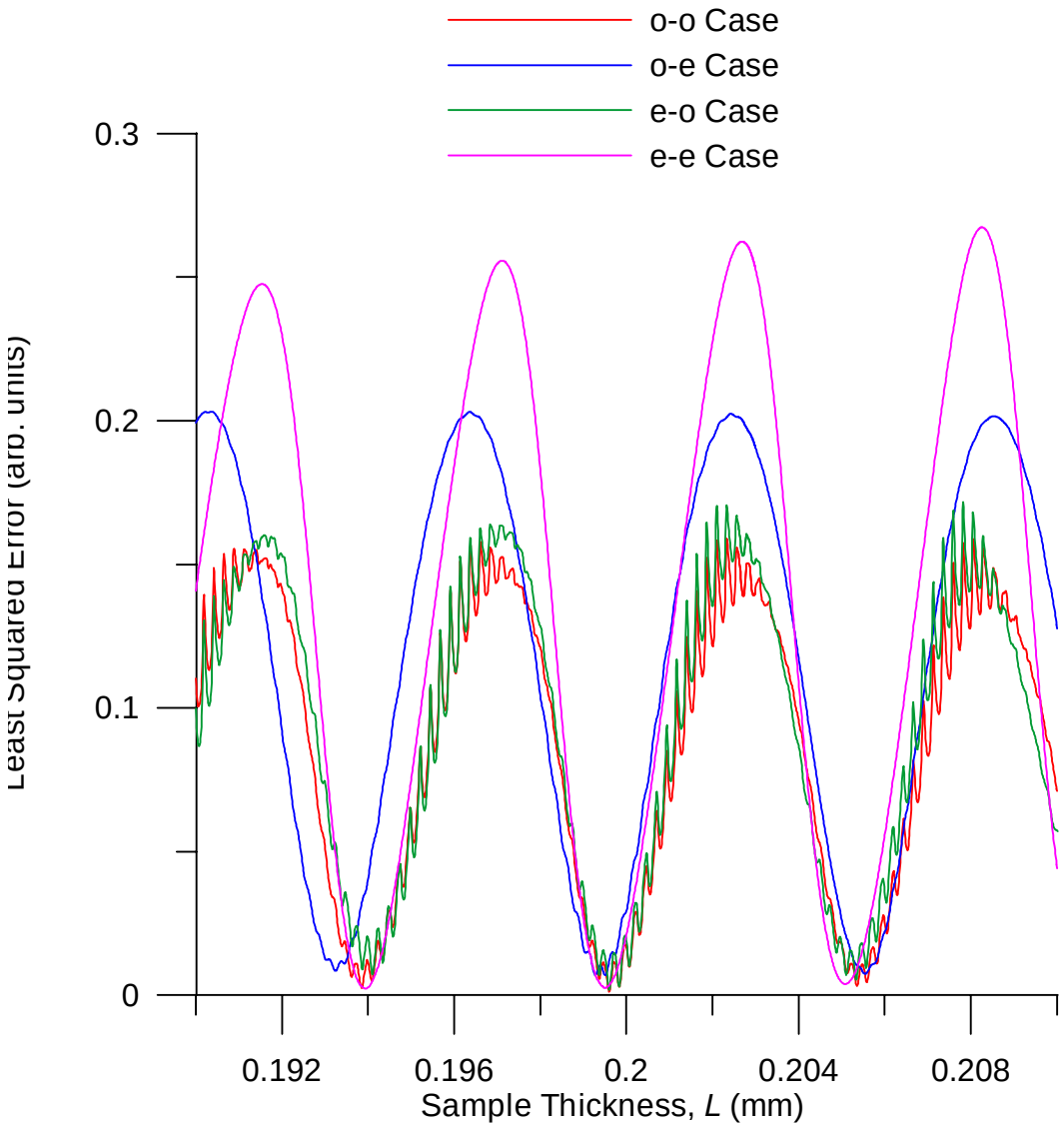

Figure 4.3 Comparison of the least squared error obtained during fits to thickness for each pump-SHG case. Each fit was performed separately.

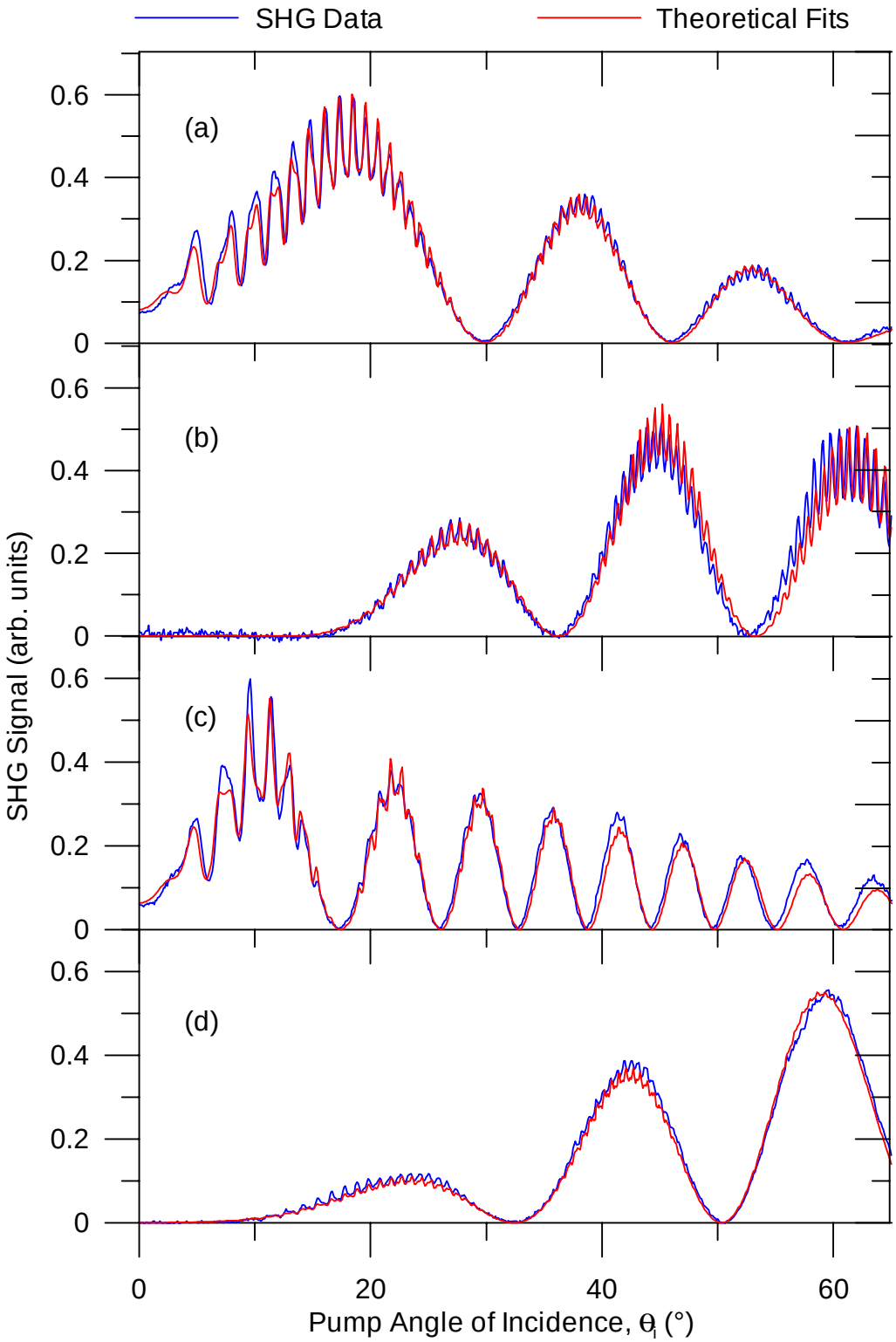

Figure 4.4 Comparison of data to theoretical fits. Fits to thickness were performed simultaneously for all four pump-SHG cases, (a) *o-o* case, (b) *o-e* case, (c) *e-o* case, (d) *e-e* case.

minimum encountered in the LSE. This is problematic and reveals the limitation of this experiment. An independent measurement of one of the five fitting parameters must be performed in order to define the proper parameter branch. The most logical candidate for independent measurement is the thickness, which would have to be measure to an accuracy of 5×10^{-5} to allow determination of the indices to within a few parts in 10^{-5}.

Table 4.3 Degenerate solutions obtained from simultaneous 4-case fit to L, Δn_{op}, Δn_{os}, Δn_{ep}, and Δn_{es} for Sample A.

L (mm)	Δn_{op} ($\times 10^{-4}$)	Δn_{os} ($\times 10^{-4}$)	Δn_{ep} ($\times 10^{-4}$)	Δn_{es} ($\times 10^{-4}$)	LSE ($\times 10^{-2}$)
0.19957	2.6	3.0	-3.1	-7.2	1.390
0.19958	1.5	1.8	-4.3	-8.0	1.373
0.19959	0.4	0.7	-5.1	-9.3	1.367
0.19960	-0.7	-0.5	-6.2	-10.0	1.360
0.19961	-1.8	-1.6	-7.1	-11.4	1.354
0.19962	-2.9	-2.8	-8.2	-12.1	1.348
0.19965	-6.3	-6.3	-11.2	-15.6	1.329
0.19970	-11.8	-12.0	-16.0	-21.1	1.296

In the absence of such a measurement, I will report a solution based on accepted index variations. The data in Table 4.3 show that as the thickness increases the various Δn's become increasingly negative and the least squared error improves. However, as the LSE improves the range of the Δn's becomes unacceptably large. I base this observation on the index-versus-composition data reported by Bergman *et al.* [Bergman '68] and the uncertainty associated with the Sellmeier equations. Bergman's work shows that the ordinary index of refraction has no detectable variation as a function of $LiNbO_3$ composition. Therefore, Δn_{op} and Δn_{os} should be within the uncertainty of the Sellmeier equation, $\pm 2 \times 10^{-4}$ [Edwards '84].

Reconciling these degeneracies by taking all the degenerate solutions that fall into the criteria of Δn_o being $\pm 2 \times 10^{-4}$ and averaging leads to a solution of $L = 0.199595 \pm 0.00002$ mm, $\Delta n_{op} = -0.15 \times 10^{-4} \pm 1.6 \times 10^{-4}$, $\Delta n_{os} = 0.1 \times 10^{-4} \pm 1.7 \times 10^{-4}$, $\Delta n_{ep} = -5.7 \times 10^{-4} \pm 1.4 \times 10^{-4}$, and $\Delta n_{es} = -9.7 \times 10^{-4} \pm 1.7 \times 10^{-4}$. The theoretical traces generated by each of these degenerate solutions are nearly indistinguishable from one another. For display, Figure 4.5 shows the overlays for the $L = 0.19960$ mm, $\Delta n_{op} = -0.7 \times 10^{-4}$, $\Delta n_{os} = -0.5 \times 10^{-4}$, $\Delta n_{ep} = -6.2 \times 10^{-4}$, and $\Delta n_{es} = -10.0 \times 10^{-4}$ degenerate solution with the data. These fits are the best that I have obtained for this data set. Both the high and low frequency fringes match for all 4 pump-SHG cases.

The most striking observation made from the solutions above is the offset of n_e needed to obtain the quality of fit seen in Figure 4.5. Similar shifts in n_e have been discussed by Shoji *et al.* [Shoji '97] and by Sanford and Aust [Sanford '98]. Shoji uses a Maker-fringe technique to measure the nonlinear coefficients of $LiNbO_3$. In doing so, he measures n_{es} by assuming that the ordinary index of Edwards and Lawrence [Edwards '84] is correct and fits his data by solving for n_{es}. For rotation about the *z*-axis, he reports a $\Delta n_{es} = -10.7 \times 10^{-4}$ and for rotation about the *x*-axis he reports $\Delta n_{es} = -10.2 \times 10^{-4}$. Shoji gives no explanation for this deviation. Sanford and I have seen similar shifts of n_{es} in sequenced *x*-cut wafers of $LiNbO_3$ [Sanford TBP]. Our preliminary analysis shows that the top of the boule, the portion grown first, has a Δn_{es} on the order of -5×10^{-4}, while the value of Δn_{es} at the bottom of the boule is on

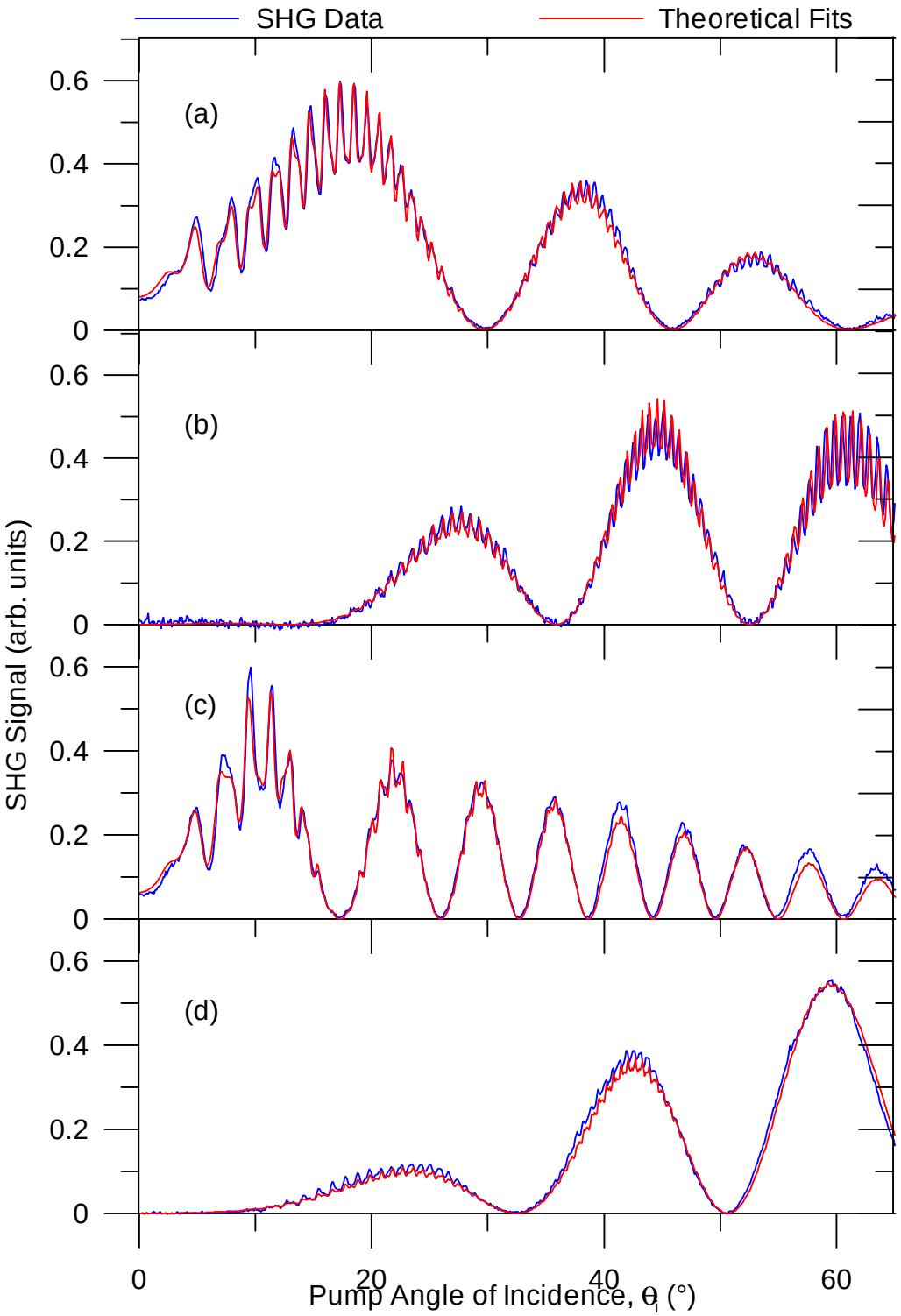

Figure 4.5 Comparison of theoretical fits with data. These fits were obtained by doing a simultaneous 4-case fit to L, Δn_{op}, Δn_{os}, Δn_{ep}, Δn_{es}. The values used for this display are $L = 0.19960$, $\Delta n_{op} = -0.7 \times 10^{-4}$, $\Delta n_{os} = -0.5 \times 10^{-4}$, $\Delta n_{ep} = -6.2 \times 10^{-4}$, $\Delta n_{es} = -10.0 \times 10^{-4}$. (a) *o*-*o* case, (b) *o*-*e* case, (c) *e*-*o* case, and (d) *e*-*e* case.

the order of -7×10^{-4}. The clear trend of decreasing n_{es} is indicative of increasing Li_2O content with boule length.

The original index data are stated to have an accuracy of $\pm 2 \times 10^{-4}$ [Nelson '74]. This seems to hold true for the values of n_o but not for the values for n_e. I believe the reason for this is the composition dependence of the extraordinary index of refraction. While Bergman's results show that n_o has no detectable variation with composition his n_e data vary considerably as a function of composition [Bergman '68]. However, because Bergman's data are presented as a function of melt composition instead of crystal composition, a conversion must be performed before a usable value for the change in n_e as a function of crystal composition can be obtained. I have accomplished this using the melt-to-crystal composition data reported by Carruthers *et al* [Carruthers '71]. Figure 4.6 shows Bergman's n_e data as a function of crystal composition in terms of its Li_2O mole percentage. A value for $\Delta n_e/\Delta$mol% of -0.0112 mol%$^{-1}$ is obtained by fitting a line to this data.

If the composition of the $LiNbO_3$ used for the index study that led to the Sellmeier equations was Li depleted by 0.09 mol% Li_2O, compared to the material used here, then the large Δn_e can be explained by this composition difference. In an attempt to confirm or refute such a possibility, I investigated the primary source of the index data used in the determination of the Sellmeier equations [Nelson '74]. Nelson and Mikulyak state that the material used in their index-of-refraction study is of congruent composition, which at the time was considered to be 48.6 mol% Li_2O. Their phase-matching

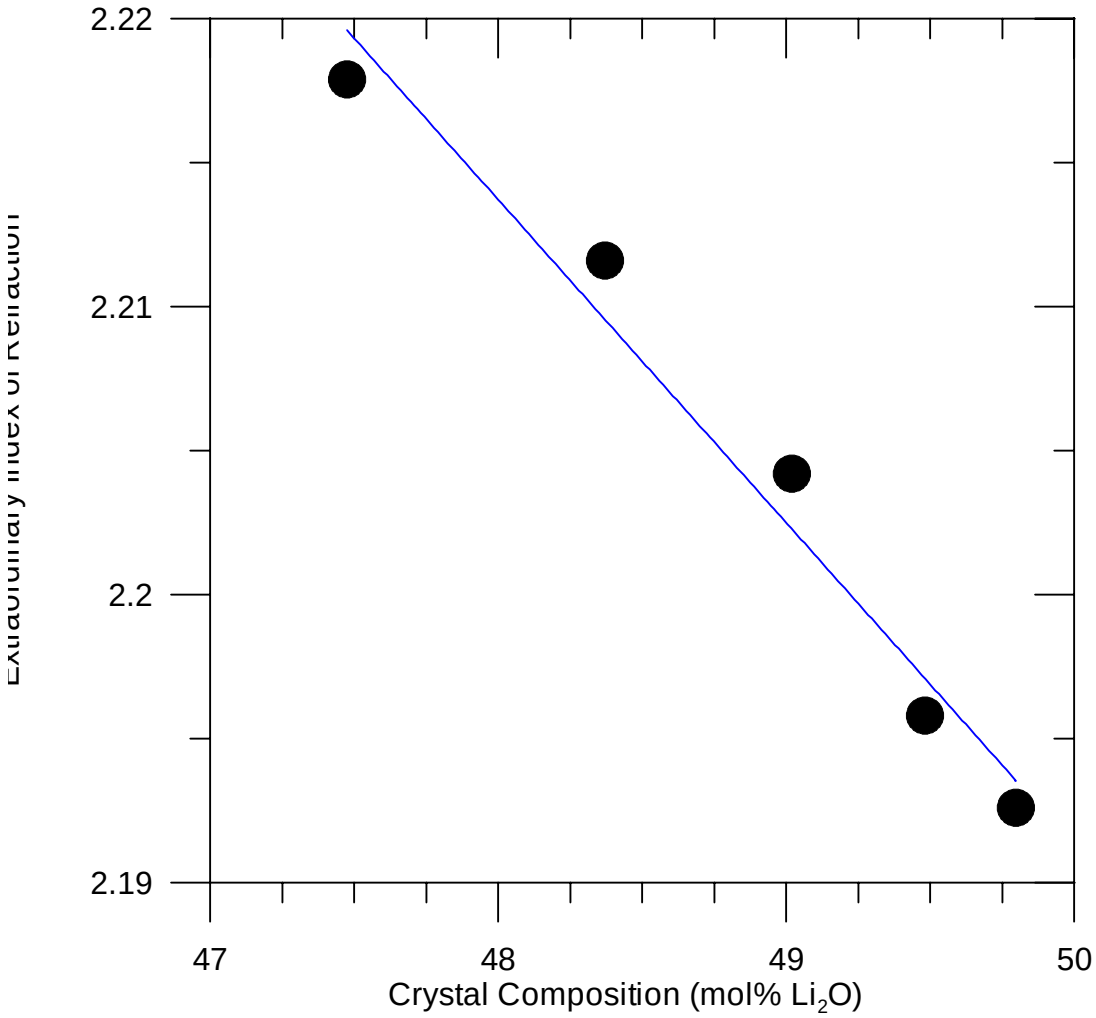

Figure 4.6 Bergman's index data re-cast as a function of crystal composition (black circles). Linear fit to data, blue line.

temperature T_{pm} at 1.1523 μm was reported to be 174 ºC. They further stated that this agreed favorably with the data of Byer *et al.* [Byer '70], who reported T_{pm} for 1.15 μm at 172 ºC. Byer *et al.* also report the phase matching temperature at 1.064 μm and 1.084 μm but do not mention their material's composition, other than its being congruent. A crosscorrelation between Byer's data and that reported by Bordui *et al.* [Bordui '92] for T_{pm} at 1.064 μm can be used to infer the composition of Nelson's material. Bordui reports T_{pm} as a function of crystal composition. His data show a linear relationship over the composition range studied, 47 to 49.5 mol% LiO_2. I believe the composition studies performed by Bordui *et al* are the most comprehensive to date and reflect the most accurate compositional data. Correlating Byer's T_{pm} data to Bordui's T_{pm} vs composition data suggests that Byer's and therefore Nelson's composition is closer to 48.3 mol% Li_2O, not the 48.6 mol% LiO_2 reported.

If this is in fact the case then my $-9.7 \times 10^{-4} \pm 1.7 \times 10^{-4}$ variation from the predicted Sellmeier index for n_{es} suggests that the composition of the material used here differed from that used in Nelson's study by 0.09 ± 0.02 mol% Li_2O or had a composition of 48.39 ± 0.02 mol% Li_2O. This coincides well with the value currently regarded as congruent, 48.38 ± 0.015 mol% Li_2O [Bordui '91].

Additional sources for the deviation of the extraordinary index are due to static surface charge on the sample and the location from within the boule from which the material was cut. The effect of charge on the surface will be

examined later. The $LiNbO_3$ data sheet from Crystal Technology, Inc. [Crystal '93] shows that the composition may vary up to ± 0.01 mol% Li_2O from the top to the bottom of the boule depending on the starting composition and other growth conditions. Also Bordui's paper [Bordui '91] states that the start composition can only be determined to ± 0.01 mol% Li_2O. These uncertainties in composition add a further uncertainty of $\pm 2.2 \times 10^{-4}$ in the value of n_e.

Additional samples, from a second supplier, have also been studied. Sample B was nominally 0.25 mm thick and Sample C was nominally 1.0 mm thick. The Maker fringe data for both of these samples are displayed in Figure 4.7. Note the increased number of low frequency fringes as the sample thickness increases. This is due to the fact that the path length change as a function of pump incidence angle is faster for thicker samples. The Maker fringe fitting parameters for Sample B were found using the same procedure as described above. These parameters are shown in Table 4.4.

Table 4.4 Degenerated solutions obtained from simultaneous 4-case fit to L, Δn_{op}, Δn_{os}, Δn_{ep}, and Δn_{es} for Sample B.

L_o (mm)	Δn_{op} ($\times 10^{-4}$)	Δn_{os} ($\times 10^{-4}$)	Δn_{ep} ($\times 10^{-4}$)	Δn_{es} ($\times 10^{-4}$)	LSE ($\times 10^{-2}$)
0.23913	2.0	2.7	-4.7	-5.9	2.427
0.23914	1.1	1.7	-5.6	-6.5	2.436
0.23915	0.2	0.8	-6.3	-7.5	2.441
0.23916	-0.8	-0.2	-7.1	-8.6	2.448
0.23917	-1.7	-1.2	-8.0	-9.2	2.455
0.23918	-2.6	-2.1	-8.7	-10.2	2.460

Averaging all the solutions that fall into the criteria of $\Delta n_o = \pm 2 \times 10^{-4}$ results in $L_o = 0.239155 \pm 0.00002$ mm, $\Delta n_{op} = -0.3 \times 10^{-4} \pm 1.4 \times 10^{-4}$, $\Delta n_{os} = 0.3 \times 10^{-4} \pm 1.4 \times 10^{-4}$, $\Delta n_{ep} = -6.8 \times 10^{-4} \pm 1.2 \times 10^{-4}$, and $\Delta n_{es} = -8.0 \times 10^{-4} \pm 1.4 \times 10^{-4}$.

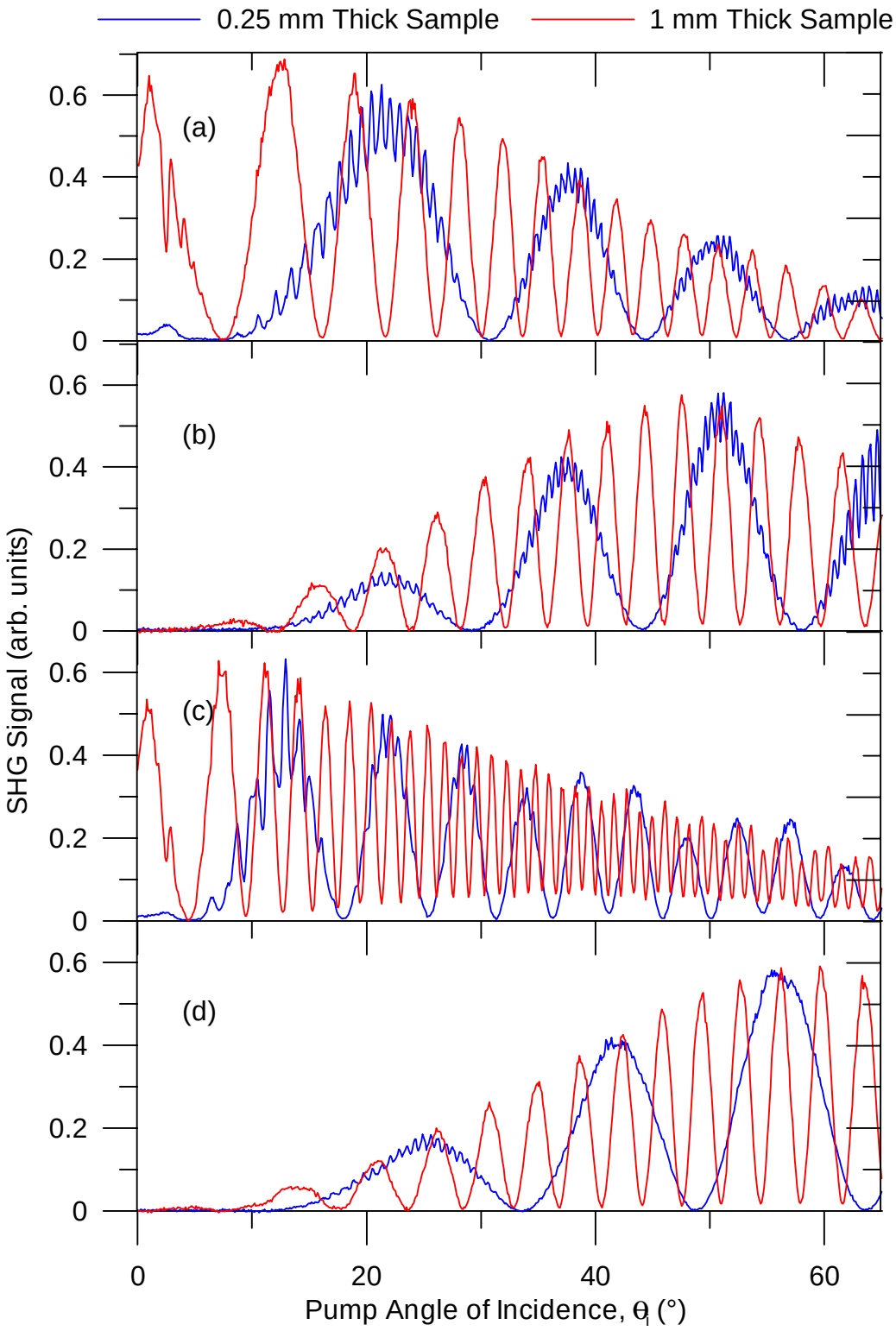

Figure 4.7 Maker-fringe data for Sample B, ~0.25 mm thick, and Sample C ~1.0 mm thick. (a) *o-o* case, (b) *o-e* case, (c) *e-o* case, (d) *e-e* case.

Sample C proved to be very difficult to fit. The Maker fringes occur much faster with respect to pump angle of incidence for thicker samples. As a result, the high frequency fringes are, for the most part, unresolved in the data. For this reason the single-pass Maker fringe code was used to solve for the fit parameters for these data. The data also suffer from an apparent acquisition anomaly. The nulls of the low frequency fringes ride up off the baseline on what looks like a lower envelope. This phenomenon is most noticeable for the *e*-*o* case but is present to some degree for all the cases. Attempts to eliminate this behavior by slowing the sample rotation speed and increasing the angular resolution of the data acquisition to 0.02º failed to eliminate this behavior. Attempts to solve for the fitting parameters for this data set, using the procedure described above, have failed. While performing 5 parameter fits (*L* and all 4 Δn's) or 4 parameter fits (holding *L* constant and solving for all Δn's) the fitting parameters walkoff and never converge to a solution that is fully contained in the search range. That is, at least one of the fitting parameters would converge to a limit in its search range. This biases the other parameters' solutions and leads to unacceptable results.

Comparing the results for samples A and B shows agreement to within the uncertainty stated. This suggests that the two suppliers are growing material of similar composition.

4.2 Nonlinear Coefficient Fit

Maker fringe analysis can be used as a tool to determine other properties of $LiNbO_3$ as well. In particular the nonlinear coefficients and the electrooptic coefficients can be determined given suitable experimental procedures. For determining the absolute nonlinear coefficients, the power of all SHG outputs must be known. One way to achieve this is to take all the data, as well as the signal from a reference material such as crystalline quartz, on the same PMT with the same gain settings and the same pump power. In this way the relative powers of the different SHG signals allow for determining the ratios of the nonlinear coefficients, while comparing to the reference material's SHG signal fixes the test sample's absolute nonlinear coefficient values.

The data considered here were taken on two different PMT-box car averager setups and for two different pump powers. Direct comparison of the signal from one PMT to the other will not result in accurate values for the nonlinear coefficients. From the data that were taken, however, I can determine the ratio of $d_{33}^{(2)}/d_{31}^{(2)}$ by examining the *e*-*e* Maker fringe signal. Equations (115a) and (115b) show that the *e*-*e* case is a function of $d_{15}^{(2)}$, $d_{31}^{(2)}$, and $d_{33}^{(2)}$. From Kleinman's dispersion arguments we know that $d_{15}^{(2)} = d_{31}^{(2)}$ [Kleinman '62]. Changing the ratio $d_{33}^{(2)}/d_{31}^{(2)}$ changes the shape of the

envelope of the *e-e* Maker fringe signal. Therefore, the ratio of $d_{33}^{(2)}/d_{31}^{(2)}$ can found by fitting the envelope of the *e-e* Maker fringe theory to data.

Published values for $d_{31}^{(2)}$ range from 4.6 × 10^{-11} to 5.95 × 10^{-11} pm/V and for $d_{33}^{(2)}$ from 25.2 × 10^{-11} to 34.4 × 10^{-11} pm/V [Dmitriev '91, Kurtz '79, Shoji '97]. These values translate into a $d_{33}^{(2)}/d_{31}^{(2)}$ range from 4.2 to 7.5. Figure 4.8 shows fits for 4 different $d_{33}^{(2)}/d_{31}^{(2)}$ ratios in this range along with data. The value of $d_{33}^{(2)}/d_{31}^{(2)}$ of 4.2 fits the amplitude of the data best. This suggests that $d_{33}^{(2)}$ is on the low side of its range and $d_{31}^{(2)}$ is on the high side of its range. Thus the suggested values based on this work are $d_{33}^{(2)}$ = 25.2 pm/V and $d_{31}^{(2)}$ = 5.95 pm/V.

4.3 Electric Field Perturbations to Maker Fringe Signals

As mentioned above, the presence of an electric field on the surface of the sample will cause a perturbation in the Maker fringe signals. This is due to two separate phenomena: the electrooptic effect and the converse piezoelectric effect. The electrooptic effect will affect the indices of refraction of the material while the converse piezoelectric effect will cause a thickness change in the sample. Since I am considering only DC electric fields, the unclamped or constant stress electrooptic coefficient r_{ij}^{T} must be used. r_{ij}^{T} is

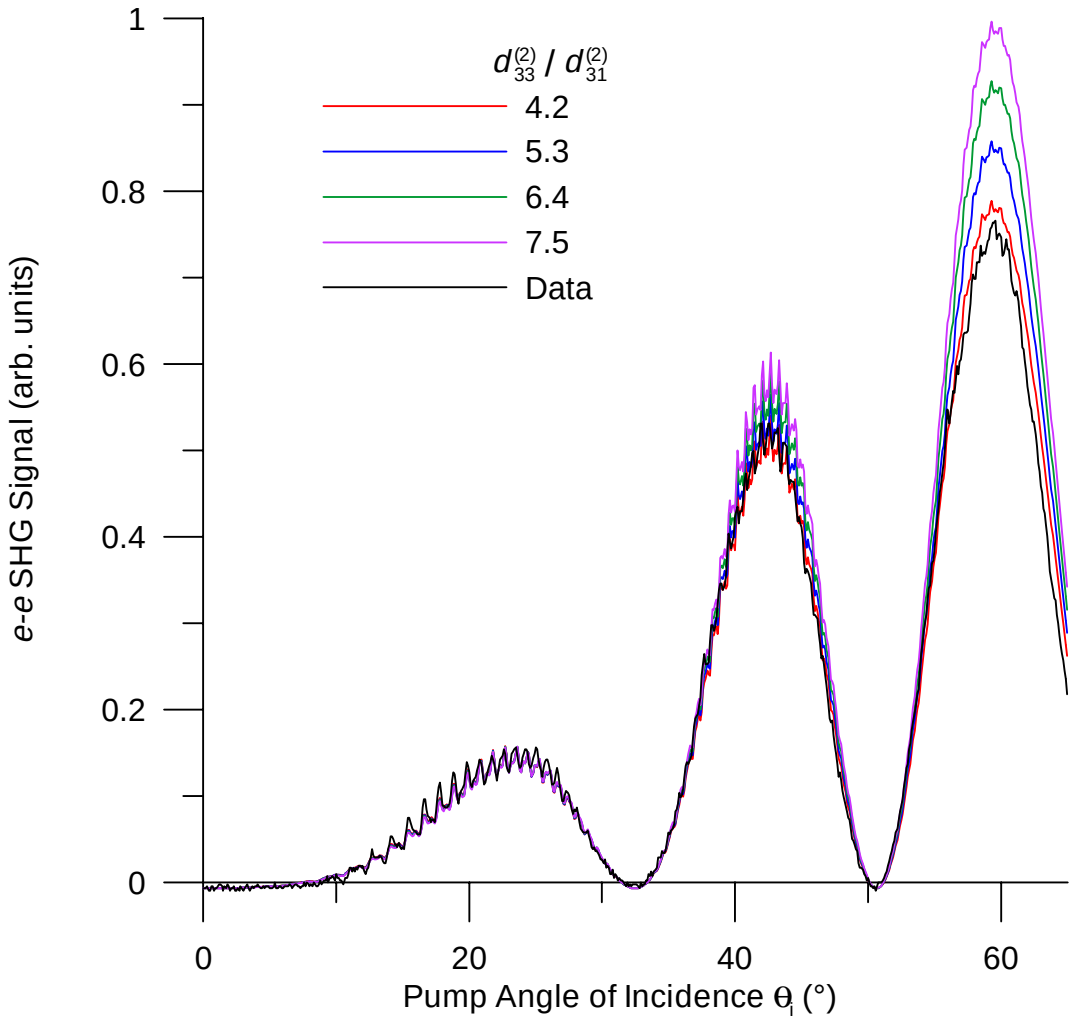

Figure 4.8 Comparison of different $d_{33}^{(2)}$ / $d_{31}^{(2)}$ ratios for the *e-e* Maker-fringe case.

related to the clamped or constant strain electrooptic coefficient r_{ij}^{S} by

$$r_{ij}^{T} = r_{ij}^{S} + p_{ik} d_{jk}, \tag{136}$$

where p_{ik} is the photoelastic coefficient and d_{jk} is the piezoelectric coefficient (not to be confused with the nonlinear susceptibility $d_{jk}^{(2)}$). If the field is in the *z*-direction only, the indices of refraction will be changed according to

$$\Delta n_o = -\frac{n_o^3}{2} r_{13}^{T} E_3, \tag{137a}$$

$$\Delta n_e = -\frac{n_e^3}{2} r_{33}^{T} E_3. \tag{137b}$$

The sample's thickness change is given by

$$\Delta L = L\, d_{33}\, E_3, \tag{138}$$

where L is the sample thickness.

To demonstrate the magnitude of these changes, an electric field of 1 kV/mm present on the *z*-surface of the sample will give rise to the following changes $\Delta n_{op} = -0.4 \times 10^{-4}$, $\Delta n_{os} = -0.6 \times 10^{-4}$, $\Delta n_{ep} = -1.6 \times 10^{-4}$, $\Delta n_{es} = -1.8 \times 10^{-4}$, and $\Delta L = 0.001$ μm. The dispersion of the electrooptic coefficients was considered when calculating these values. Interpreting the electrooptic coefficient-versus-wavelength data presented by Mendez *et al* resulted in the following coefficients $r_{13,p}^{T} = 0.8 \times 10^{-5}$ mm/kV, $r_{13,s}^{T} = 1.0 \times 10^{-5}$ mm/kV, $r_{33,p}^{T} = 3.1 \times 10^{-5}$ mm/kV, $r_{33,s}^{T} = 3.2 \times 10^{-5}$ mm/kV, where the subscript *p* designates the pump wavelength and the subscript *s* designates the second-harmonic wavelength [Mendez '99]. For the length change calculation I used $d_{33} = 0.6 \times$

10^{-11} C/N and L = 0.2 mm. These calculations show that the electrooptic effect should be clearly resolved by our Maker fringe analysis while the converse piezoelectric effect should be negligible for electric fields up to 10 kV/mm.

$LiNbO_3$ is a pyroelectric material and generates a surface charge whenever the material experiences a change in temperature. As the temperature of the sample changes, the spontaneous polarization changes according to

$$\Delta P_s = \zeta \cdot \Delta T \tag{139}$$

where $\zeta = -4 \times 10^{-5}$ C/(K•m^2). Associated with this change in polarization is it a change in the depolarizing field ΔE_{dep}. The depolarizing field is eventually compensated for by the migration of free charge, from either the environment or the material itself, to the surface of the sample. Pyroelectric detectors work by measuring the charge flow to the sample's surface to compensate for the temperature-induced change in the spontaneous polarization. When the depolarization field is fully compensated for, the sample experiences no net electric field. Figure 4.9 (a) represents a $LiNbO_3$ sample that is fully compensated for the depolarizing field generated by the sample's spontaneous polarization. Before the compensation is complete, the sample experiences a net electric field E_{net} equal to the uncompensated depolarizing field. Figures 4.9 (b)-(d) show a sequence of pictures representing the polarization and electric field changes associated with a temperature change and accompanying charge compensation. The first of these pictures

(a) Fully Compensated Sample

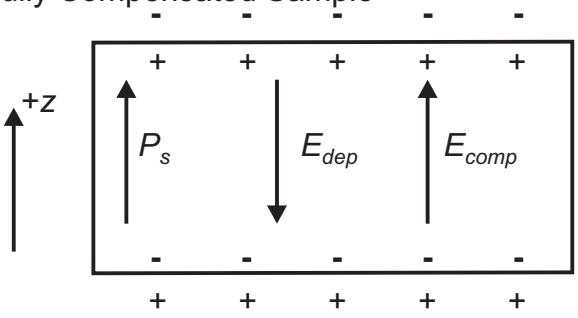

$E_{Net} = 0 = E_{dep} + E_{sur}$

(b) -ΔT with No Charge Compensation

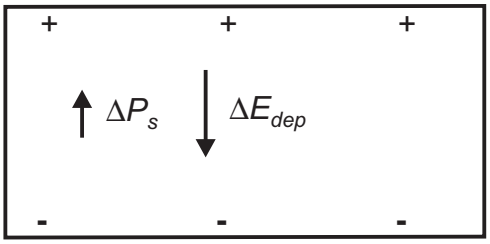

$E_{Net} = \Delta E_{dep}$

(c) -ΔT with Partial Charge Compensation

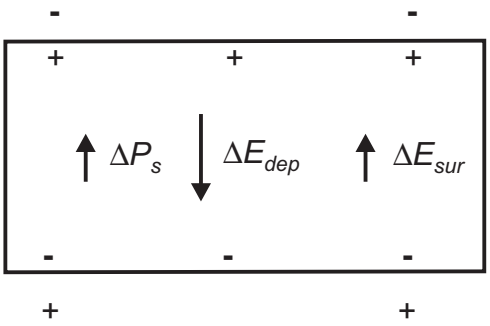

$E_{Net} = \Delta E_{dep} + \Delta E_{sur}$

(d) -ΔT with Full Charge Compensation

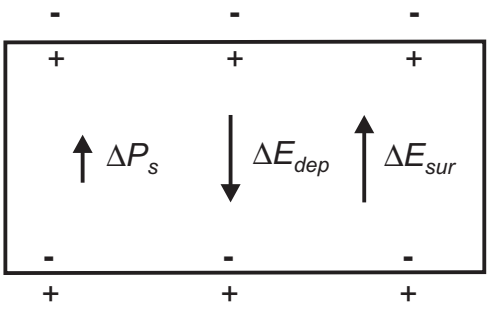

$E_{Net} = 0 = \Delta E_{dep} + \Delta E_{sur}$

Figure 4.9 Schematic of depolarizing fields and associated compensating surface charges.

shows a sample in the hypothetical situation of having experienced a decrease in temperature and no charge compensation. The second represents partial depolarizing field compensation and the last full compensation. The effect of this ΔT-induced net electric field on the material can be simulated by the effect of an applied electric field that produces the same net electric field. From classic dielectric theory (see for example [Serway '83]) we know that $E_{net} = E_o + E_1$ where E_o is the applied electric field, E_1 is the field associated with the material's response to the E_o and is the electric-field-induced depolarizing field, and E_{net} is the net field experienced by the material. Expressing the net electric field in terms of only the applied field results in $E_{net} = E_o/\varepsilon_{33}$ where ε_{33} is the dielectric constant and has a value of 29.1 [Crystal Technology, Inc. '1993]. Therefore, a ΔT-induced net electric field will result in the same electrooptic index changes to the material as an applied electric field of $E_o = \varepsilon_{33}E_{net}$.

The ΔT-induced depolarizing field relates to opposing the change in the spontaneous polarization and not necessarily opposing the spontaneous polarization itself. Positive temperature changes create a reduction in P_s but the associated depolarizing field is directed to increase P_s. Negative temperature changes increase P_s, but result in a depolarizing field that opposes P_s. For large negative ΔT's, the depolarizing field can become large enough to overcome the coercive field of the material, ~21 kV/mm, and cause self domain reversal. For temperature changes in either direction of ~100 °C

over a time of a few minutes, electrical discharge from the sample has routinely been observed.

An example of what can occur when a *z*-cut wafer of $LiNbO_3$ is temperature-cycled is illustrated in Figures 4.10 and 4.11. Figure 4.10 (a) represents the typical appearance of an as-received wafer viewed through a microscope with a 5x objective and through crossed polarizers. The sample was then temperature-cycled on a hot plate from 25 ºC to 120 ºC in roughly 30 min and allowed to dwell at 120 ºC for 5 min. The sample was then removed from the hot plate and allowed to cool back to room temperature over a period of ~20 min. During the cooling, electrical discharges were observed. Figure 4.10 (b) depicts the typical appearance of the sample after this temperature cycle. Two types of features are visible, defects with 3-fold symmetry, commensurate with the C_{3v} point group symmetry of $LiNbO_3$, and "wispy clouds." The sample was placed in a low vacuum in an attempt to charge compensate it. This technique was suggested by Dieter Jundt of Crystal Technology, Inc. Almost immediately after the mechanical pump was turned on, more electrical discharges were observed. By the time the pressure reached 0.5 Torr the discharging had stopped. No further discharging was seen on the vent cycle or on a subsequent vacuum cycle. The picture in Figure 4.10 (c) shows that the defects of 3-fold symmetry remain but that the "wispy clouds" have been eliminated. I believe that the "wispy cloud" observation was due to a non-uniform uncompensated depolarization field in the sample after the temperature cycle. The nonuniform

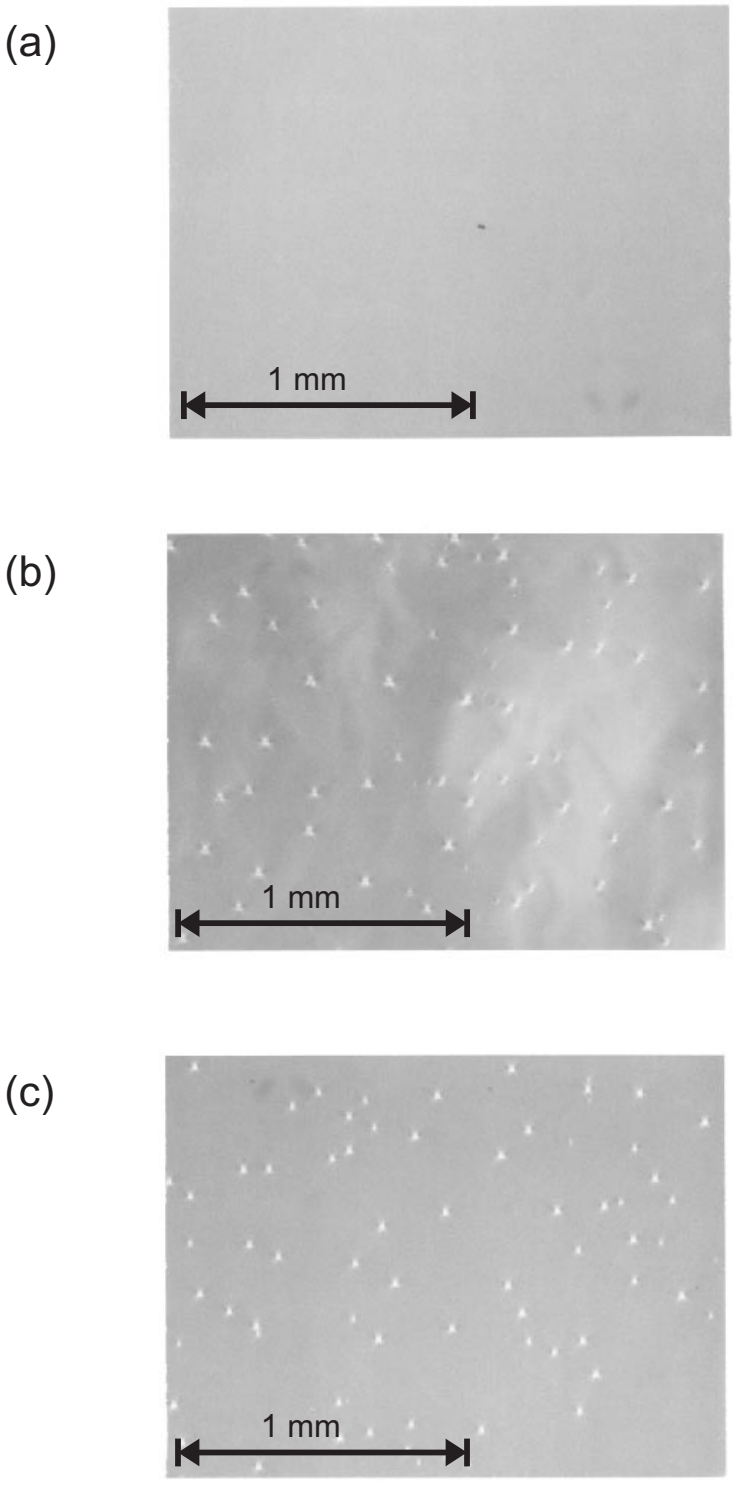

Figure 4.10 Photographs of a $LiNbO_3$ wafer taken using a 5x objective. (a) as-recieved sample, (b) after a 200 °C anneal, (c) after charge compensation.

uniform field caused a spatially varying index change, localized birefringence between $n_{o,x}$ and $n_{o,y}$, that caused a variable polarization rotation and allowed light to leak through the crossed polarizers. After the sample was fully discharged, the effect was eliminated.

Examining the 3-fold symmetry defects more closely revealed that they were in fact small domain reversed regions. Figures 4.11 (a) and (b) show 50x views of the same region of the sample for before and after etching. Once again the pictures were taken through crossed polarizers. It is well know that the positive and negative *z*-faces of $LiNbO_3$ differentially etch in a solution of HNO_3 and HF with the negative *z*-face etching faster. I used a 2:1 ratio of HNO_3 to HF and etched the sample for 35 min at room temperature. The result of the etch was a one-to-one correlation of etch features to 3-fold symmetry defects. Etch features consist of hillocks on the negative *z*-face and etch pits on the positive *z*-face. This confirms that these defects are domain-reversed regions but does not explain their visibility when viewed between crossed polarizers. I believe the distortion of the microscope illumination in the vicinity of these defects is due to space charge separation in the region of the domain walls. This would again create localized index changes, which give rise to a birefringence between $n_{o,x}$ and $n_{o,y}$ at the domain walls, thereby allowing the light to leak through the crossed polarizers.

The effect of pyroelectrically induced surface potentials on the *o*-*o* Maker fringe signal is displayed in Figure 4.12. The different scans in the

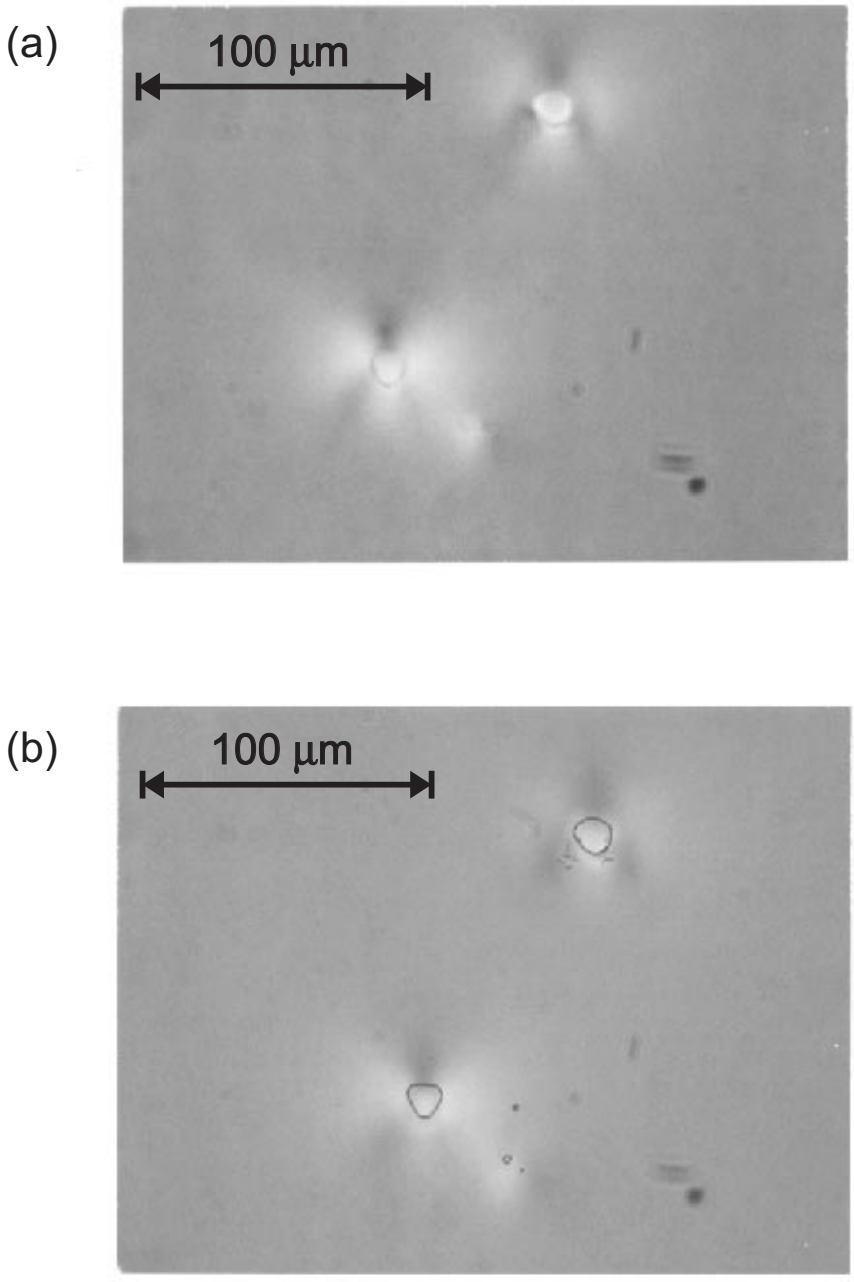

Figure 4.11 Photographs of 3-fold defects taken through crossed polarizers with a 50x objective. (a) before etching and (b) after etching.

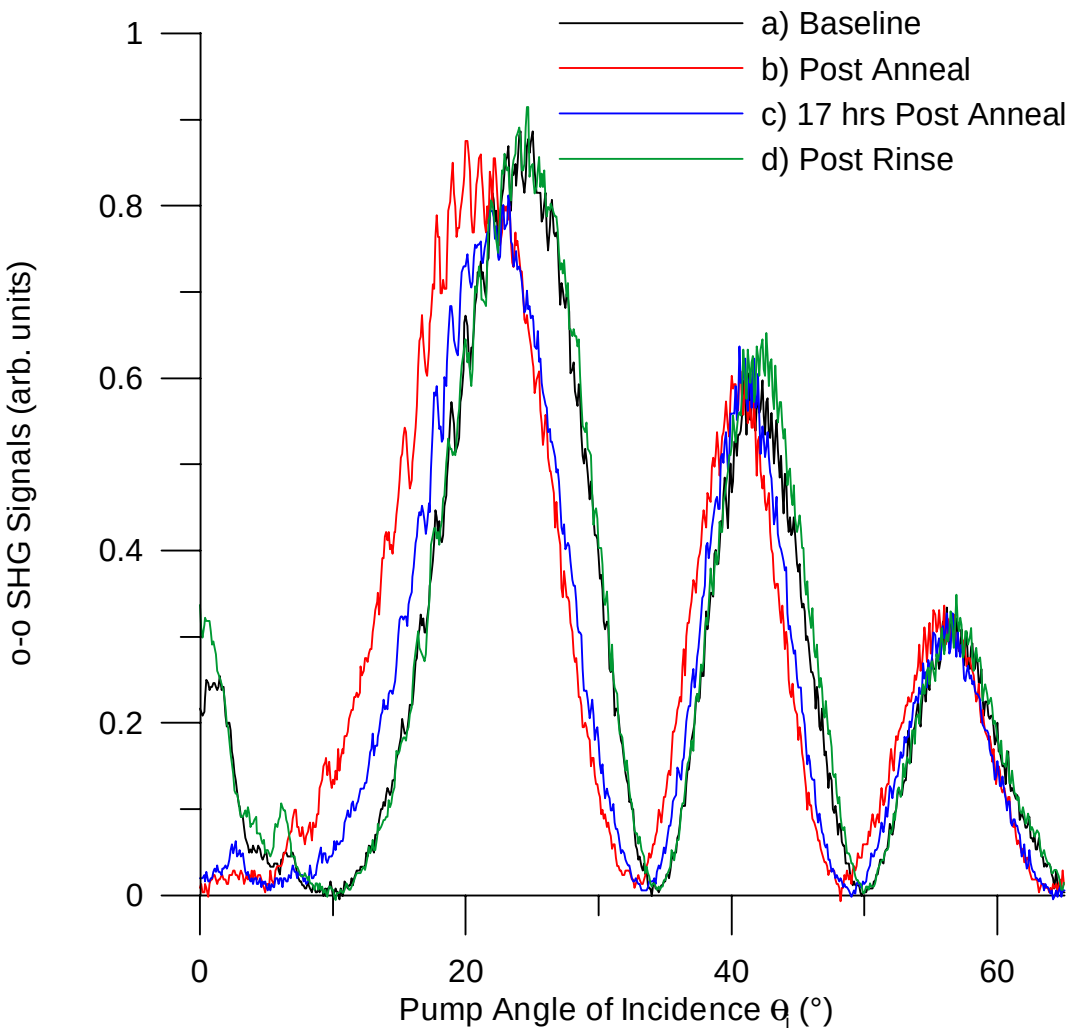

Figure 4.12 Progession of the *o-o* Maker-finge signal as a result of pyroelectricity.

figure correspond to (a) data taken before any processing, (b) immediately after returning to room temperature following a 10 min anneal at 200 ºC, (c) 17 h after the anneal, and (d) after being rinsed in tap water. These data were taken on the earlier Maker-fringe setup that used a cw pump laser and lock-in detection. Vissual inspection of these traces shows that the fringe shift immediately following the anneal is significant, ~4°; some recovery is seen after 17 h, and full recovery has occurred after the sample was rinsed in tap water.

Using the data from trace (a) as a baseline for the Maker-fringe analysis results in a sample thickness of 0.19808 mm and index variations from the Sellmeier values of $\Delta n_{op} = -0.3 \times 10^{-4}$ and $\Delta n_{os} = 0.0$. Using these parameters as inputs and solving for an apparent applied electric field E_{app} for the data in trace (b) results in E_{app} = -19.1 kV/mm, for trace (c) E_{app} = -11.7 kV/mm, and for trace (d) E_{app} = 1.0 kV/mm. The overlays of all four of these fits are shown in Figure 4.13. These values suggest that the non-neutralized depolarization field due to the original temperature cycle for traces (b) and (c) are -0.66 and -0.40 kV/mm respectively. The 1.0 kV/mm apparent applied field (0.03 kV/mm uncompensated depolarization field) found for trace (d) is most likely due to a positive ΔT as the sample warmed from the temperature of the tap water back up to room temperature.

In an attempt to eliminate the effect of depolarization fields on the Maker fringe signals and to measure the values of r_{13}^{T} and r_{33}^{T}, a series of experiments were devised using transparent electrodes on the *z*-surfaces of

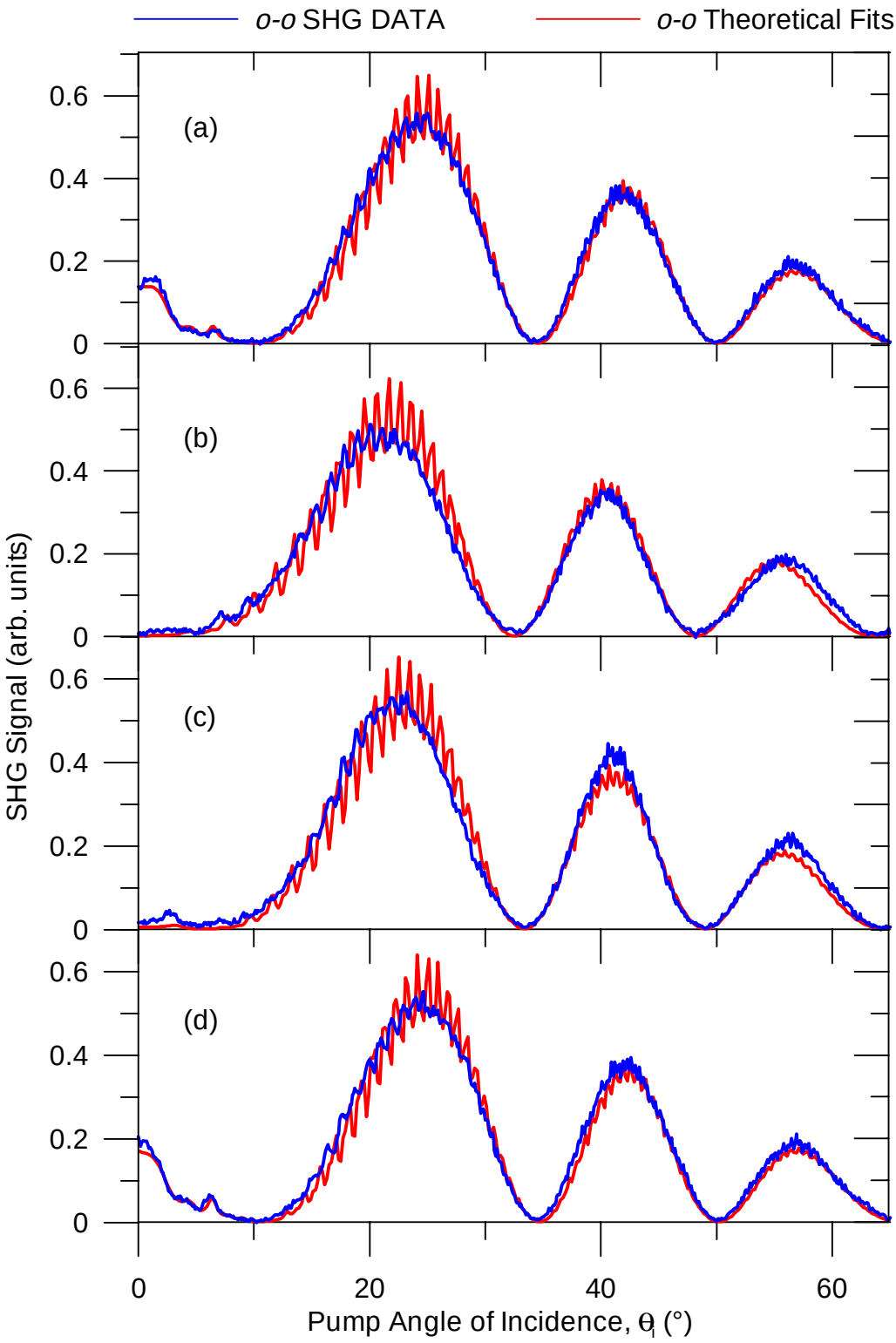

Figure 4.13 Theoretical fits to the *o-o* Maker-fringe signals shown in Figure 4.12. (a) baseline data, E_{app} = 0.0 kV/mm, (b) post-anneal data, E_{app} = -19.1 kV/mm, (c) 17 h post-anneal data, E_{app} = -11.7 kV/mm, (d) post-charge compensation by rising in water, E_{app} = +1.0 kV/mm.

the sample. The electrodes were constructed in the following manner. A pad of Al 100 nm thick and approximately 4 mm × 8 mm was deposited onto each *z*-face of the sample. An electrical lead was bonded to a portion of each pad using electrically conducting epoxy. Next a drop of LiCl in water solution was sandwiched between the sample and a quartz cover slip. The cover slips were positioned to overlap a portion of the Al pads. A schematic of these electrodes is shown in Figure 4.14. The leads were then used to apply a known electric field to the region of the sample covered by the quartz cover slips while taking Maker fringe data.

Data was taken for Sample A with an open circuit condition and on Sample D for a short circuit condition (0 kV/mm) and for ±5 kV/mm applied fields. The open circuit condition was examined to see what type of perturbation the electrodes themselves caused to the Maker fringe signals. Figure 4.15 compares the *o*-*o* Maker fringe signal with and without the surface electrodes. The result was somewhat disappointing. Because the electrodes reduced the index contrast at the sample's surfaces, the high frequency fringes where greatly affected. Most notable was the reduction in the high frequency fringe amplitude. This effect on the Maker fringe signals can be accounted for in the theory by changing the boundary conditions at the sample's surfaces to include the index of refraction of the liquid electrodes. I have not yet done so, so the analysis of these data uses the current full resonance code using the overlap factors described in Equation (136).

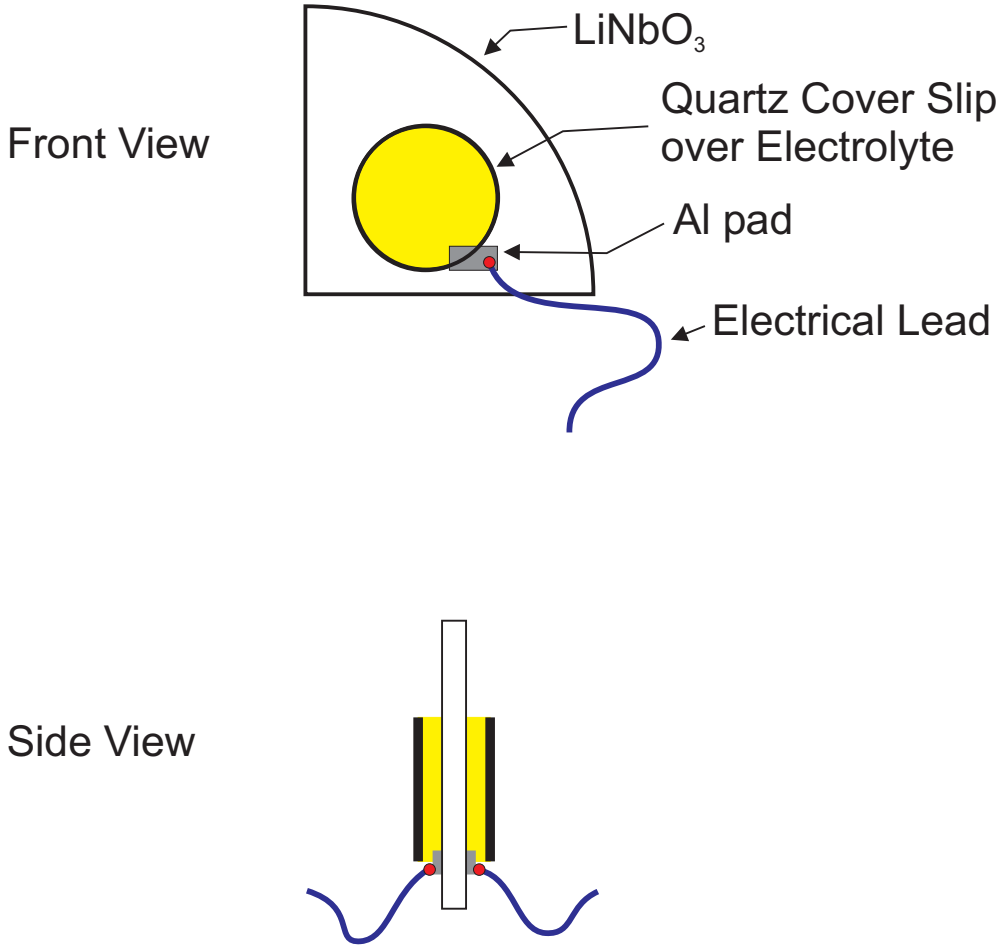

Figure 4.14 Schematic of liquid electrodes.

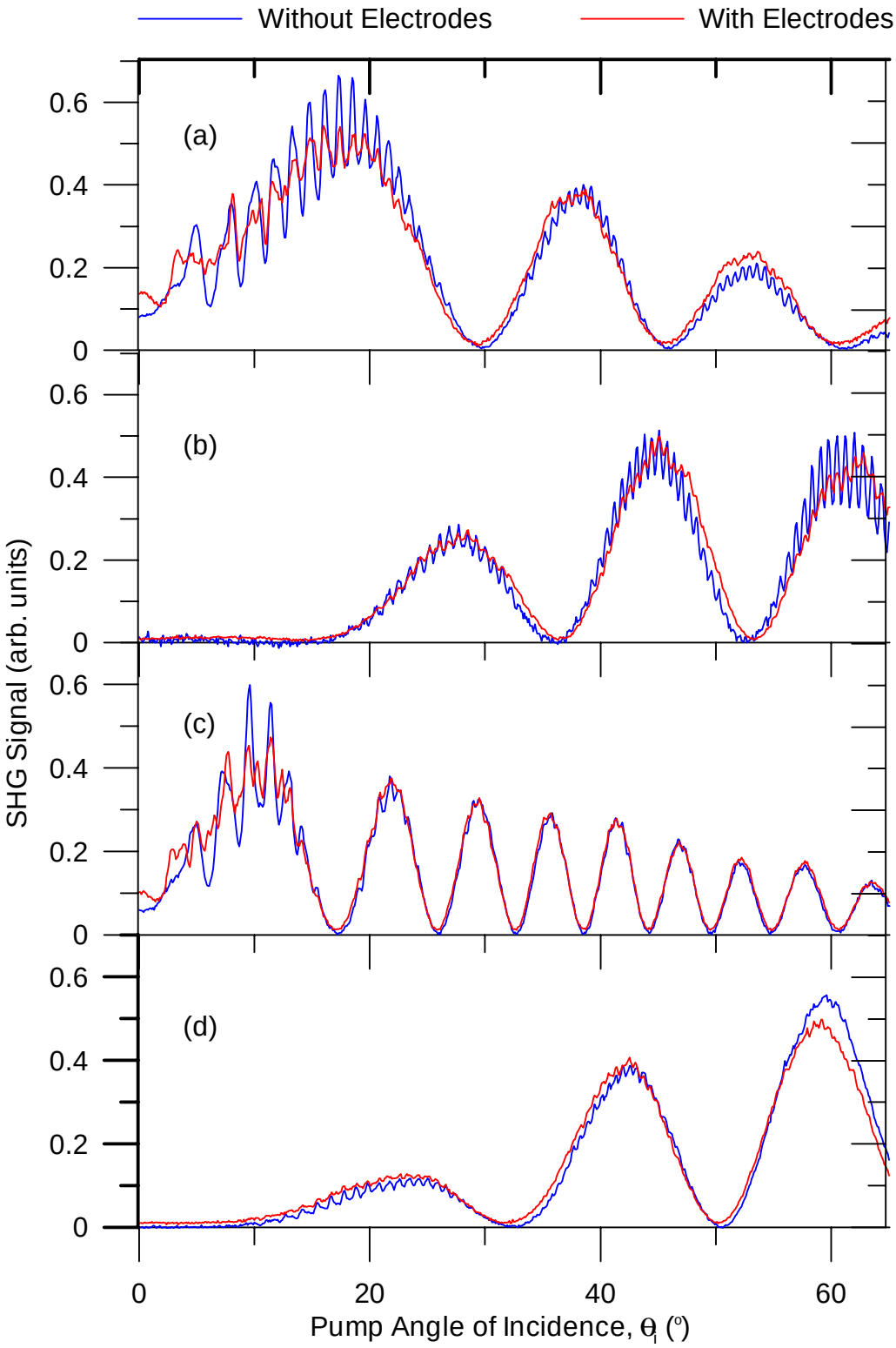

Figure 4.15 Comparison of Maker-fringe signals for with and without liquid electrodes. (a) o-o case, (b) o-e case, (c) e-o case, and (d) e-e case.

Analyzing the Make-fringe data taken at the same location as that found in Table 4.3 but with the liquid electrodes in place shows how the degenerate parameter sets have shifted. These results are presented in Table 4.5.

Table 4.5 Degenerate solutions obtained from simultaneous 4-case fit to L, Δn_{op}, Δn_{os}, Δn_{ep}, and Δn_{es} for Sample A with liquid electrodes.

L (mm)	Δn_{op} ($\times 10^{-4}$)	Δn_{os} ($\times 10^{-4}$)	Δn_{ep} ($\times 10^{-4}$)	Δn_{es} ($\times 10^{-4}$)	LSE ($\times 10^{-2}$)
0.19958	1.7	2.3	1.2	-5.0	1.255
0.19959	0.6	1.2	0.3	-6.4	1.253
0.19960	-0.5	0.0	-0.8	-7.1	1.251
0.19961	-1.6	-1.1	-1.6	-8.4	1.248
0.19962	-2.7	-2.3	-2.7	-9.1	1.246

The average of the degenerate solutions that have Δn_o's in the range of $\pm 2 \times 10^{-4}$ is $L = 0.19960 \pm 0.00001$, $\Delta n_{op} = -0.5 \times 10^{-4} \pm 1.1 \times 10^{-4}$, $\Delta n_{os} = 0.0 \pm 1.1 \times 10^{-4}$, $\Delta n_{ep} = -0.7 \times 10^{-4} \pm 1.0 \times 10^{-4}$, $\Delta n_{es} = -7.3 \times 10^{-4} \pm 1.0 \times 10^{-4}$. The thickness, Δn_{op}, and Δn_{os} fall within the range determined from the data without the electrodes; however, Δn_{ep} and Δn_{es} have shifted significantly from the nonelectrode results. Looking at the individual degenerate solutions shows even greater discrepancy of the Δn's between the data taken with and without the electrodes. These discrepancies are most likely due to some combination of the electrodes' perturbation of the Maker fringe signals and a redistribution of the surface charge due to the electrodes establishing a constant potential on each surface.

Nontheless, I have used the liquid electrode technique to explore the values of the linear electrooptic coefficients. Identical electrodes to those

described above were fabricated on a similar sub-wafer of $LiNbO_3$, Sample D. Figure 4.16 shows the progression of the Maker fringe signal as a function of applied electric field. The data taken with shorted electrodes (E_o = 0 kV/mm) were used to determine the baseline parameters L, Δn_{op}, Δn_{os}, Δn_{ep}, and Δn_{es} for this sample. The degenerate solutions for this baseline data set were solved for as described above and are presented in Table 4.6.

Table 4.6 Degenerate solutions obtained from simultaneous 4-case fit to L, Δn_{op}, Δn_{os}, Δn_{ep}, and Δn_{es} for Sample D with Eo = 0 kV/mm.

Ref. #	L (mm)	Δn_{op} ($\times 10^{-4}$)	Δn_{os} ($\times 10^{-4}$)	Δn_{ep} ($\times 10^{-4}$)	Δn_{es} ($\times 10^{-4}$)
1	0.20223	1.4	1.8	-3.9	-5.0
2	0.20224	0.3	0.7	-4.8	-6.3
3	0.20225	-0.7	-0.4	-5.8	-6.9
4	0.20226	-1.9	-1.6	-6.8	-8.4

These values were then used as inputs for solving the data sets taken for ±5 kV/mm applied fields.

The Maker-fringe scans taken for the ±5 kV/mm applied fields were analyzed in two different ways. First, as a self-consistency check, they were analyzed by solving for the applied field using the previously stated published values for the electrooptic coefficients. Then the actual applied field was used as an input and the four electrooptic coefficients were found. In the self-consistency check the -5.0 kV/mm data yielded an electric field of -5.2, -5.1, -5.1, and -5.1 kV/mm for the four degenerate solutions in Table 4.6. The +5.0 kV/mm data solved to 5.0, 5.1, 5.0, and 5.0 kV/mm. The 5.0 kV/mm data were very self-consistent while the -5.0 kV/mm were less self-consistent.

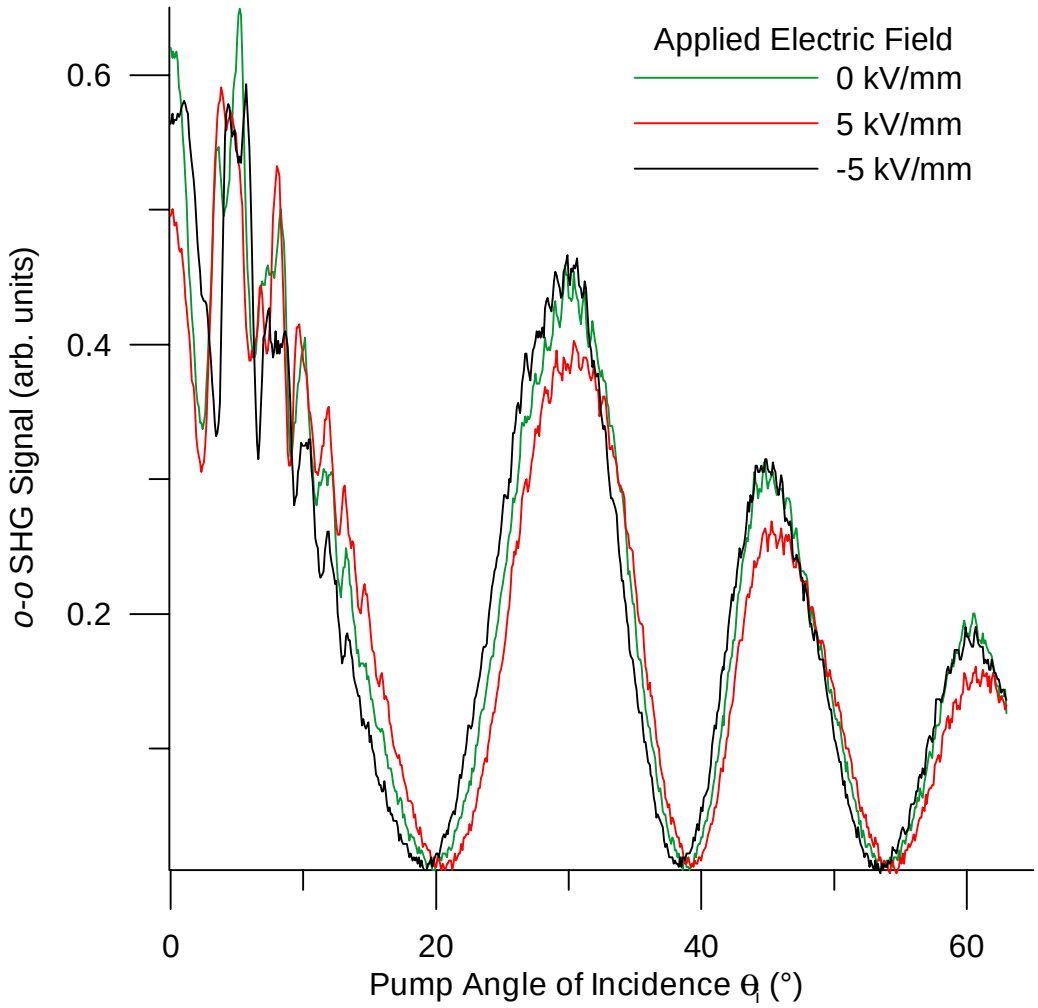

Figure 4.16 Comparison of *o-o* Maker-fringe signal for different applied fields.

The coefficients found from the second part of this experiment appear in Table 4.7.

Table 4.7 Electrooptic coefficients found

E_o (kV/mm)	Degenerate Ref #	$r^T_{13,p} \times 10^{-5}$ (mm/kV)	$r^T_{13,s} \times 10^{-5}$ (mm/kV)	$r^T_{33,p} \times 10^{-5}$ (mm/kV)	$r^T_{33,s} \times 10^{-5}$ (mm/kV)
-5.0	1	1.28	1.41	3.47	3.37
-5.0	2	1.28	1.39	3.42	3.49
-5.0	3	1.25	1.38	3.43	3.34
-5.0	4	1.28	1.39	3.43	3.51
5.0	1	1.03	1.12	3.11	3.46
5.0	2	1.04	1.14	3.14	3.40
5.0	3	1.08	1.16	3.11	3.52
5.0	4	1.04	1.14	3.13	3.38

These values are mostly higher than those normally seen in the literature and stated earlier in this section. There is a clear clustering of the results dependent upon the applied field. For E_o = -5.0 kV/mm the average electrooptic coefficients were $r^T_{13,p} = 1.27 \times 10^{-5}$ mm/kV, $r^T_{13,s} = 1.39 \times 10^{-5}$ mm/kV, $r^T_{33,p} = 3.44 \times 10^{-5}$ mm/kV, and $r^T_{33,s} = 3.43 \times 10^{-5}$ mm/kV. For E_o = 5.0 kV/mm the average electrooptic coefficients were $r^T_{13,p} = 1.05 \times 10^{-5}$ mm/kV, $r^T_{13,s} = 1.14 \times 10^{-5}$ mm/kV, $r^T_{33,p} = 3.12 \times 10^{-5}$ mm/kV, and $r^T_{33,s} = 3.44 \times 10^{-5}$ mm/kV.

The reasons for this clustering and the elevated values for these electrooptic coefficients are unknown. Implementation of solving codes using the proper boundary conditions for the liquid electrodes and having an independent measurement of the sample's thickness may help resolve these issues.

4.4 Maker-Fringe Analysis of Domain Reversed Lithium Niobate

Using Maker-fringe analysis as a tool to examine domain-reversed $LiNbO_3$ was a natural extension for this technique. However, no difference between the Maker-fringe signals from originally domained material and domain-reversed material should be expected unless a domain wall is encountered. The domain reversal process involves realigning the direction of the spontaneous polarization only and is not thought to affect the indices, thickness, nonlinear coefficients, or depolarizing field response with respect to the direction of the P_s of the sample.

Preliminary tests of this hypothesis proved it to be incorrect; there was a clear shift between the Maker fringe signals taken before and after poling. Determining the possible cause of the shift in the Maker fringe signals, the conditions required to eliminate the shift, if any, and the magnitude of the shift are the goals of this section.

Maker-fringe scans were taken at four different stages throughout the process history of Sample Q. The four stages were before processing, after electric field poling, after annealing, and after discharging the sample. At each of these stages Maker fringe scans were taken over the same 5.0 mm by 5.0 mm region of the sample. The spacing between scans was 0.25 mm in both the *x*- and *y*-directions. The 0.2 mm thick sample was 15 × 15 mm. For this series of experiments only *o*-polarized pump data were taken. This was because the data were taken very early in the research and at that time I was

not considering *e*-polarized pumping. Having only *o*-polarized pump data cuts the number of pump-SHG cases to be solved in half but only reduces the number of fitting parameters to be found by one, because Δn_{ep} is no longer included.

The first set of Maker-fringe scans, those taken before any processing, were used to establish a baseline set of fitting parameters that will be used and compared to those for subsequent scans. Because of the nature of the pyroelectric effect, the initial state of the sample is very difficult to judge. Without knowing exactly the sample's thickness and uncompensated depolarization field, I cannot precisely determine the indices of refraction of the material in the initial state. Using the *o*-*o* and *o*-*e* data taken for grid point 1, I initially assumed that the sample was fully charge compensated and solved for thickness, Δn_{op}, Δn_{os}, and Δn_{es} simultaneously. The degenerate solution I chose for these data was L = 0.20504 mm, $\Delta n_{op} = -0.1 \times 10^{-4}$, $\Delta n_{os} = 0.2 \times 10^{-4}$, $\Delta n_{es} = -7.6 \times 10^{-4}$. Next I assume that there is no variation in the indices of refraction as a function of position and use these indices as inputs while calculating the thickness and apparent electric field for the remaining grid points. By making this assumption, any variation in the indices will be incorporated into the variation in L and E_{app}. The contour map in Figure 4.17 (a) represents the thickness values for a 1.5 mm × 5.0 mm region of this data set and shows a clear trend of increasing thickness from the lower left corner to the upper right corner. The maximum thickness excursion over this area is 0.35 μm. A map of corresponding electric field is shown in Figure 4.17

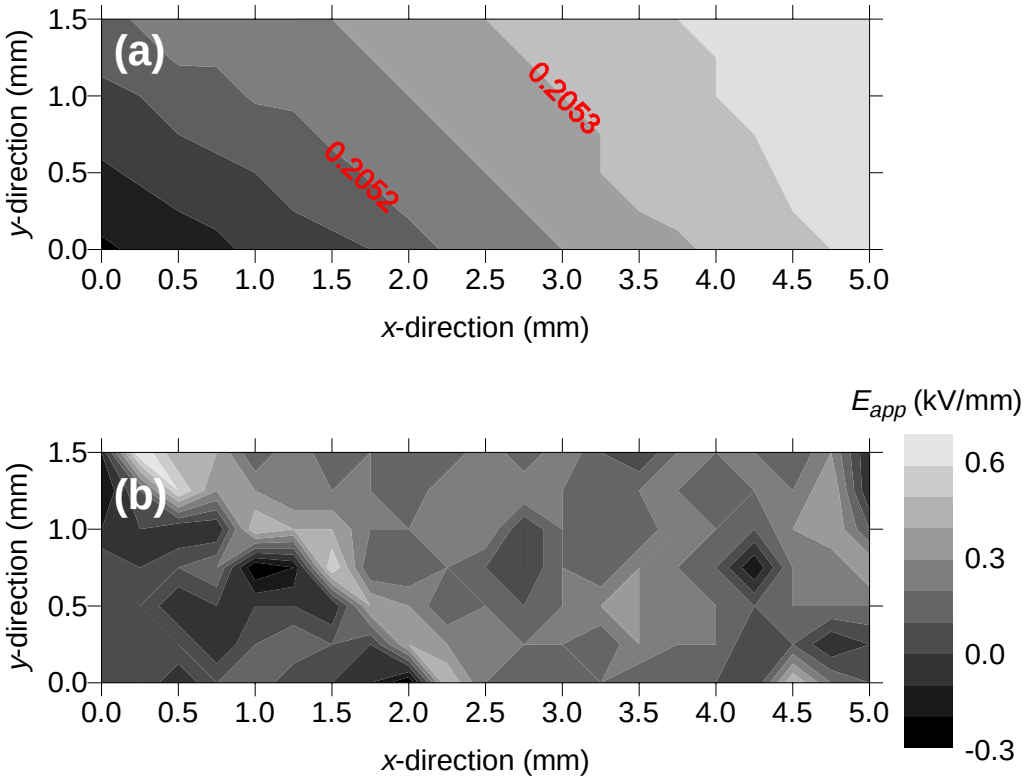

Figure 4.17 Baseline wafer maps of (a) thickness (mm) and (b) apparent electric field E_{app} *(kV/mm).*

(b) and shows no correlation with the thickness trend. The average electric field is 0.15 kV/mm with values ranging from –0.3 to 0.7 kV/mm. These data represent our baseline information for the sample. We will compare the electric field data with those obtained after each of the processing steps.

The next set of scans was taken after a portion of the sample had been poled to the opposite domain direction. The poled feature was delineated by photoresist and consisted of a square 0.76 mm on a side. The domain reversal was accomplished by applying a single 5.2 kV, 1 ms pulse to the sample. See Section 3.2 for a description of the poling setup. The effect of the poling process on the Maker-fringe scans is detailed in Figure 4.18. Here Maker-fringe scans were taken from locations inside and outside the poled region for before and after the domain reversal. The scans in Figure 4.18 (a) show how the signals changed inside the poled region while Figure 4.18 (b) is shown as a control to see how the signals outside the poled region changed. Figure 4.18 (a) shows that the low frequency fringes are shifted toward normal incidence and there is an offset in amplitude for the high frequency fringes near normal incidence. Figure 4.18 (b) shows that the low and high frequency fringes outside the poled region occur nearly on top of one another with a slight shift of the low frequency fringes toward high angles of incidence. Qualitatively these data suggest that the material and/or the electric field conditions outside the poled region have changed very little, whereas inside the poled region the change was larger and in the opposite direction. A quantitative measure of these changes was made by fitting the apparent

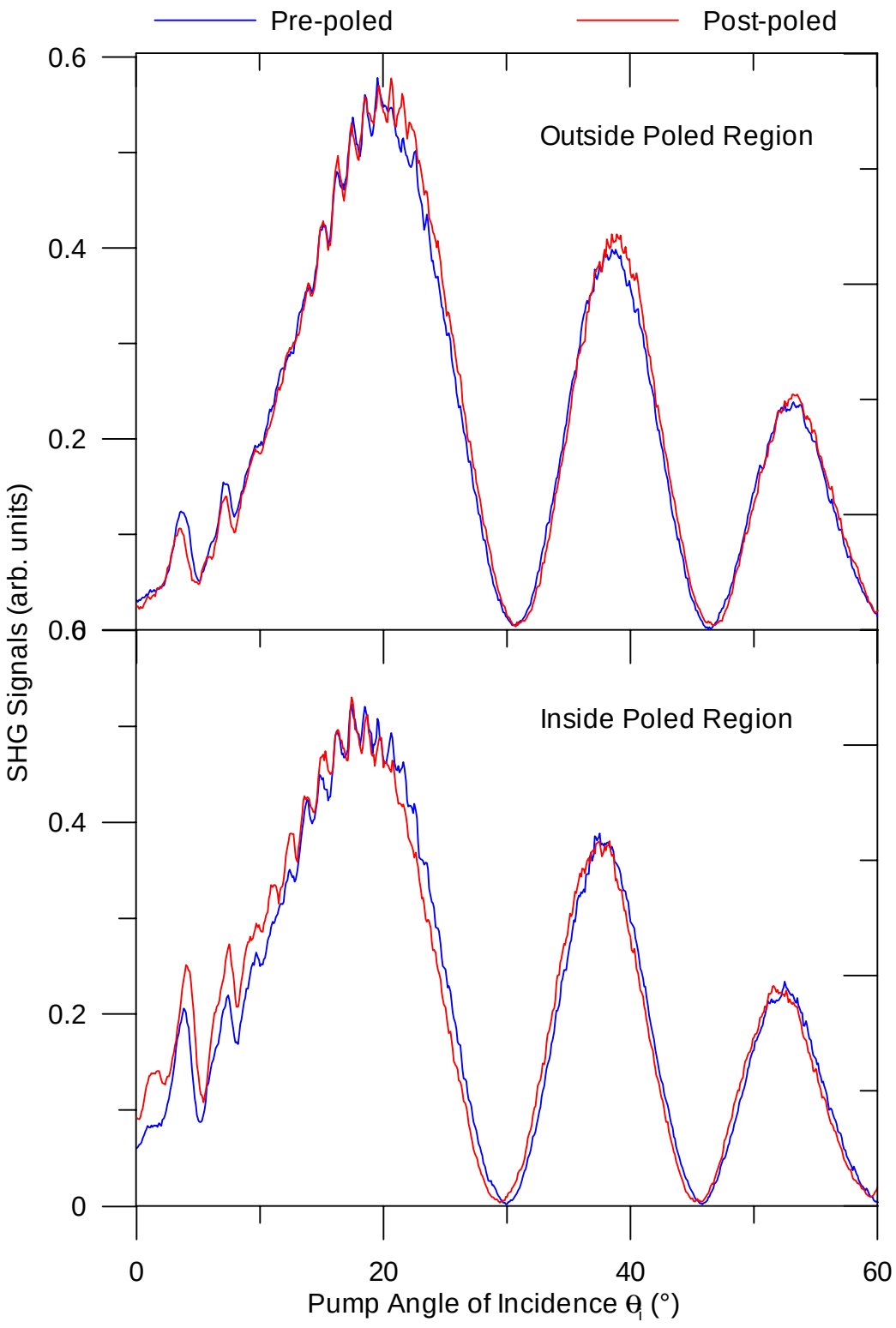

Figure 4.18 Comparison of *o-o* Maker-fringe signals inside and outside the domain reversed region.

applied electric field to the data. In so doing, the thicknesses and indices found from the baseline data set are used as inputs to the solver. The results of this fit are displayed in Figure 4.19 (a). The location of the poled region is clearly visible in the center of this contour map. In the poled region the average electric field has shifted to -5.1 kV/mm while the average electric field outside the poled region is 0.3 kV/mm. The slight increase in the electric field in the nonpoled region of the sample is most likely due to a new uncompensated depolarization field due to temperature changes during processing. However, the large decrease in the apparent electric field in the poled region must be due to some change in the material as a result of the poling process. It is not thought to be a surface charge effect because the sample has been rinsed in water as part of the photoresist removal process. This rinsing would have presumably neutralized such a high surface charge.

The sample was annealed in a box furnace in an attempt to eliminate the perturbation to the Maker-fringe signals caused by electric field poling. The anneal consisted of heating the sample at a rate of 2 ºC/min from room temperature to 200 ºC and held at this temperature for 12 min. The furnace was then turned off and the whole setup was allowed to cool back to room temperature. The third set of Maker fringe scans was then taken immediately after the sample reached room temperature. Analysis of this data set will be presented later. The sample was then discharged by placing it in a low vacuum as described earlier in Section 4.3. After being discharged, the fourth set of Maker-fringe scans was taken. This data set is analyzed by again

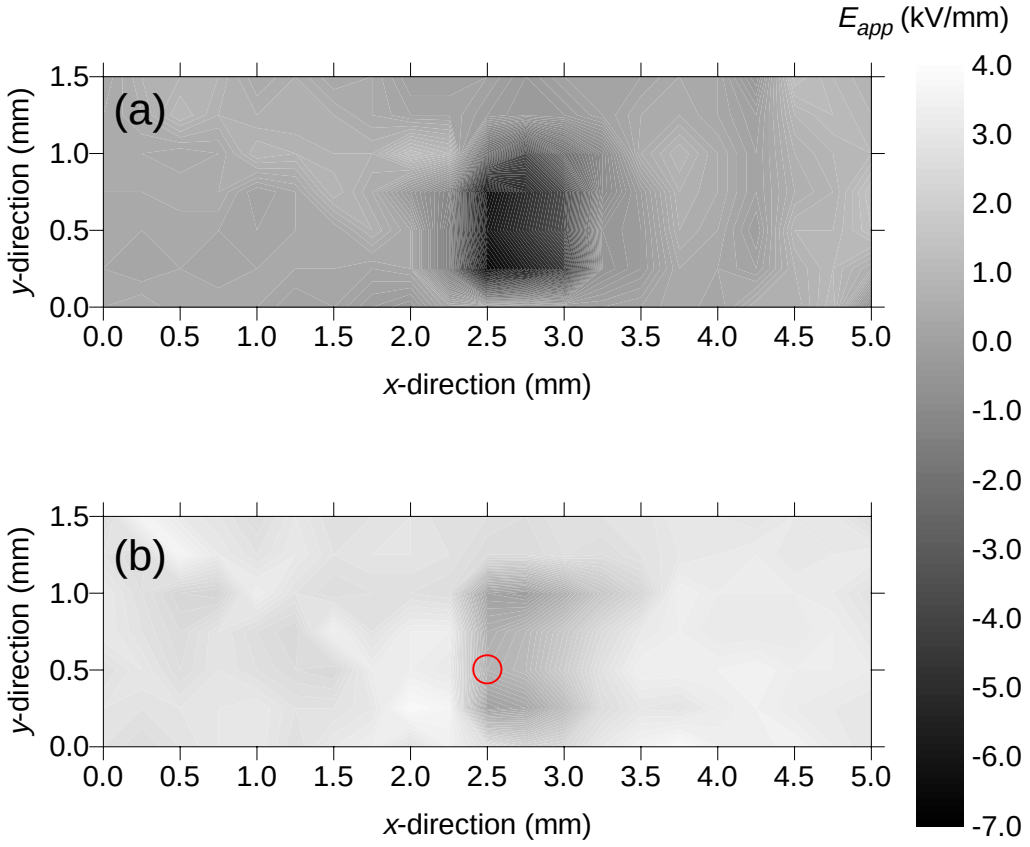

Figure 4.19 Contour maps of E_{app} for Sample Q taken (a) post poling and(b) post anneal and charge compensation. The red circle indicates the location of the Maker-fringe signals displaye in Figure 4.20.

solving for the apparent applied electric field using the thicknesses and indices found from the baseline data as input parameters to the solver. The result of this analysis is presented in the contour map of Figure 4.19 (b). The average electric field outside the domain-reversed region has increased to 3.0 kV/mm. The variation of the apparent applied electric field from data set to data set suggests that the sample is very susceptible to environmental conditions, such as temperature fluctuations, and that great care must be taken to fully neutralize the depolarization field. The average electric field in the domain reversed region was 1.0 kV/mm. Comparing $E_{in} - E_{out}$ immediately after poling (-5.4 kV/mm) and after annealing (-2.0 kV/mm) shows that the contrast of the domain reversed region has been reduced. I believed that more thorough annealing and charge compensation will completely eliminate this difference. Further discussion on the possible nature of the apparent field associated with the domain-reversal process as well as a correlation between this field and the poling dynamics will be presented in section 4.5.

An example of the effect of rotating the sample through a domain wall during a Maker-fringe scan is shown in Figure 4.20. These scans were taken at the location of the red circle in Figure 4.19 (b). The fringe anomaly centered at 47º can clearly be seen in the post-processed scan. The pre-processed scan, taken at the same location, is included for comparison. The fringe perturbation is due to an additional interference between the portion of the beam in one domain region and that in the other domain region.

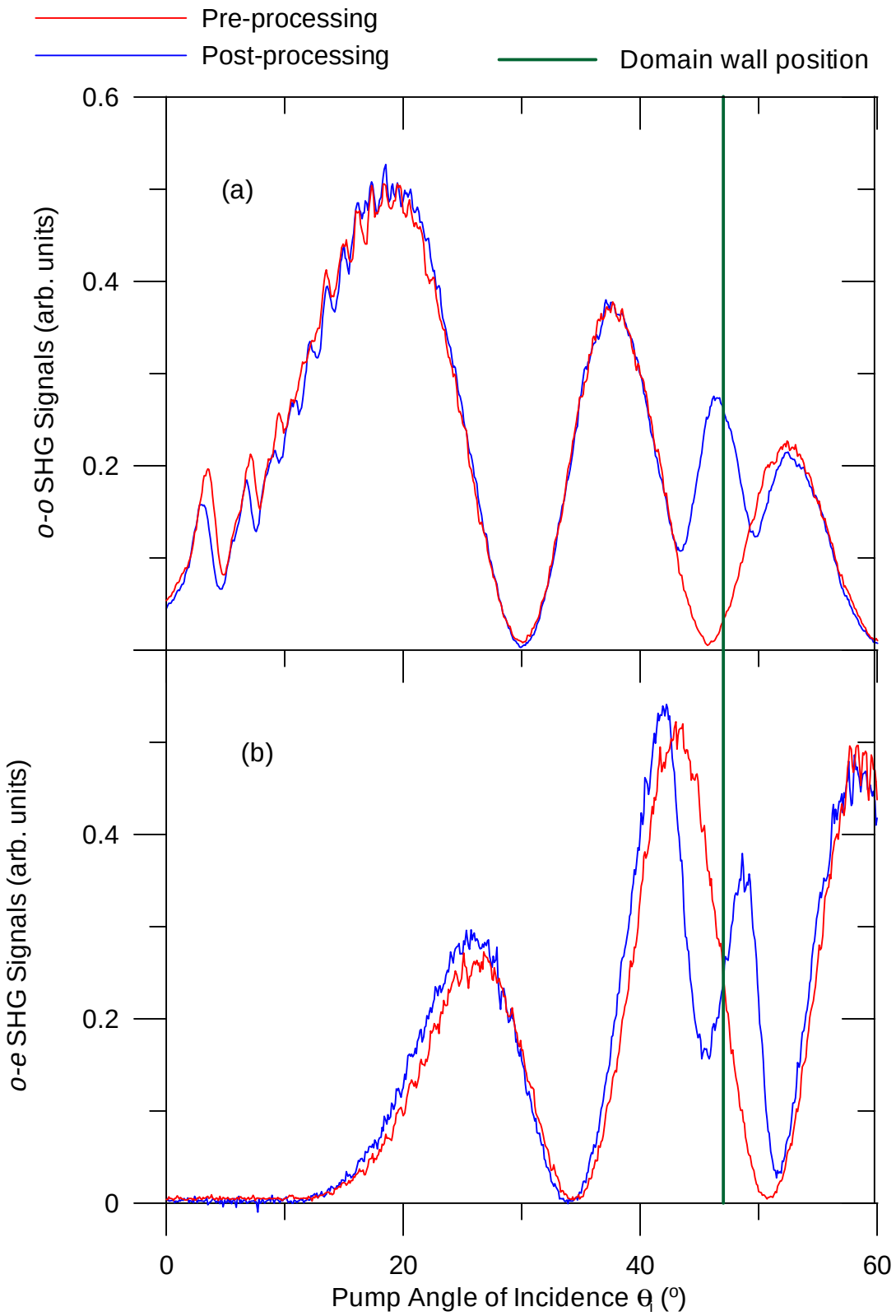

Figure 4.20 (a) *o-o* and (b) *o-e* Maker-fringe signals taken at the location designated by a red circle in Figure 4.19. A domain wall is encountered during the rotation.

The analysis of the data immediately following annealing but before discharging the sample shows a peculiar behavior in the resulting electric field. Again, this data set was solved for the apparent applied electric field while using the thicknesses and indices found from the baseline data set. Figure 4.21 shows the contour map of the resulting electric field. The average electric field for the originally domained material was -9.4 kV/mm, while that for the domain-reversed material was +8.8 kV/mm. These results suggest that there is a nearly equal electric field across the sample's entire surface regardless of the domain region. The reason for the sign change in the poled region is that the direction of the spontaneous polarization is in the opposite direction and therefore the sign for the electric field is reversed. The consequence of this is that the electrooptic index change in the poled region will be in the opposite direction to that in the original domain region. This situation is presented graphically in Figure 4.22 a).

This result is perplexing. Assuming that annealing has to a large extent relaxed the effect of the domain reversal, intuition suggests that the direction of the uncompensated depolarization field would be identical with respect to the direction of each region's spontaneous polarization. The directions of these fields will be opposite to one another from the laboratory reference frame but identical from the material's frame of reference. This scenario is depicted in Figure 4.22 (b). This in turn would give rise to like changes in the Δn's and therefore like changes in the Maker fringe signals. This hypothesis results in a contour map of apparent electric field that shows no contrast

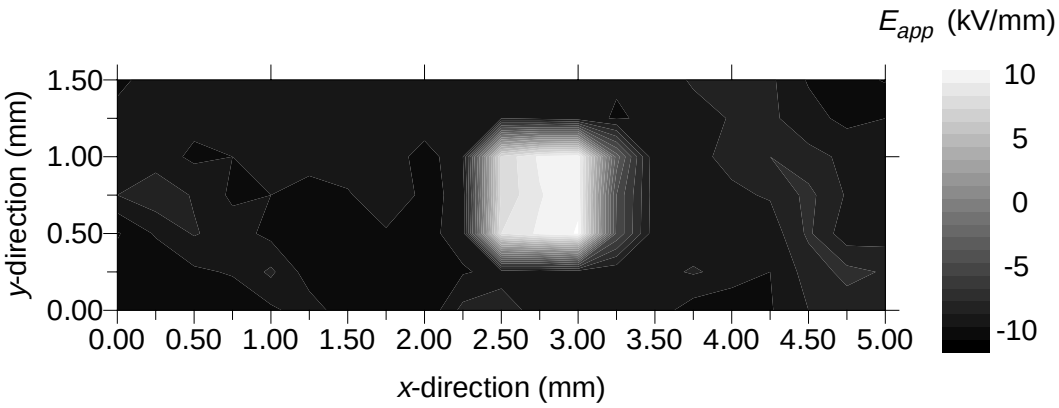

Figure 4.21 Contour map of E_{app} post domain reversal and anneal, no charge compensation has been done.

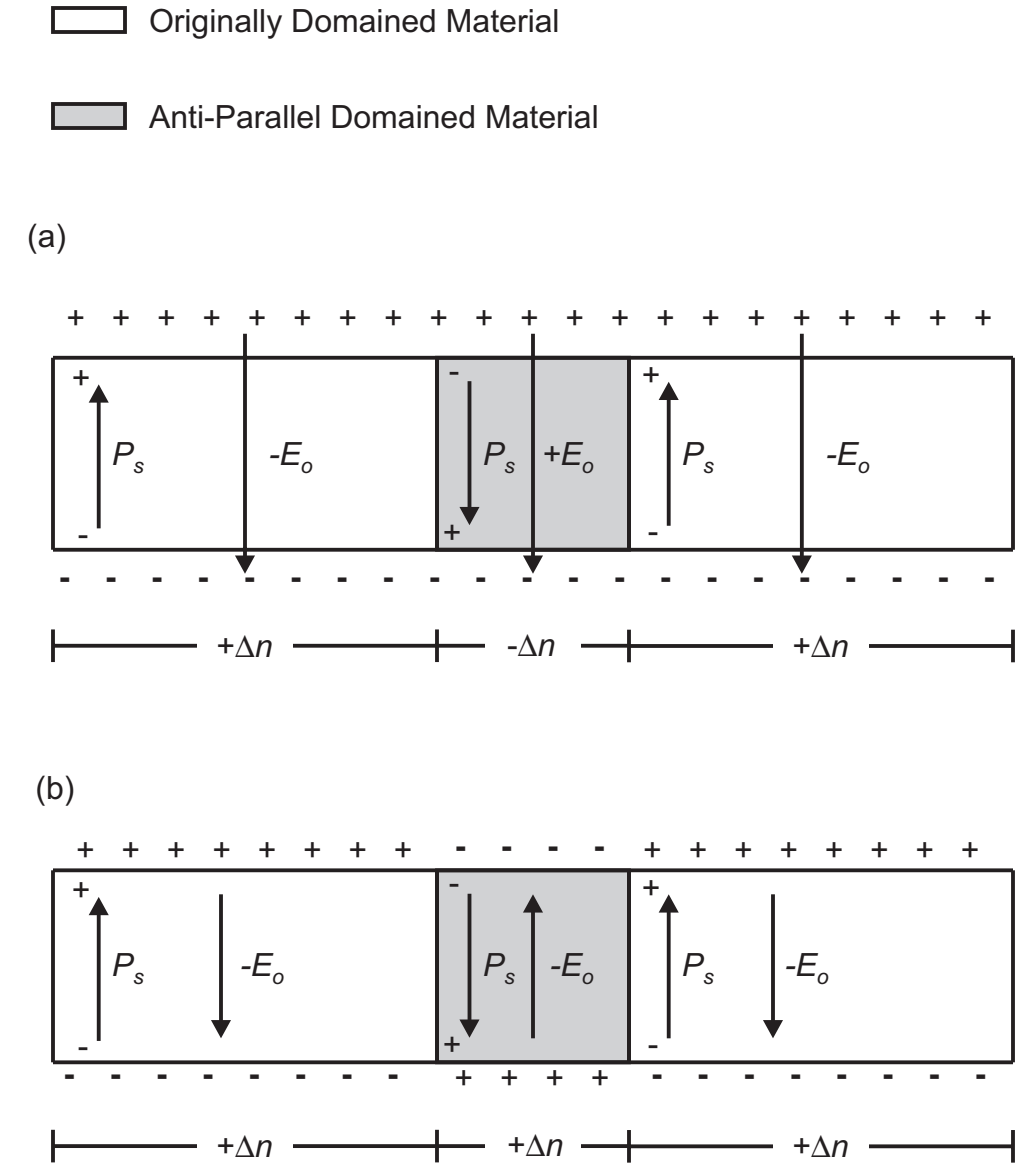

Figure 4.22 Schematic depicting the fields associated with the results seen in Figure 4.21. (a) what was observed and (b) what was predicted.

between the original and reversed domain regions. Once again the results show that such naive assumptions are apparently incorrect. It is plausible that a surface charge migration has occurred during annealing that has distributed the charge from the largest domain area, the original domain, over the entire surface.

4.5 Poling-Current Characteristics of Electric-Field-Induced Domain Reversal

Here I examine poling characteristics in an attempt to better understand the dynamics of the electric-field poling process in $LiNbO_3$. One common experiment used to examine ferroelectric materials is to measure the polarization of the material as a function of applied electric field. The result of such an experiment is the polarization hysteresis loop. During this type of experiment the direction of the material's spontaneous polarization is repeatedly reversed. However, because the high-voltage supply used here did not have the capability to ramp the voltage continuously, I was unable to perform such an experiment. Instead I developed an experiment to look at the poling characteristics given a single applied poling pulse. In particular, the poling-current characteristics were examined under these poling conditions. The same test area was repeatedly poled to the anti-parallel and parallel directions for several values of applied field. Anti-parallel poling is defined as poling the spontaneous polarization to a direction 180° from that of the

original material, while parallel poling is defined as poling the spontaneous polarization back to its original orientation.

The feature being poled during this experiment was a square with 0.76 mm long sides and was delineated by patterning photoresist on the + *z*-face of a 0.2 mm thick sub-wafer of $LiNbO_3$. The electric field strength and pulse duration were set to assure complete poling of the designated area in one applied pulse. Each pulse was 1 ms long and the applied electric field ranged from 18 to 29 kV/mm. The polarity of the pulse with respect to the sample was reversed to change the poling direction. The time between successive pulses was generally 2 to 3 min. Seven different samples, cut from a single wafer, were used during this experiment; each was taken through several domain reversal cycles for a range of applied electric fields. Four of the samples experienced electrical breakdown during the poling process. The number of domain reversals experienced by these samples before breakdown occurred ranged from 1 to 40. Interesting surface patterns were generated when electrical breakdown occurred. Figures 4.23 (a) and (b) show 5x and 50x optical microscope images of these surface patterns respectively. The patterns appear to be fractal in nature.

The current flowing through the poling circuit was recorded for each applied pulse. Figure 4.24 shows examples of the anti-parallel poling current for three different applied fields. Note that the “bumpiness” of the poling current traces is not electrical noise in the data acquisition system but is “domain reversal noise” due to domain nucleation and propagation. The

(a)

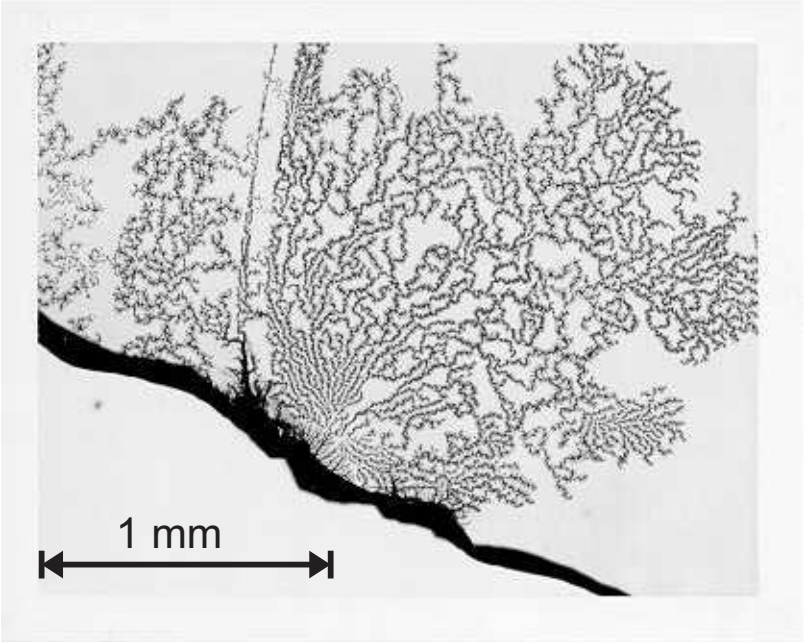

(b)

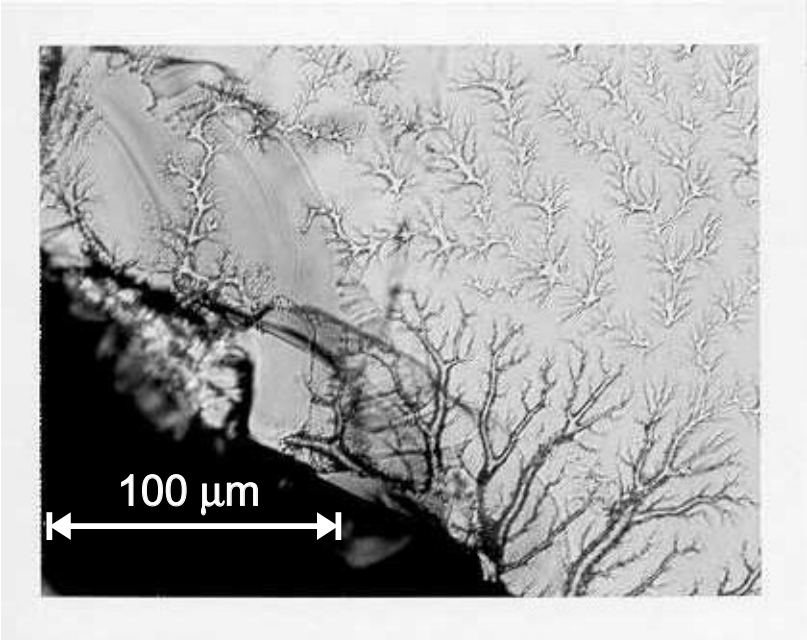

Figure 4.23 Photographs depicting the aftermath of electrical breakdown, (a) 5x objective and (b) 50x objective.

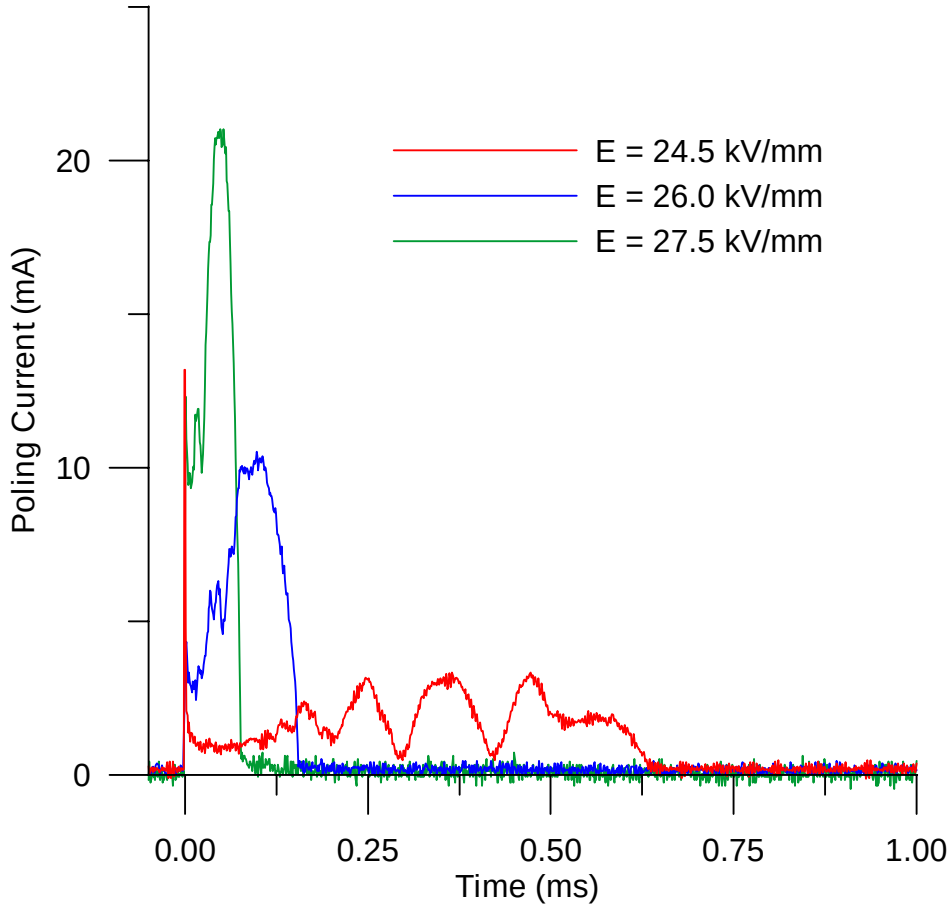

Figure 4.24 Examples of poling current for three different applied poling fields.

“domain-reversal noise” is analogous to the Barkhausen noise commonly observed with ferromagnetic phase transitions. This noise is most noticeable at low poling fields, where domain nucleation takes longer to form and suggests that there is non-uniformity within the crystal with regard to domain nucleation.

The area that has undergone domain reversal can be determined by integrating the current pulse

$$A = Q / 2P_s = \int i dt \Big/ 2P_s \,, \tag{140}$$

where P_s has a value of 0.71 μC/mm^2 [Camlibel ‘69]. Ideally the area of our poled region is 0.58 mm^2 and should remain constant for the repeated domain reversals. However, it was found that with increased cycling of the domain reversal, the area being poled grew outward and underneath the photoresist defining the opening. The area poled at the beginning of a series was typically 0.6 mm^2 and grew monotonically to a maximum of 0.85 mm^2 after 40 domain reversals.

The current data were analyzed by examining the maximum current obtained during a pulse divided by the area that underwent domain reversal I_{max}/A for each applied electric field. The data presented in Figure 4.25 represents the data taken for all 7 samples studied here. These data show a linear relationship between the applied field and the maximum current density for both the anti-parallel and parallel poling directions. The slopes of these two lines are very similar, 7.7 $\frac{\text{mA/mm}^2}{\text{kV/mm}}$ for the anti-parallel poling direction

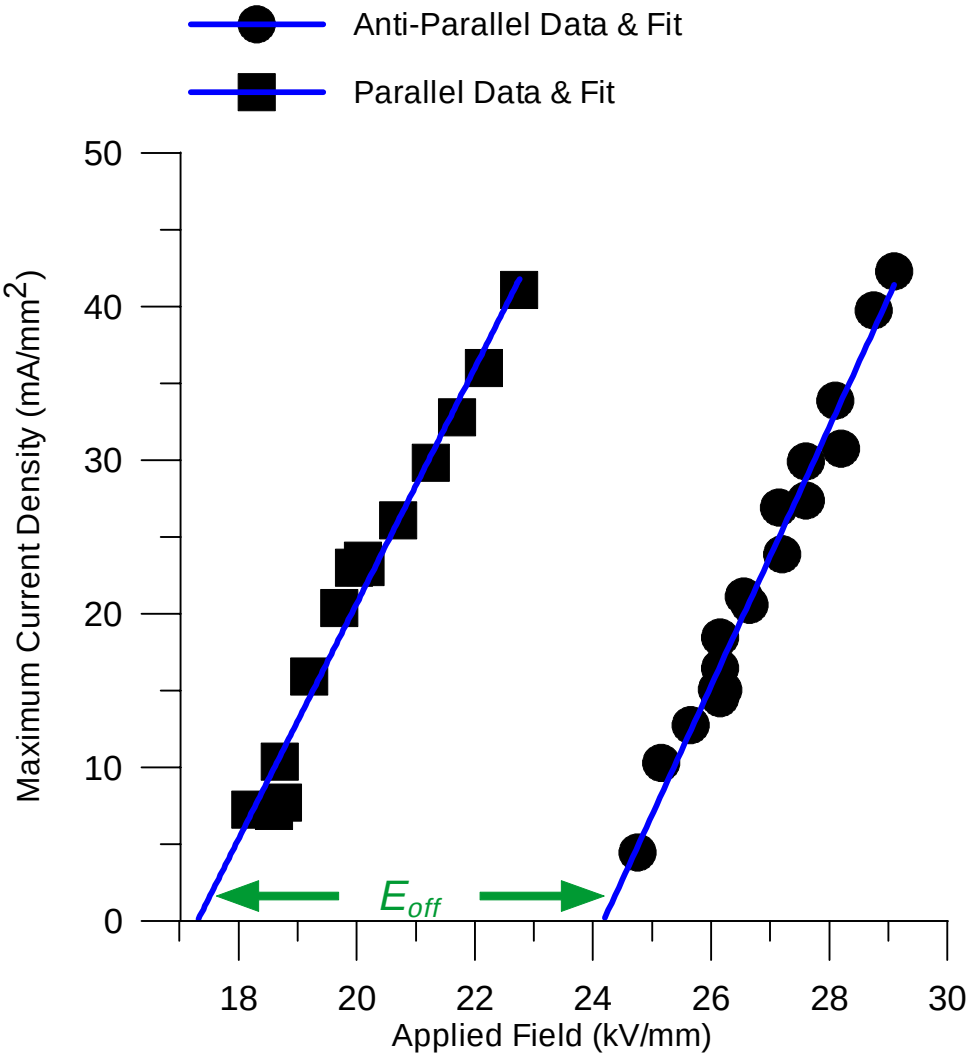

Figure 4.25 Maximum poling current observed for poling to the anti-parallel and parallel directions. Data is represented by black circles and squares. Linear fits to the data are shown with blue lines.

and 8.4 $\frac{\text{mA/mm}^2}{\text{kV/mm}}$ for the parallel poling direction. There is, however, an offset in the poling field between the anti-parallel and parallel poling directions. It takes less applied field to achieve the same maximum current density when poling to the parallel direction than it does in poling to the anti-parallel direction. This suggests a preferred direction for the spontaneous polarization that is parallel with the original domain direction. The coercive field E_c of a ferroelectric material is usually defined in terms of the polarization hysteresis loop. Here, I define the coercive field with respect to the maximum poling current density. The coercive field is defined as the applied field at the point the maximum current density goes to zero. Extrapolating the data in Figure 4.25 to zero current density shows an anti-parallel coercive field E_c^{A-P} of 24.2 kV/mm and a parallel coercive field E_c^{P} of 17.3 kV/mm. The difference between these coercive fields $E_{off} = E_c^{A-P} - E_c^{P}$ is 6.9 kV/mm.

Next, one of the surviving samples was poled to the anti-parallel direction and left there. The sample was then annealed in a box furnace at 200ºC for 12 min and allowed to cool back to room temperature as was done for the sample in section 4.4. The sample was then put back in the poling system and again repeatedly domain reversed. The poling current was again recorded for a range of applied electric fields for both the anti-parallel and parallel poling directions. The definition of anti-parallel and parallel is still referenced to the original domain direction. Figure 4.26 shows the post-

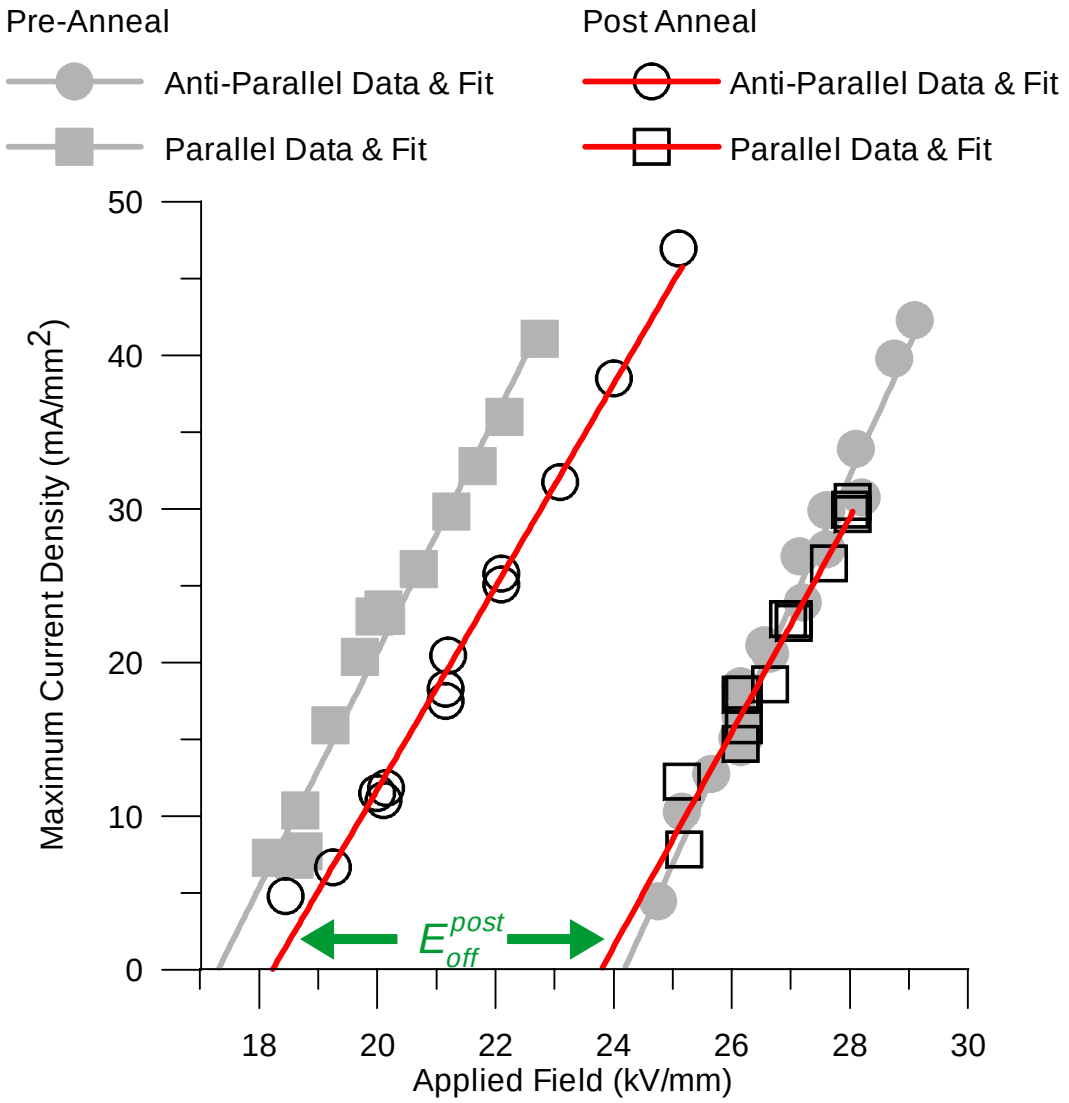

Figure 4.26 Similar representation as in Figure 4.25 but taken after the sample was annealed in the anti-parallel direction. Post-anneal data represented by open circles and squares. Linear fits to these data are given by red lines. The original pre-anneal data from Figure 4.25 is displayed here in gray for comparison.

annealed maximum current density as a function of applied field. The original pre-annealed data are shown in gray for comparison purposes.

The relationship between the current density and the applied field is once again linear for both of the poling directions. The slopes of these two lines are again very similar to one another, 6.6 $\frac{\text{mA/mm}^2}{\text{kV/mm}}$ for the anti-parallel case and 7.0 $\frac{\text{mA/mm}^2}{\text{kV/mm}}$ for the parallel case, but the slopes have decreased with respect to those for the pre-annealed data. The most striking difference seen here is the location of the post-annealed data with respect to the pre-annealed data. The post-annealed parallel data overlay the pre-annealed anti-parallel data. This implies that poling away from the annealed domain direction is similar to poling away from the original domain direction in the pre-annealed state. Annealing the domain-reversed material has essentially returned it to its original state but with its spontaneous polarization pointing in the opposite direction, this direction being the new preferred domain direction. However, the post-annealed anti-parallel data do not overlay the pre-annealed parallel data. This suggests that not everything about the material has been fully reversed after the domain reversal and subsequent anneal. The coercive field for the post-annealed anti-parallel data has increased when compared to the pre-annealed parallel data. As a result the offset between the coercive fields for the post-annealed data E_{off}^{post} has decreased to 5.6 kV/mm.

The difference in the coercive fields between poling in the anti-parallel and parallel directions is not unprecedented. Gopalan and Gupta [Gopalan '97] as well as Wang *et al* [Wang '97] have reported observing differences between the coercive fields for the two poling directions of 6.7 kV/mm and 7.0 kV/mm respectively. These values are for as-received samples and compare favorably to the value of 6.9 kV/mm reported here. Gopalan also reports a coercive field difference of ~4 kV/mm for an annealed domain-reversed sample [Gopalan '97]. Their annealing consisted of a rapid heating to 200ºC, a 2 min dwell, and a rapid cooling back to room temperature.

In a follow-up paper examining congruent and stoichiometric $LiNbO_3$, Gopalan *et al* [Gopalan '98] conclude that the origin of the difference in the coercive fields for the two poling directions is related to the non-stoichiometry of the material. He further explains the asymmetry in the polarization hysteresis loop as being the result of an intrinsic internal field. The internal field is defined as $E_{\text{int}} = \frac{1}{2}\left(E_c^{A-P} - E_c^{P}\right)$ and is oriented parallel to the original spontaneous polarization.

I will attempt to further explain the presence of this internal field. Lines and Glass [Lines '77] state that defects in a ferroelectric crystal structure generally increase the coercive field of a material and give rise to a defect polarization ΔP. The defect polarization can be modeled as an equivalent field of $E_{int} = \Delta P/\varepsilon\varepsilon_o$. They further state that when the spontaneous polarization of a crystal is reversed by the application of an electric field, the defect polarization may or may not be reversed with it.

In the case of congruent $LiNbO_3$, the deficiency of Li in the material results in a crystalline structure containing defects. There are two cation substitution models commonly proposed for the defect chemistry of congruent $LiNbO_3$. The Li-site vacancy model involves Li vacancies $(V_{Li})^-$ and Nb anti sites $(Nb_{Li})^{4+}$ and the Nb-site vacancy model involves Nb vacancies $(V_{Nb})^{5-}$ and Nb anti sites. Evidence for both these models has been reported in the literature [Watanabe '95, Schirmer '91] without definitively confirming the validity of one model over the other. One theoretical investigation suggesting the presence of the ilmenite structure Li Nb □ Nb Li □ Li Nb □ Nb Li within the $LiNbO_3$ structure has lead to the observation that these two models may in fact be synonymous [Donnerberg '91]. Regardless of which model is correct, there are charged point defects due to the deficiency of Li in congruent $LiNbO_3$. As stated by Lines and Glass, these charged defects will give rise to a defect polarization which in turn can be considered as a defect induced electric field. The defect-induced electric field is most probably the source of the internal field reported by [Gopalan '97].

The data reported here show further support for this hypothesis. A plausible explanation for my observations is that congruent $LiNbO_3$ has associated with it a defect polarization aligned in the direction of the original spontaneous polarization. This defect polarization impedes domain reversal to the anti-parallel direction and assists domain reversal to the parallel direction. Further, even though the defect polarization prefers to be aligned in the direction of the spontaneous polarization, it is not reversed by the

application of the poling field. The defect polarization does, however, almost completely re-align itself to the anti-parallel spontaneous polarization during a 200 ºC annealing. This suggests that the energy of the defect is relatively low, 4×10^{-2} eV. I believe that this is a result of the movement of the defect vacancies within the crystal. The vacancy locations appear not to move under the application of the poling field but do appear to move during annealing to re-establish their preferred relationship with the spontaneous polarization.

With these interpretations of the results, the Maker fringe data presented in Section 4.4 can now explained. The fringe shift resulting from the domain reversal is the effect of the defect polarization acting on indices of refraction of the material. The magnitude of the index changes is the result of the net difference in the electric field the material 'sees' acting through the electrooptic effect. The net difference in the electric field is

$$E_{off} = 2 \cdot E_{\text{int}} = E_c^{A-P} - E_c^{P} .$$

Chapter 5

Conclusion

The Maker-fringe theory developed here has proven to be quite accurate at reproducing the second-harmonic signals generated by *z*-cut $LiNbO_3$. Theoretical descriptions for all four pump-SHG polarization orientations capable of being produced by rotation about the *y*-axis of a *z*-cut wafer have been developed. Simultaneously fitting all four of these pump-SHG orientations to thickness, ordinary index of refraction at the pump and second-harmonic wavelengths, and extraordinary index of refraction at the pump and second-harmonic wavelengths has led to the most comprehensive Maker-fringe analysis attempted to date. The results of this analysis have corroborated previous researchers' claim of lower than expected extraordinary indices of refraction [Shoji '97, Sanford '98]. The results of this work suggest the difference between the extraordinary index of refraction and that predicted by the Sellmeier equation derived by Edwards & Lawrence [Edwards '84] is $-5.7 \times 10^{-4} \pm 1.4 \times 10^{-4}$ at the pump wavelength (1.064 μm) and $-9.7 \times 10^{-4} \pm 1.7 \times 10^{-4}$ at the second-harmonic wavelength (532 nm). Correlation of reported composition-related phase matching temperatures suggests the reason for the low values of n_e. Apparently, the composition of the material used for the original index studies was lithium deficient, 48.3 mol

% Li_2O, compared to current congruent material, 48.38 ± 0.015 mol % [Bordui '91].

However, it has been discovered that an independent measure of the sample's thickness must be made in order to eliminate the degenerate nature of the solutions obtained during the Maker-fringe analysis. With the thickness of the sample measured to within 5×10^{-5}, the indices of refraction can be determined to within a few parts in 10^{-5}. Researchers at NIST, Gaithersburg, now have a thickness measurement technique that uses gauge blocks, which may prove to be useful in determining wafer thickness to this precision. Great care must also be taken to fully compensate the sample for any depolarization fields that may be present due to its pyroelectric response to temperature fluctuations. This perturbation to the Maker-fringe signals is associated only with *z*-cut material; pyroelectricity will not effect *x*- and *y*-cut $LiNbO_3$.

I have also used Maker-fringe analysis to examine the DC electrooptic coefficients of $LiNbO_3$. The values obtained for r_{13}^T and r_{33}^T were larger than those generally seen in the literature [Weis '85, Mendez '99]. However, the electrooptic coefficients reported in the literature are for low frequency AC fields, not true DC fields as were studied here. This subtlety may explain the discrepancy.

Examining electric-field domain-reversed material proved to be very interesting. It was observed that the electric-field domain reversal process did affect the Maker-fringe signals. The magnitude of the perturbation to the

Maker-fringe signals was quantified by fitting the data to an apparent applied electric field in the *z*-direction. The result of this fit suggested an applied field of -5.4 kV/mm. The shift in the Maker-fringe signals could be partially relaxed by a short anneal at 200 °C. The apparent applied field in the domain reversed region after annealing was -2.0 kV/mm. I believe a full recovery of the sample will occur given a slightly more rigorous anneal.

Examining the poling current as a function of applied field, I was able to demonstrate electric field asymmetries (6.9 kV/mm) in my maximum current density experiment similar to what other researchers have reported in their polarization hysteresis loops (6.7 kV/mm [Gopalan ‘97] and 7.0 kV/mm [Wang ‘97]). Since the asymmetry is such that it is easier to pole the material back to the original domain direction, it must be oriented in the direction of the original spontaneous polarization. This would make the asymmetry field negative with respect to the domain-reversed material, just as was seen from the Maker-fringe analysis of the domain reversed material. I believe that the apparent applied field seen from the Maker-fringe analysis of the domain-reversed material and the asymmetric field seen during the poling experiments are the result of the same phenomenon.

The exact reason for this effect is not known. However, these results support the contention that it is the result of a defect-induced polarization associated with congruent $LiNbO_3$. The defect polarization seems to be unaffected by the poling fields but greatly affected by a 200 °C annealing. As

a result of this behavior, I believe the vacancy site location with respect to the rest of the ionic structure is the cause of this phenomenon.

Gopalan has shown that the asymmetry in the polarization hysteresis loop goes to zero as the composition of $LiNbO_3$ goes to stoichiometric [Gopalan ‘98]. This result lends credibility to the defect-induced polarization hypothesis because stoichiometric material has far fewer defects than congruent material. Gopalan also shows that the coercive field decreases by ~15 kV/mm for stoichiometric material. Presumably, electric-field poling of stoichiometric material would suffer far fewer instances of electrical breakdown; this could lead to much high yields and lower prices for QPM devices.

Consideration for future work should be given to performing Maker-fringe analysis at different pump wavelengths, in conjunction with an independent thickness measurement, in an effort to obtain more index data for congruent material. This could lead to more accurate Sellmeier equations for $LiNbO_3$. Poling studies as well as Maker-fringe analysis should be performed on stoichiometric material. Again, Maker-fringe analysis at several pump wavelengths could lead to extremely accurate Sellmeier equations for this material. The poling studies would provide needed data to evaluate stoichiometric material as a suitable substrate for QPM devices.

Bibliography

Aust, J.A., B. Steiner, N.A. Sanford, G. Fogarty, B. Yang, A. Roshko, J. Amin, and C. Evans, “Examination of domain-reversed layers in *z*-cut $LiNbO_3$ using Maker fringe analysis, atomic force microscopy, and high-resolution *x*-ray diffraction imaging,” in *Conference on Lasers and Electro-Optics*, Vol. 11 of 1997 OSA Technical Digest Series (Optical Society of America, Washington, D.C., 1997) pp. 485. (A)

Aust, J.A. N.A. Sanford, and J. Amin, “Maker fringe analysis of *z*-cut lithium niobate,” in *Proceedings of the 10th Annual Meeting of IEEE Lasers and Electro-Optics Society* (IEEE Lasers and Electro-Optics Society, Piscataway, N.J., 1997), pp. 114-115. (B)

Bergman, J.G., A. Ashkin, A.A. Ballman, J.M. Dziedzic, H.J. Levinstein, and R.G. Smith, “Curie temperature, birefringence, and phase-matching temperature varistions in $LiNbO_3$ as a function of melt stoichiometry,” Appl. Phys. Lett. **12**, 92 (1968).

Bloembergen, N. and P.S. Pershan, “Light waves at the boundary of nonlinear media,” Phys. Rev. **128**, 606 (1962).

Bordui, P.F., R.G. Norwood, C.D. Bird, and G.D. Calvert, “Compositional uniformity in growth and poling of large-diameter lithium niobate crystals,” J. Cryst. Growth **113**, 61 (1991) .

Bordui, P.F., R.G. Norwood, D.H. Jundt, and M.M. Fejer, “Preparation and characterization of off-congruent lithium niobate crystals,” J. Appl. Phys. **71**, 875 (1992).

Byer, R.L., J.F. Young, and R.S. Feigelson, “Growth of high-quality $LiNbO_3$ crystals from the congruent melt,” J. Appl. Phys. **41**, 2320 (1970).

Camlibel, I., “Spontaneous polarization measurements in several ferroelectric oxides using a pulsed-field method,” J. Appl. Phys. **40**, 1690 (1969).

Carruthers, J.R., G.E. Peterson, M. Grasso, and P.M. Bridenbaugh, “Nonstoichiometry and crystal growth of lithium niobate,” J. Appl. Phys. **42**, 1846 (1971).

Choa, S., W. Davis, D.D. Tuschel, R. Nichols, M. Gupta, and H. C. Cheng, “Time dependence of ferroelectric coercive field after domain inversion for lithium-tantalate crystal,” Appl. Phys. Lett. **67**, 1066 (1995).

Crystal Technology, Inc., “Lithium niobate optical crystals,” product data sheet DC-12, (Crystal Technology, Inc., 1040 East Meadow Circle, Palo Alto, CA 94303, 1993).

Donnerberg, H.J., S.M. Tomlinson, and C.R.A. Catlow, “Defects in $LiNbO_3$—II. Computer simulation,” J. Phys. Chem. Solids **52**, 201 (1991).

Dmitiev, V.G., G.G. Gurzadyan, and D.N. Nikogosyan, *Handbook of nonlinear optical crystals* (Springer-Verlag, Berlin, 1991).

Edwards, G.J. and M. Lawrence, “A temperature-dependent dispersion equation for congruently grown lithium niobate,” Opt. Quant. Electr. **16**, 373 (1984).

Goldberg, L., R.W. McElhanon, and W.K. Burns, “Blue light generation in bulk periodically field poled $LiNbO_3$,” Eletron. Lett. **31**, 1576 (1995).

Gopalan, V. and M. Gupta, “Origin and characteristics of internal fields in LiNbO3 crystals,” Ferroelectrics **198**, 49 (1997).

Gopalan, V., T.E. Mitchell, Y. Furukawa, and K. Kitamura, “The role of nonstoichiometry in 180° domain switching of $LiNbO_3$ crystals,” Appl. Phys. Lett. **72**, 1981 (1998).

Hecht, E., *Optics, second edition* (Addison-Wesley Publishing Company, Reading, MA, 1987.

Jerphagnon, J. and S.K. Kurtz, “Maker fringes: A detailed comparison of theory and experiment for isotropic and uniaxial crystals,” J. Appl. Phys. **41**, 1667 (1970).

Kleinman, D.A., “Nonlinear dielectric polarization in optical media,” Phys. Rev. **126**, 1977, 1962.

Kurtz, S.K., J. Jerphagnon, and M.M. Choy, Landolt-Bornstein Numerical data and functional relationships in science and technology, Vol. 11 (Springer-Verlag, Berlin, 1979).

Lines, M.E. and A.M. Glass, *Principles and Applications of Ferroelectrics and Related Materials* (Clarendon Press, Oxford, 1977).

Lunt, S.R., G.E. Peterson, R.J. Holmes, and Y.S. Kim, “Maker fringe analysis of lithium niobate integrated optical substrates,” Integrated Optical Circuit Engineering II, S. Sriram ed., Proc. SPIE **578**, 22 (1985).

Maker, P.D., R.W. Terhune, M. Nisenoff, and C.M. Savage, “Effects of dispersion and focusing on the production of optical harmonics,” Phys. Rev. Lett. **8**, 21 (1962).

Mendez, A., A. Garcia-Cabanes, E. Dieguez, and J.M. Cabrera, “Wavelength dependence of electro-optic coefficients in congruent and quasi-stoichiometric $LiNbO_3$,” Electr. Lett. **35**, 498 (1999).

Meyn, J.P. and M.M. Fejer, “Tunable ultraviolet radiation by second-harmonic generation in periodically poled lithium niobate,” Opt. Lett. **22**, 1214 (1997).

Miller, G.D., “Periodically poled lithium niobate: Modeling, fabrication, and nonlinear-optical performance,” Ph.D. Dissertation, Department of Electrical Engineering, Stanford University, 1998.

Mitchell, J.A., “Fabrication and characterization of quasi-phase-matched nonlinear optical devices,” M.S. Thesis, Department of Physics, University of Colorado, 1999.

Möller, K.D., *Optics* (University Science Books, Mill Valley, CA, 1988).

Myers, L.E., “Quasi-phasematched optical parametric oscillators in bulk periodiclly poled lithium niobate,” Ph.D. Dissertation, Department of Electrical Engineering, Stanford University, 1995.

Nelson, D.F. and R.M. Mikulyak, “Refractive indices of congruently melting lithium niobate,” J. Appl. Phys. **45**, 3688 (1974).

Pruneri, V., R. Koch, P.G. Kazansky, W.A. Clarkson, P.St.J. Russell, and D.C. Hanna, “49 mW of cw blue light generated by first-order quasi-phase-matched frequency doubling of a diode-pumped 946-nm Nd:YAG laser,” Opt. Lett. **20**, 2375 (1995).

Rosenman, G., Kh. Garb, A. Skliar, M. Oron, D. Eger, and M. Katz, “Domain broadening in quasi-phase-matched nonlinear optical devices,” Appl. Phys. Lett. **73**, 865 (1998).

Sanford, N.A., and J.A. Aust, “Nonlinear optical characterization of LiNbO3. I. Theoretical analysis of Maker fringe patterns for *x*-cut wafers,” J. Opt. Soc. Am. B **15**, 2885 (1998).

Sanford, N.A. and J.A. Aust, “Nonlinear optical characterization of LiNbO3. II. Wafers sequentially cut from a single boule,” To Be Submitted to J. Opt. Soc. Am. B.

Schirmer, O.F., O. Thieman, and M. Wöhlecke, “Defects in $LiNbO_3$—I. Experimental aspects,” J. Phys. Chem. Solids **52**, 185 (1991).

Serway, R.A., *Physics* (Saunders College Publishing, New York, NY 1983).

Shen, Y.R., *The Principles of Nonlinear Optics* (John Wiley & Sons, New York, 1984)

Shoji, I., T. Kondo, A. Kitamoto, M. Shirane, and R. Ito, “absolute scale of second-order nonlinear-optical coefficients,” J. Opt. Soc. Am. B **14**, 2268 (1997).

Wang, H.F., Y.Y. Zhu, S.N. Zhu, and N.B. Ming, “Investigation of ferroelectric coercive field in $LiNbO_3$,” Appl. Phys. A **65**, 437 (1997).

Watanabe, Y., T. Sota, K. Suzuki, N. Iyi, K. Kitamura, and S. Kimura, “Defect structures on $LiNbO_3$,” J. Phys. Condens. Matter, **7**, 3627 (1995).

Webjörn, J., V. Pruneri, P.St.J. Russell, J.R.M. Barr, and D.C. Hanna, “Quasi-phase-matched blue light generation in bulk lithium niobate, electrically poled via periodic liquid electrodes,” Eletron. Lett. **30**, 894 (1994).

Weis, R.S. and T.K. Gaylord, “Lithium niobate: Summary of physical properties and crystal structure,” Appl. Phys. A **37**, 191 (1985).

Yamada, M., N. Nada, M. Saitoh, and K. Watanabe, “First-order quasi-phase matched LiNbO3 waveguide periodically poled by applying an external field for efficient blue second-harmonic generation,” Appl. Phys. Lett. **62**, 435 (1993).

Yariv, A. and P. Yeh, *Optical Waves in Crystals* (John Wiley & Sons, New York, 1984)

Appendix A

Definition of Symbols

L	sample thickness
d_p, d_s	1/e diameter of the pump and SHG beams; $d_s = d_p/\sqrt{2}$
λ_p, ω_p	pump wavelength and frequency
λ_s, ω_s	second-harmonic wavelength and frequency; $\lambda_s = \lambda_p/2$
ε_{11}, ε_{22}, ε_{33}	dielectric coefficients
$d_{ijk}^{(2)}$	nonlinear coefficients for $LiNbO_3$
$r_{13,p}^T, r_{13,s}^T$	unclamped electrooptic coefficient relating ordinary index changes due to *z*-directed electric fields for the pump and SHG wavelengths
$r_{33,p}^T, r_{33,s}^T$	unclamped electrooptic coefficient relating extraordinary index changes due to *z*-directed electric fields for the pump and SHG wavelengths
$n_{o,p}$, $n_{e,p}$	ordinary and extraordinary indices of refraction at the pump wavelength
$n_{o,s}$, $n_{e,s}$	ordinary and extraordinary indices of refraction at the second-harmonic wavelength
$n_{e,p}(\theta_{ep})$, $n_{e,s}(\theta_{es})$	angular dependent extraordinary index of refraction at the pump and SHG wavelengths
Δn_{ij}	index offset from the Sellmeier predicted value; subscript *i* corresponds to either *e*- or *o*-polarization while subscript *j* corresponds to either pump or SHG wavelength $\Delta n_{ij} = n_{ij}(calculated) - n_{ij}(Sellmeier)$
H_x, H_y, H_z	magnetic field components
E_x, E_y, E_z	electric field components
P_x, P_y, P_z	nonlinear source polarizations
k	genaric wave vector at wavelength λ
k_p	wave vector at the pump wavelength
k_s	wave vector at the second-harmonic wavelength
θ_i	angle of incidence of the pump wave, referenced to the surface normal of the sample

θ_{ep}, θ_{es}, θ_{op}, θ_{os}	angle of propagation in the $LiNbO_3$ referenced to the surface normal; *e* or *o* correspond to *e*- or *o*-polarization while *p* or *s* corresponds to pump or SHG
K_i	modified wave vector representing the projection of a wave vector onto a crystallographic axis; subscript *i*, see below for specific definitions
K_{xp}, K_{zp}	$k_p\sin\theta_i$ and $k_p\cos\theta_i$
K_{pr1x}, K_{pr1z}	$k_p\sin\theta_{r1}$ and $k_p\cos\theta_{r1}$
K_{pex}, K_{pez}, K_{poz}	$k_p n_{e,p}(\theta_{ep})\sin\theta_{ep}$, $k_p n_{e,p}(\theta_{ep})\cos\theta_{ep}$, and $k_p n_{o,p}\cos\theta_{op}$
K_{xs}, K_{zs}	$k_s\sin\theta_i$, $k_s\cos\theta_i$
K_{xes}, K_{zes}	$k_s n_{e,s}(\theta_{es})\sin\theta_{es}$, $k_s n_{e,s}(\theta_{es})\cos\theta_{es}$
K_{xep}, K_{zep}	$k_s n_{e,p}(\theta_{ep})\sin\theta_{ep}$, $k_s n_{e,p}(\theta_{ep})\cos\theta_{ep}$
K_{xop}, K_{zop}, K_{zos}	$k_s n_{o,p}(\theta_{op})\sin\theta_{op}$, $k_s n_{o,p}(\theta_{op})\cos\theta_{op}$, $k_s n_{o,s}(\theta_{os})\cos\theta_{os}$
$E^o_{p,x}, E^o_{p,y}, E^o_{p,z}$	pump wave electric-field amplitude components incident on the $LiNbO_3$
$E^o_{p,r1,x}, E^o_{p,r1,y}, E^o_{p,r1,z}$	pump wave electric-field amplitude components reflected from the front surface of the $LiNbO_3$
$E^o_{p,t1,x}, E^o_{p,t1,y}, E^o_{p,t1,z}$	pump wave electric-field amplitude components transmitted through the front surface of the $LiNbO_3$
$t1_e$, $r1_e$	single pass, first surface transmission and reflection coefficients for an *e*-polarized pump
$E^o_{p,r2,x}, E^o_{p,r2,y}, E^o_{p,r2,z}$	pump wave electric-field amplitude components reflected from the rear surface of the $LiNbO_3$
$E^o_{p,t2,x}, E^o_{p,t2,y}, E^o_{p,t2,z}$	pump wave electric-field amplitude components transmitted through the rear surface of the $LiNbO_3$
$t2_e$, $r2_e$	single pass, rear surface transmission and reflection coefficients for an *e*-polarized pump
$t1_o$, $r1_o$, $t2_o$, $r2_o$	*o*-polarized pump transmission and reflection coefficients for the front and rear surfaces of the $LiNbO_3$
$E^h_{e,t1,x}, E^h_{e,t1,y}, E^h_{e,t1,z}$	homogeneous solutions to the wave equations for SHG produced from an *e*-polarized pump wave
$E^p_{e,t1,x}, E^p_{e,t1,y}, E^p_{e,t1,z}$	particular solutions to the wave equations for SHG produced from an *e*-polarized pump wave
$E_{e,t1,x}, E_{e,t1,y}, E_{e,t1,z}$	general solutions to the wave equations for SHG produced from an *e*-polarized pump wave; equal to the sum of the homogeneous and particular solutions
$A_{e,t1,x}, A_{e,t1,y}, A_{e,t1,z}$	field amplitudes for the particular solutions to the wave equations for an *e*-polarized pump wave
$E^o_{e,t1,x}, E^o_{e,t1,y}, E^o_{e,t1,z}$	field amplitudes for the homogeneous solutions to the wave equations for an *e*-polarized pump wave

$E^{h}_{o,t1,x}, E^{h}_{o,t1,y}, E^{h}_{o,t1,z}$	homogeneous solutions to the wave equations for SHG produced from an *o*-polarized pump wave
$E^{p}_{o,t1,x}, E^{p}_{o,t1,y}, E^{p}_{o,t1,z}$	particular solutions to the wave equations for SHG produced from an *o*-polarized pump wave
$E_{o,t1,x}, E_{o,t1,y}, E_{o,t1,z}$	general solutions to the wave equations for SHG produced from an *o*-polarized pump wave; equal to the sum of the homogeneous and particular solutions
$A_{o,t1,x}, A_{o,t1,y}, A_{o,t1,z}$	field amplitudes for the particular solutions to the wave equations for an *o*-polarized pump wave
$E^{o}_{o,t1,x}, E^{o}_{o,t1,y}, E^{o}_{o,t1,z}$	field amplitudes for the homogeneous solutions to the wave equations for an *o*-polarized pump wave
$\eta_{p,e}$, $\eta_{p,e}$, $\eta_{p,e}$, $\eta_{p,e}$	heuristic correction factors for finite sized beams; *e* or *o* correspond to *e*- or *o*-polarization while *p* or *s* corresponds to pump or SHG
$t1_{e,FR}$, $r1_{e,FR}$	full resonance, first surface transmission and reflection coefficients for an *e*-polarized pump
$t2_{e,FR}$, $r2_{e,FR}$	full resonance, rear surface transmission and reflection coefficients for an *e*-polarized pump
$A^{FR}_{e,t1,x}, A^{FR}_{e,t1,y}, A^{FR}_{e,t1,z}$	full resonance field amplitudes for the particular solutions to the wave equations for an *e*-polarized pump wave
$t1_{o,FR}$, $r2_{o,FR}$	full resonance, first surface transmission and second surface reflection coefficients for an *o*-polarized pump
$A^{FR}_{o,t1,x}, A^{FR}_{o,t1,y}, A^{FR}_{o,t1,z}$	full resonance field amplitudes for the particular solutions to the wave equations for an *o*-polarized pump wave